A phenomenological approach to the prediction of material behaviours during co-sintering

Dissertation zur Erlangung

des naturwissenschaflichen Doktorgrades

der Julius-Maximilians-Universität Würzburg

vorgelegt von

Marc Delporte

Würzburg 2009

Eingereicht am: . . . .

bei der Fakultät für Chemie und Pharmazie

1. Gutachter: . . . .

2. Gutachter: . . . .

der Dissertation

1. Prüfer: . . . .

2. Prüfer: . . . .

3. Prüfer: . . . .

das öffentlichen Promotionskolloquiums

Tag des öffentlichen Promotionskolloquiums: . . . .

Doktorurkunde ausgehändigt am: . . . .

Contents

Contents i

Foreword and acknowledgment v

Summary / Zusammenfassung vii

1. Introduction 1

2. Material model description 7

- 2.1. Sintering kinetics with the Master Sintering Diagram (MSD) 7
  - 2.1.1. Assumptions 7
  - 2.1.2. How to construct and interpret the MSD? 9
- 2.2. Characterization of creep during sintering 12
  - 2.2.1. Viscous moduli 12
  - 2.2.2. Principle of the cyclic unloading method 13

3. Experimental techniques 15

- 3.1. Materials 15
  - 3.1.1. Partially stabilized zirconia 15
  - 3.1.2. Bi-layer alumina/zirconia 16
  - 3.1.3. Bi-layer glass-ceramic/alumina 17
- 3.2. Optical dilatometry 17
  - 3.2.1. Instrument 17
  - 3.2.2. Image analysis: principle, precision, repeatability and deviation 18
  - 3.2.3. Data treatment 20
  - 3.2.4. Specific setups 20
    - 3.2.4.1. Free sintering of tapes 20
    - 3.2.4.2. Loading setup 21
    - 3.2.4.3. Bending setup 22
  - 3.2.5. Experimental procedures and data treatment 23
    - 3.2.5.1. Free sintering of tapes 23
    - 3.2.5.2. Cyclic unloading dilatometry 23
    - 3.2.5.3. Warpage of asymmetric composites 25

3.2.5.4. Bending 27
3.3. Additional characterization methods 28
3.3.1. X-ray diffraction 28
3.3.2. Microstructure investigation 29
3.3.3. Density 30

4. Material model construction for one specific material: zirconia pressed compacts 31
4.1. Sintering characterization and input data 31
4.1.1. Free sintering kinetics 31
4.1.2. Sintering kinetics with load 33
4.2. Construction of the MSD with the input data 38
4.3. Viscous behaviour during sintering 43
4.3.1. Experimental determination of the viscous moduli 43
4.3.2. Influence of the load on the viscous moduli 44
4.3.3. Influence of the heating rate on the viscous moduli 44
4.3.4. Influence of the holding time on the viscous moduli 46
4.4. Microstructure investigations 48
4.4.1. Measurement of the particle size in the green-body 48
4.4.2. Influence of the thermal treatment on the microstructure of free sintered samples 48
4.4.3. Microstructure evolution during loaded sintering 49

5. Model validation 53
5.1. Validation procedures 53
5.1.1. Procedure for the validation of the sintering kinetics with the MSD . . . 53
5.1.2. Procedure for the validation of the viscous moduli 53
5.2. Prediction of the sintering kinetics with the MSD 54
5.3. Prediction of the warpage of a bi-layer with the experimentally determined viscous moduli 58
5.3.1. Free sintering mismatch between alumina and zirconia stacks 58
5.3.2. Characterization of the viscous moduli of alumina and zirconia stacks . . 58
5.3.3. Prediction of the curvature rate of a bi-layer 64

6. Co-sintering of a glass-ceramic and alumina bi-layer 67
6.1. Foreword 67
6.2. Sintering kinetics and crystallization of the glass-ceramic tape 67
6.3. Viscosity measurement of the glass-ceramic tape 72
6.4. Co-sintering of a bi-layer glass-ceramic/alumina 73
6.4.1. Sintering mismatch 73

6.4.2. Qualitative description of co-sintering 73
6.5. Conclusions on the co-sintering case of a glass-ceramic and alumina bi-layer . . 77

7. Discussion 79
7.1. Free sintering kinetics and apparent activation energy 79
7.2. Constrained sintering in zirconia 82
7.3. Experimental determination of the viscous moduli 84
7.3.1. Uniaxial viscosity 84
7.3.2. Viscous Poisson ratio 87

8. Conclusions and outlook 89
8.1. Conclusions on the material model 89
8.2. Parameters affecting co-sintering 91
8.3. Outlook 92

A. True strain 95
A.1. Strains and strain rates 95
A.2. Linear true and engineering strains 95
A.3. Volumetric strains and densities 96

B. Phase diagram ZrO_2 - Y_2O_3 101

Bibliography 103

List of Figures 109

List of Tables 113

List of symbols and abbreviations 115

Foreword and acknowledgment

This work was being performed between April 2006 and April 2009 in part time at the Fraunhofer Institute for Silicate Research in Würzburg and at the department for Advanced Research Materials at Robert Bosch GmbH in Stuttgart. The work was presented in October 2009 at the University of Würzburg in the Department for Chemistry and Pharmaceutical.

My first thanks go to Prof. Dr. Sextl who accepted to direct my work in his Chair and for his justified comments in the final corrections.

I would like to thank Dr. Lindner, head of the department for Advanced Research Materials at Robert Bosch GmbH and Mr Lindemann, Dr. Selten, Dr. Hiller, group leaders for the financial support of this work.

In 2008, I had the opportunity to take part at the international conference Sintering 2008. The scientific community debated the ”major challenges and opportunities in the field of sintering”. One of these was the *co-sintering and constrained sintering*. For having initiated this project combining industrial interests and up-to-date scientific challenges, I would like to thank Dr. Eisele (Robert Bosch) and Dr. Raether (Fraunhofer). Furthermore I am very grateful to Dr. Raether for his scientific support and guidance in this work. I appreciated his availability at all times, his experienced look and valuable hints in the difficult matter of sintering. I would like also to thank Dr. Eisele for his critical look on the scientific approach though keeping in focus the industrial interests.

Kind aknowledgements are addressed to Philipp Spies and André Moc for accepting to review the first version of this work.

Many thanks go precisely to Hans Schömig (Fraunhofer) who offered his assistance in the lab and his thoroughness. Thank you Hans, without your help my work would have been much more arduous! I also would like to thank André Moc (Robert Bosch) for the great collaboration. I appreciated our scientific discussions leading frequently to essential hints in this work. Thanks also for your patience and kindness in looking through my scripts in German. Finally, I’d like to thank Pay Schulze-Horn for his technical support and our fruitful cooperation during the first two years of my work.

I would like to address kind words to people helping me at some points in the scientific progress at Robert Bosch and at the Fraunhofer: (at Robert Bosch) Ingrid Wührl, Imgard Mann, Thomas Köhler and Christiane Müller, Uwe Glanz, Imke Herren, Niko Dorsch, Gaetan Deromelaere, Raphaëlle Satet, Jochen Rager, Daniel Meyer, Ingo Kerkamm, (at the Fraunhofer) Andreas Klimera, Maria Iuga and Jens Baber - thanks for all nice evenings in Würzburg - and the whole KF7 team of Dr. Torsten Staab. Special thanks go to Kathrin Nagy for her patience at teaching me some german words during the first months in Germany but also to Ingrid Wührl, Martin Schubert, Ralf Holzschuh and Thorsten Bober who constantly challenged me in using words out of the classical german dictionary! Welcome to Schwabenland!

I would like also to greet my Ph.D. colleagues at Robert Bosch and at the Fraunhofer and to wish them lot of fun and courage. I do not forget my friends in Switzerland that I quitted in 2006 to join as well the “Ph.D. family” and my friends who participated in keeping me motivated three years long.

A few words go to my parents for their endless encouragements and support in my choices during my education.

Finally, I address all my loving thanks to my girlfriend Chrystèle Déal for her endless support with love and patience during the last months of writing this work.

Summary

This work deals with the sintering of multi-material composites. It aims at the establishment of an alternative to the existing complex models for sintering. The development of the associated experimental procedure is also included in this work. The developed material model must be able to predict (i) the sintering kinetics and (ii) the viscous moduli of a material. An experimental approach with free sintering and hot-forging measurements is favoured in this work.

The prediction of the sintering kinetics is addressed with the construction of a map of sintering kinetics data: the Master Sintering Diagram (MSD). The MSD is based on a generalized equation for solid-state diffusion, thus is suitable for any thermal activated diffusion. The MSD allows the prediction of sintering kinetics for a large range of temperatures and external loads.

A novel approach to the determination of the viscous moduli is developed in this work: the cyclic unloading method. It is a hot-forging measurement (sintering under uniaxial compression) where the applied load is released for short periods. The measurements are carried out with continuous heating, so that the viscous moduli are determined over large ranges of temperatures and densities. The advantage of this method is the measurement of the viscous moduli in anisotropic microstructures.

The material model is validated in two steps. Firstly, the predictions of sintering kinetics with the MSD are compared with experimental results: changes of thermal profile and changes of load are predicted with a maximum deviation of 10%. Secondly, the experimentally determined viscous moduli are used for the prediction of a bi-layer curvature using models for warpage from literature. The prediction is qualitatively good for a maximum deviation of 27%.

The study of a sintering glass-ceramic tape on a rigid substrate is presented. It shows that this co-sintering problem can be qualitatively investigated with requirement of the material model.

The formation of anisotropy intrinsic to the hot-forging experiments is also reported in this work. It appears to be a important point to address in the future for a better understanding of the co-sintering.

Zusammenfassung

Die vorliegende Arbeit behandelt das Thema Kosintern. Ziel ist, die bisher verwendeten komplexen Sintermodelle durch ein einfacheres Verfahren zu ersetzen. Zusätzlich wird ein Messverfahren entwickelt, um die zur Beschreibung des Kosinterns erforderlichen Messdaten zu erhalten. Der experimentelle Ansatz beinhaltet Sinterungen ohne Last sowie mit einachsiger Belastung. Das Verfahren ermöglicht die Vorhersage (i) der Sinterkinetik und (ii) der viskosen Moduli.

Um den Sinterpfad von Grünkörpern vorhersagen zu können, wird ein Kennfeld verwendet: das *Master Sintering Diagram* (MSD). Das MSD wird durch eine allgemeine Gleichung für das Festphasensintern definiert und lässt sich damit für alle thermisch aktivierten Diffusionsmechanismen anwenden. Die Vorhersage gilt für breite Bereiche von Temperaturen und äußeren Lasten.

Eine neuartige Messmethode für die Erfassung der viskosen Moduli wird in der Arbeit entwickelt: das *cyclic unloading dilatometry*. Sie besteht in Hot-forging Versuchen mit konstanter Last, bei denen die sinterenden Proben regelmäßig für kurz Zeit entlastet werden. Die Versuche werden mit konstanter Aufheizrampe durchgeführt, so dass die viskose Moduli für breite Bereiche von Temperaturen und Dichten erfasst werden. Ein Vorteil dieser Messmethode ist es, die viskosen Eigenschaften von anisotropen Materialien messen zu können.

Das Vorhersageverfahren wird in zwei Schritten geprüft. Erstens werden Vorhersagen vom MSD mit experimentellen Daten verglichen: die maximale Abweichung bei Änderung der Temperaturrampe und der äußeren Last liegt bei 10%. Zweitens werden die viskose Moduli aus dem MSD zur Vorhersage der Krümmung eines Zweischicht-Systems verwendet. Dazu wird ein in der Literatur beschriebenes Modell verwendet. Die qualitative Vorhersage ist gut: die maximale Abweichung zur experimentellen Krümmung liegt bei 27%.

Zusätzlich wird eine Studie über ein Zweischicht-System aus Glas und Keramik vorgestellt, bei dem die Keramik nicht sintert. Es wird gezeigt, dass dieser Fall ohne Hilfe des Sintermodells qualitativ verstanden werden kann. Die Entwicklung der Anisotropie in der Mikrostruktur der keramischen Grünkörper durch die anisotrope Last beim Sintern wird diskutiert. Das volle Verständnis der anisotropen Mikrostrukturentwicklung beim Sintern unter anisotropen Randbedingungen erfordert weitere Arbeiten.

1. Introduction

This work deals with the sintering process of multi-material composites. At least one materials of these materials is porous before sintering. During the firing step, named co-sintering, transient stresses generally occur within each part of the composite due to the mismatching shrinkage speeds between both materials. These stresses lead to macroscopic defects like delamination, crack formation or strong alteration of the final density. Since they damage the integrity or the functionality of the composites, they are source of additional complexities in the successful development of new multi-material structures.

Nowadays the production of such composites becomes successful after long try-and-improve procedures, thanks to firing processes under external loads or use of sacrificial tapes for the minimization of the macroscopic deformations. Great improvement in the fabrication of composites can be assessed by a better knowledge of the co-sintering mechanisms and by the control of the stress generation. For this purpose, it is essential:

1. to identify the parameters playing a role in the generation of these stresses,
2. to create a simulation tool supporting the engineering of new composites by predicting stress and macroscopic deformation (warping, barrelling, twisting,...). The simulation tool must be sufficiently flexible to enable the variation of some or all identified parameters in order to diminish the composite deformations.

Stresses during co-sintering

A literature overview gives already a relatively clear picture about the keys having a major role on the stress generation during co-sintering: taking out pure geometrical aspects, the stresses are generated by the shrinkage rate mismatch existing between two parts of an heterogeneous structure [1, 2, 3, 4]. Thus further considerations on the shrinkage kinetics are necessary to understand the keys of co-sintering.

Sintering results from the thermodynamically driven reduction of the total surface energy of the system. Next to the densification by minimization of the total free surface i.e. smaller pore fraction, the diminution of the total area of interfaces occurs i.e. less and shorter grain boundaries: this is the coarsening and the grain growth [5, 6, 7]. The sintering kinetics varies mainly with three

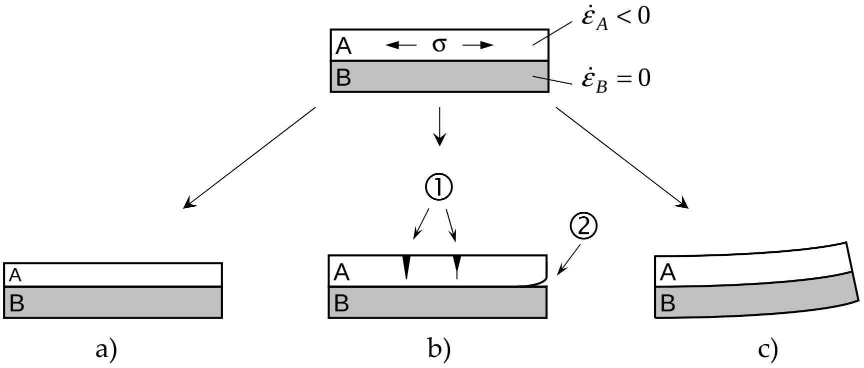

Figure 1.1.: Sketch of the co-sintering of a layered composite with a shrinking tape A and a non-shrinking tape B. The stresses generated by the shrinkage rate mismatch ($\Delta\dot{\varepsilon}$) can lead to a) no radial deformation through enhanced axial (z-) shrinkage, b) generation of cracks (1) and delamination (2) and c) warpage.

independent categories of parameters having multiple interactions. These parameters are briefly enumerated here:

a) *material and microstructure*: the shrinkage rate is (i) specific to one material or one mixture of materials (including additives), depends (ii) on the powder characteristics like particle size distribution [8] or specific surface energy of the powder [9] and (iii) on the particle packing [10, 11] including density, particle orientation [12] and homogeneity of the green-body, all strongly depending on the green-body processing [13, 14].

b) *temperature*: matter re-distribution takes place within the green-bodies during sintering. Several mechanisms (surface diffusion, lattice diffusion and grain-boundary diffusion for instance) are thermally activated. Furthermore, the diffusion is a time dependent process making the sintering kinetics reliant to the temperature path like heating ramp and holding time: this is named the thermal memory of the material (or thermal history).

c) *external stresses*: when they are applied, external stresses are transmitted to each grain [15] and generate stress-oriented faster or slower matter fluxes [16, 17] in addition to sintering. The instant macroscopic strain rate results from the sum of the sintering shrinkage and the macroscopic creep [18][19]. If the external forces are non-hydrostatic and applied during long periods, the microstructure becomes remarkably anisotropic with the orientation of the pores (along the load axis in case of uniaxial compression) [20]. If the external forces are suddenly totally released, the strain rate does not instantaneously return to the free sintering rates [21], due to the loading memory of the material (or loading history).

Simulation tool for co-sintering and material models

Many layered multi-materials can be designed: association of glass, metal and/or ceramic in form of thin and thick films on rigid substrate, symmetric and asymmetric parts, juxtaposed elements, etc. Therefore it is valuable to build the simulation tool for co-sintering on a flexible base being able to consider any geometry and any dimension. For this purpose, finite element simulation (FEM) offers a sufficient flexibility. However, FEM requires external inputs (the material model) defining the sintering behaviour of each material. This material model confers a certain flexibility regarding the parameters previously cited, hence must be predictive.

One type of sintering material models is the ab-initio models, starting at the particle level and scaling up to the macroscopic behaviour, like Riedel's model [22, 23, 24] later extended by Kanters [25] for sintering nano-powders. Particle geometries, particle packing, material transport mechanisms must be known or assumed and the quantitative material fluxes need to be assessed thanks to thermodynamic considerations. Creep behaviour was integrated in these models. However the major complexity of these models is the accurate description of the on-going mechanisms using simplified powder topologies (for example spherical particles), making assumptions on the sintering mechanisms and being based on numerous physical quantities very difficult to assess experimentally (diffusion coefficients, boundary mobility, surface energies,...).

The kinetic field (KF) of Palmour [26] and the Master Sintering Curve (MSC) of Johnson [27] are alternatives for the modelling of sintering kinetics. Both rely on the information contained in macroscopic data. They require no microscopic considerations and only few assumptions about the sintering mechanisms. The sintering kinetics (densification rate) is predicted by time iterations within the field limits knowing temperature and temperature rate (set by the user) and a starting density. Both approaches differ by their approach and their representation: the MSC was constructed on a scientifically accepted approach and required the adjustment of one free parameter (the activation energy). In contrast the KF being often criticized for the lack of strong scientific background in its original formulation had the advantage to be free of adjusting parameter. A 3D extension of the MSC was reported with the integration of external stresses [28], whereas three years back, no reference about a KF for loaded sintering was found in literature.

Development of a new material model for sintering

Due to its simplicity and its apparent efficiency, the KF deserves more attention. The existing state of development suggests a large potential in the sintering kinetics under external load. The KF was reformulated based on a generalized equation for diffusion mechanisms making the field suitable for sintering kinetics under external loads [29]. It enables the construction of a predictive model for the sintering kinetics of one specific green-body with variable temperatures and variable external loads. The 3D-kinetic field was renamed the *Master Sintering Diagram* (MSD).

For co-sintering cases, predictions of the sintering kinetics necessitate the knowledge of the stresses within each part of the composite. Hence the mechanical properties of the material during the sintering process must be determined, namely the bulk (K_v) and shear (G_v) viscosities (also alternatively given by the uniaxial viscosity η_v and the viscous Poisson ratio ν_v). Bordia and co-workers provided the theoretical framework for the linear viscous behaviour [30] and almost 20 years later for anisotropic sintering bodies[1] [31].

Experimental characterization of the viscous behaviour during sintering

After Bordia, the viscous moduli of a material can be determined from the change in strain rate occurring with a sudden change of stress. Searching in the mechanical engineering, there are plenty of existing methods to serve this purpose. However, in the case of sintering materials, only a few become adequate regarding mainly the poor mechanical properties of porous structures and the complexity of in-situ measurements at high temperatures in closed furnaces. In literature, characterizations in tension are almost non-existent, only two examples were found in the literature with the work of Gregg [32] on porous copper compacts and Sglavo et al. [33] on pre-sintered Al_2O_3 compacts. Bending test methods are well adapted to flat geometries like tapes, however the sample thickness undergoes alternatively tension and compression. Finally, the uniaxial compression test is the most convenient and also the most commonly utilized. Large ranges of load can be investigated and the material response can be monitored in the stress direction and in the normal plane to the stress.

Due to the developing anisotropy during hot-forging measurements (sintering under non-hydrostatic compression), only a few groups achieved the successful mechanical determination of both viscous moduli using uniaxial compression tests. Two distinct loading modes were used and are shortly described here:

a) *the cyclic loading* was developed first by Cai et al. [34] using porous ceramics and repeated later by Gillia et al. [35] with porous W-carbides. The method was based on the succession of short loaded and long unloaded sequences in order to obtain the mechanical response of a material with time-, temperature- or density dependence. The long unloaded periods were intended to let the material recover from the previous loading period and thus to exhibit again an isotropic microstructure before the next loaded sequence.

b) *the discontinuous hot forging* was based on isothermal experiments with the application of one constant load at different stages of sintering [36]. Due to the developing microstructure anisotropy, the method was valid strictly shortly after the load application. The measurement had to be repeated several times for each temperature of interest and for the whole density range. The advantage of this method is the clear demonstration of the effect of the microstructure state on the uniaxial viscosity, i.e. the less porous the sample is, larger is the uniaxial viscosity. This effect is directly related to the steadily decrease of the compressibility of the porous body as the pore fraction is reduced. One disadvantage of this method is the large number of measurements that are required to construct a reliable viscosity map for co-sintering cases. Additionally the method was applied during isotherms neglecting thereby the pre-sintering during the heating period and ignoring variation of temperature profile (thermal history). This was identified as a lack of information for further simulation of co-sintering.

---

[1] With "anisotropic sintering bodies", Bordia meant either an anisotropy existing in the green-body or an anisotropy generated during sintering by non-hydrostatic stresses (the loading memory).

Goals of the work and thesis content

This work aimed at (1) the establishment of a material model to predict the material behaviour during sintering under external stresses and (2) the development of the experimental method required by the material model. The model must deliver the sintering kinetics and the viscous moduli of porous bodies during thermal treatments.

The Master Sintering Diagram (MSD) is proposed as a judicious solution for the prediction of sintering kinetics: it is simple experimental approach without many assumptions and without free parameters delivering the desired sintering kinetics. The background and the construction of the MSD are detailed in Chapter 2.

None of the previously mentioned characterization methods for viscous moduli is perfectly adapted to the requirements of real co-sintering cases, i.e. taking into account the thermal memory and the loading memory over the full of density range. A new experimental alternative is reported in this work. The procedure and associated characterization methods are presented in Chapter 3.

Three material systems are available for the investigations in this work:

- a partially stabilized zirconia powder (single material),
- bi-layers made of a zirconia tape on an alumina tape,
- bi-layers made of a porous glass-ceramic tape on a non-shrinking alumina tape.

The work is built on the following sequence: experimental data, model construction, validation (see Figure 1.2). Good input data is extremely important since it ensures accurate predictions. The whole set of data is acquired first for a single (defect free) pressed compacts (3 mol%-Y_2O_3-stabilized zirconia) and is presented in Chapter 4 together with the construction of the MSD, the determination of the viscous moduli and a few microstructure investigations.

The MSD is validated by comparing several predicted sintering kinetics and the corresponding experiments with variations of the thermal profiles and of the loading states. The experimentally determined viscous moduli are used for the warpage prediction of co-sintering of the alumina and zirconia tapes. The warpage of a bi-layer Al_2O_3-ZrO_2 is analytically calculated and compared with the experimental warpage. The two-part verification of the model is reported in one extra chapter, the Chapter 5.

Finally, the co-sintering case with the glass-ceramic tape on a non-shrinking alumina tape is reported in Chapter 6.

A discussion of the experimental results is made in Chapter 7.

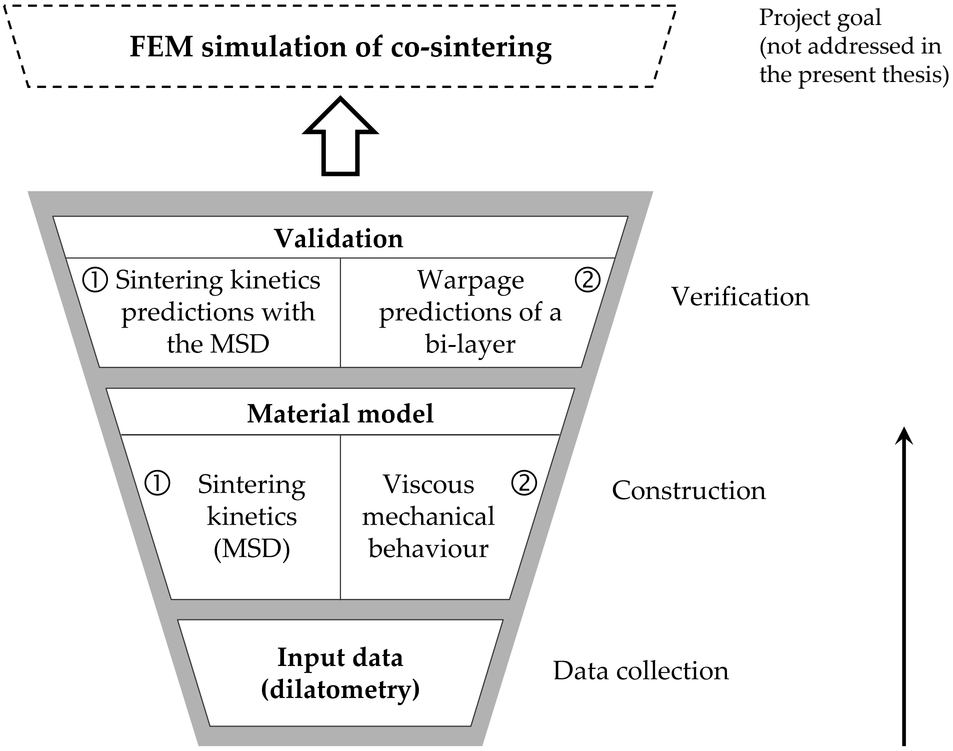
FEM simulation of co-sintering
Project goal
(not addressed in
the present thesis)
Validation
① Sintering kinetics predictions with the MSD
Warpage predictions of a bi-layer ②
Verification
Material model
① Sintering kinetics (MSD)
Viscous mechanical behaviour ②
Construction
Input data (dilatometry)
Data collection

Figure 1.2.: Scheme describing the present work: the experimental data are used for the generation of the material model with (1) the MSD and (2) the viscous moduli. The sintering kinetics and the viscous moduli are validated in two distinct steps. The overall aim of the project is to generate a material model for the FEM simulation of co-sintering (not addressed in this work).

2. Material model description

Instead of a classical ”theory” part, this second chapter focuses on the description of the material model developed in this work. The readers who miss basic understanding of sintering are advised to refer to well-written and explicative books and reviews [5, 6, 7, 37, 38].

2.1. Sintering kinetics with the Master Sintering Diagram (MSD)

The MSD is an experimental approach to describe the sintering kinetics of one specific green-body for any temperature, any load, considering thermal and loading histories [29].

2.1.1. Assumptions

- *The model assumes the control of free sintering by thermally activated diffusion.*

In early contributions on solid-state sintering, several authors elaborated mathematical expressions for diffusion controlled material transport (see Table 2.1). These models were restricted to specific matter displacement mechanisms and were based on geometric considerations (like 2 sphere models). By comparing all these models, the same mathematical form can be recognized:

$$-\dot{\varepsilon} = \frac{C_1(\rho)D}{TG^n} \tag{2.1}$$

$\dot{\varepsilon}$: macroscopic shrinkage rate (during sintering $\dot{\varepsilon} < 0$)
$C_1(\rho)$: material parameter including all microstructural constants
D: diffusion coefficient
G: grain size
n: grain size exponent function of the sintering mechanism
T temperature

Table 2.1.: Equations to describe the shrinkage by diffusion controlled solid-state sintering for initial, intermediate and final sintering stages and for grain-boundary (GB) or lattice diffusion

Sintering stages	**Ref.**	**Diffusion mechanisms**	**Equations**
Initial	[39]	Lattice	$\frac{dV}{dt} = -\frac{720D\gamma\Omega}{G^3kT}$
	[40]	GB or lattice	$\frac{\Delta V}{V_0} = \left(\frac{K\gamma\Omega D}{G^pkT}\right)^{3m} \cdot t^{3m}$ with K, p, m: numerical constants
	[41]	GB or lattice	$\frac{\Delta V}{V_0} = \frac{-3n}{8}\left(\frac{80\gamma a^3 D}{G^3kT}\right) \cdot t^{4/5}$ with n: number of contact per sphere; a: atomic radius
Intermediate	[42]	GB	$\frac{\Delta V}{V} = \left(\frac{\Delta V}{V}\right)_0 - \frac{21\pi}{0.04\sqrt{2}}\frac{D\gamma\delta\Omega}{bkT}\left(\frac{1}{l_0} - \frac{1}{l}\right)$
		Lattice	$\frac{\Delta V}{V} = \left(\frac{\Delta V}{V}\right)_0 - \frac{12}{8\sqrt{2}\cdot 145}\frac{D\gamma B\Omega}{bkT} ln\left(\frac{l^3}{l_0^3}\right)$ with B: geometrical factor; b: temperature-dependent constant; l: grain length as function of time so that $l^3 = l_0^3 + bt$; l_0: initial grain length
	[43]	GB	$\frac{dV}{dt} = \frac{4\pi D\Omega^2\gamma C_0}{kTr}$
		Lattice	$\frac{dV}{dt} = \frac{112\pi D\gamma\Omega}{kT}$ with r: cylindrical pore radius; C_0: initial vacancy concentration
Final	[43]	GB and Lattice	$\frac{\Delta V}{V_0} = \frac{6\pi D\gamma\Omega}{l^3kT}\Delta t$

Nomenclature of characters in commun

$\Delta V/V_0$: volume shrinkage; γ: surface energy; Ω: vacancy volume; D: Diffusion coefficient of the considered diffusion mechanism; δ: grain-boundary width; G: grain size; k, T, t have the usual meaning with

$$D = D_0 \exp\left(\frac{-E_a}{RT}\right) \tag{2.2}$$

D:	diffusion coefficient
D_0:	pre-exponential diffusion coefficient
E_a:	activation energy for sintering
R, T	have the usual meaning

In that way, Eq. 2.1 becomes suitable for the complete sintering process whatever lattice or GB diffusion is active.

■ *The model assumes that creep is diffusion controlled.*

Nabarro-Herring [16] and Coble [17] presented mathematical expressions respectively for grain-boundary diffusion and lattice diffusion controlled creep (see Table 2.2). A generalized form for diffusion creep can be derived, by writing:

$$-\dot{\varepsilon} = \frac{C_2(\rho, \sigma, G^{-n})D}{T} \tag{2.3}$$

where C_2 is a parameter depending on the density ρ, the external stress σ and the grain size G.

Table 2.2.: Diffusion creep models

Diffusion mechanism	**Creep equation**	**Ref.**
Grain-boundary	$\dot{\varepsilon} = 148\sigma \cdot D\delta\Omega/\left(G^3kT\right)$	[17]
Lattice	$\dot{\varepsilon} = 10\sigma \cdot D\Omega/\left(G^2kT\right)$	[16]

2.1.2. How to construct and interpret the MSD?

■ *Free sintering kinetics and constrained sintering kinetics in one plot*

With the assumptions given in Section 2.1, free sintering and constrained sintering can be described with one unique equation. Rearranging Eqs 2.1, 2.2 and 2.3, a generalized Arrhenius form is obtained:

$$ln\left(\frac{-T \cdot \dot{\varepsilon}}{C_0}\right) = ln\left(\frac{C(\rho, G^{-n})}{C_0}\right) - \frac{E_a}{RT} \tag{2.4}$$

where C is a parameter varying with density (or strain) and grain size only and $C_0 = 1$ K/s. In the graphical representations in this work the factor C_0 becomes implicit despite its essential role for mathematical rigour.

Considering equal density values and equal grain size, the so-called iso-density points, C is constant and Eq. 2.4 describes a linear function with the inverse of temperature. Its slope is $-E_a/R$ where E_a is the activation energy for sintering. Interpretation of the activation energy values must take into account the possible simultaneous contribution of surface, grain-boundary and lattice diffusions (although surface diffusion does not directly participate to shrinkage). Therefore the E_a values determined with these plots do not necessarily express one unique mechanism and the term *apparent activation energy* is favoured.

If Eq. 2.4 were experimentally shown to be non-linear, then several assumptions made in this model could be discussed:

- thermally activated diffusion is not the only sintering mechanism,
- there is a change in sintering mechanism with temperature and/or with temperature ramp.

■ *Which experimental data are needed to construct the MSD?*

For the experimental construction of the MSD, the strain rate as function of the temperature is needed for free sintering experiments and for sintering experiments under external load (constrained sintering). No further knowledge on the material properties (diffusion parameters, matter mobility,...) and no consideration of diffusion mechanism is required. Two parameters are experimentally varied:

1. the thermal treatment by using several constant heating rates,
2. the external load.

The hot-forging (uniaxial compression) is an experimentally convenient method to apply external loads on a sample during sintering. Since the uniaxial load generates anisotropic shape deformation, the sintering kinetics in the load direction has to be distinguished from the sintering kinetics in the normal plane to the load. Moreover, marking points of equal strain on the MSD (named iso-strain points) has more sense than marking points of equal density.

A stepwise construction of the MSD is given in Figure 2.1.

■ *How to predict the sintering kinetics with the MSD?*

The prediction of the sintering kinetics is based on a time-iterative process (see Figure 2.2). For each starting point P_t the temperature T, the external stress σ, the strain ε and the strain rate $\dot{\varepsilon}$ are known (for the onset of sintering, $\varepsilon = 0$ and $\dot{\varepsilon} = 0$).

For a small time increment dt, a new temperature and a new strain are calculated (see graphical solution in Figure 2.3). The new strain value belongs also to an intermediate iso-strain line which position is linearly interpolated between two other iso-strain lines ε_1 and ε_2. The new temperature $T + dT/dt$ and the new strain value $\varepsilon + d\varepsilon/dt$ define the location of the new point P_{t+dt} whose

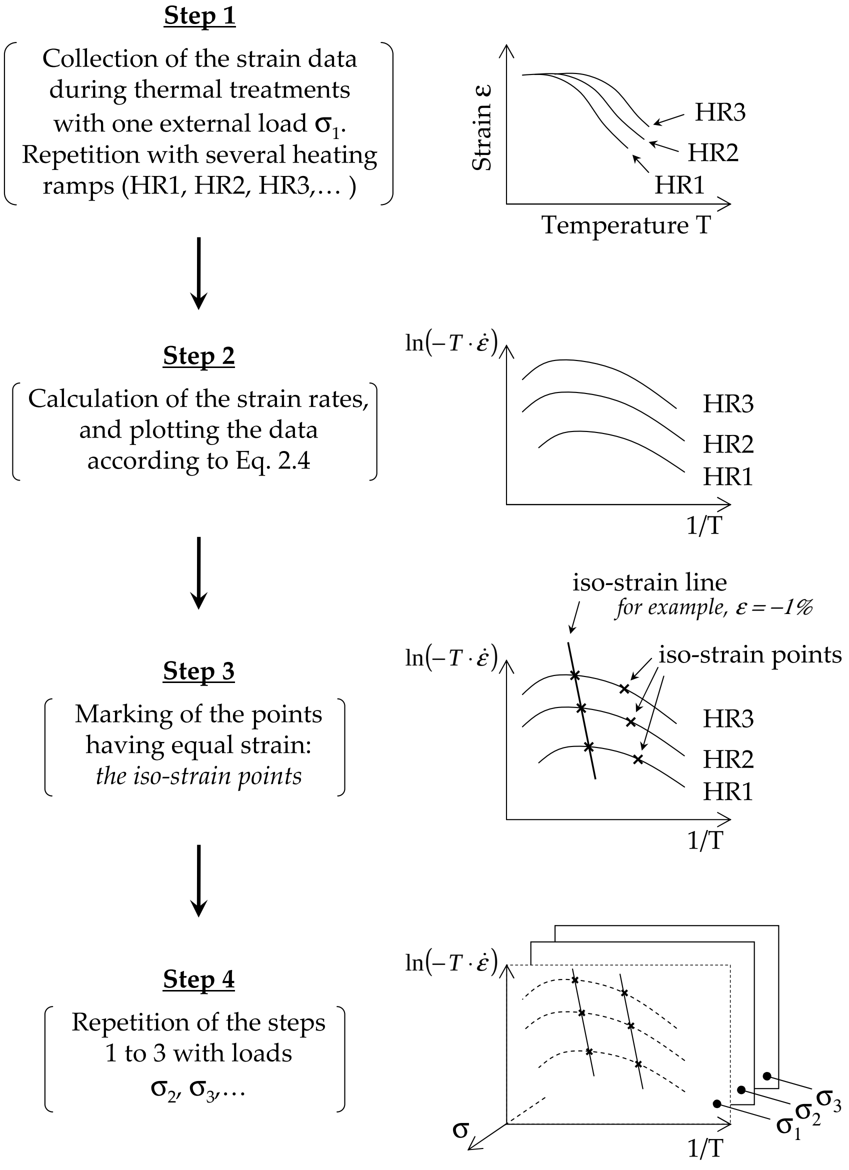
Step 1
Collection of the strain data during thermal treatments with one external load σ_1. Repetition with several heating ramps (HR1, HR2, HR3,…)
Strain ε
HR3
HR2
HR1
Temperature T
Step 2
Calculation of the strain rates, and plotting the data according to Eq. 2.4
$\ln(-T \cdot \dot{\varepsilon})$
HR3
HR2
HR1
1/T
Step 3
Marking of the points having equal strain: *the iso-strain points*
iso-strain line
for example, $\varepsilon = -1\%$
iso-strain points
$\ln(-T \cdot \dot{\varepsilon})$
HR3
HR2
HR1
1/T
Step 4
Repetition of the steps 1 to 3 with loads σ_2, σ_3,…
$\ln(-T \cdot \dot{\varepsilon})$
σ
1/T
σ_1
σ_2
σ_3

Figure 2.1.: Schematic construction of the MSD in 4 steps (ε: strain; $\dot{\varepsilon}$: strain rate; T: temperature; HR: heating ramp; σ: external stress)

$$P_t \begin{pmatrix} T \\ \sigma \\ \varepsilon \\ \dot{\varepsilon} \end{pmatrix} \xrightarrow{t+dt} \begin{pmatrix} T + dT/dt \\ \sigma + d\sigma/dt \\ \varepsilon + d\varepsilon/dt \\ \end{pmatrix} \longrightarrow P_{t+dt} \begin{pmatrix} T_{t+dt} \\ \sigma_{t+dt} \\ \varepsilon_{t+dt} \\ \dot{\varepsilon}_{t+dt} \end{pmatrix}$$

Figure 2.2.: Increment method of the MSD with one time increment *dt* of the temperature T, the external stress σ and the strain ε (see graphical representation in Figure 2.3)

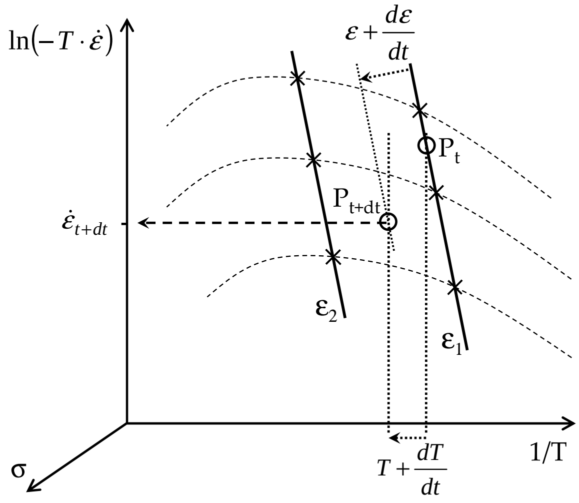
$\ln(-T \cdot \dot{\varepsilon})$
$\varepsilon + \frac{d\varepsilon}{dt}$
P_t
P_{t+dt}
$\dot{\varepsilon}_{t+dt}$
ε_2
ε_1
σ
$T + \frac{dT}{dt}$
1/T

Figure 2.3.: Graphical representation of the time-iteration procedure used to predict the sintering kinetics with the MSD between two indicative iso-strain lines ε_1 and ε_2. The increment of external stress σ works according to the same process (see Figure 2.2)

temperature, strain and strain rate are known for the next time iteration. The load is implemented according to the same principle with interpolation between iso-strain lines.

The positive radial strain rates (diameter expansion) are not directly defined in the MSD due to trivial mathematical reasons (see Eq. 2.4). The predictions of positive strain rates are achieved by adding a mathematical condition on the density: when the full density is reached, creep in radial direction must respect the volume conservation.

2.2. Characterization of creep during sintering

2.2.1. Viscous moduli

The viscous moduli quantify the ability of one specific body to deform under external stress(es). The compressive (or bulk) viscosity and shear viscosities are characterized by the bulk modulus (K_v) and shear modulus (G_v) respectively. They were mathematically expressed for an isotropic body with [37]:

$$G_v = \frac{\eta_v}{2\,(1+\nu_v)} \tag{2.5}$$

and

$$K_v = \frac{\eta_v}{3\,(1-2\nu_v)} \tag{2.6}$$

where the uniaxial viscosity η_v gives the mechanical resistance of the material in the direction of the uniaxial stress and the viscous Poisson ratio ν_v gives the mechanical behaviour in the normal plane to the load application. Stating G_v, K_v and η_v are strictly positive [44], Eqs. 2.5 and 2.6 give the domain of definition $-1 < \nu_v < 0.5$. However, in the case of sinter forging experiments, the viscous Poisson ratio is to be positive [45], i.e. $0 < \nu_v < 0.5$. When $\nu_v = 0$, the uniaxial stress has no effect onto the strain rate in the normal plane to the load.

During sintering, the viscous moduli vary with:

a) *the temperature*: since creep is diffusion controlled, G_v and K_v are temperature dependent. With increasing temperature, lower viscosity can be expected.

b) *the densification* due to (i) the increase of grain-grain contact surfaces and (ii) the reduction of pore fraction. Moreover the densification is linked to the thermal treatment (see Eq. 2.1).

c) *the grain size* due to the number of grain-boundaries. With larger grain size, higher viscosities can be expected.

d) *the degree of anisotropy* due to formation of pore and grain anisotropy under non-hydrostatic external loads [46].

2.2.2. Principle of the cyclic unloading method

The cyclic unloading method is close to the hot-forging method, with short periods without load in order to determine the viscous moduli. At the beginning of a measurement, a load is applied on the sample. The load is released during short periods several times during the measurement. At each unloading cycle, the interpolated loaded strain rates and measured unloaded strain rates are determined (see Figure 2.4). The viscous moduli are calculated using the linear isotropic viscous constitutive equations [30, 45]. Despite probable orientation of grains and pores after long uniaxial compressive load application, these equations are assumed to be valid since the microstructures in the loaded state and the unloaded state are the same. For a cylinder under uniaxial compression in the z-direction (axial), they are given by:

$$\Delta\dot{\varepsilon}_r = \frac{d\varepsilon_r^{loaded}}{dt} - \frac{d\varepsilon_r^{unloaded}}{dt} = -\frac{\nu_v}{\eta_v}\sigma_z \tag{2.7a}$$

$$\Delta\dot{\varepsilon}_z = \frac{d\varepsilon_z^{loaded}}{dt} - \frac{d\varepsilon_z^{unloaded}}{dt} = \frac{1}{\eta_v}\sigma_z \tag{2.7b}$$

where σ_z is the stress applied in the z-direction, ε is the strain and $\dot{\varepsilon}$ the associated strain rate annotated with the subscripts z and r for the axial direction and radial direction respectively.

The dependence of the viscous moduli on temperature is assessed by performing measurements over a large temperature range with a constant heating rate. The correlation between the viscous moduli and the density can be done with the strain data of the dilatometry curves.

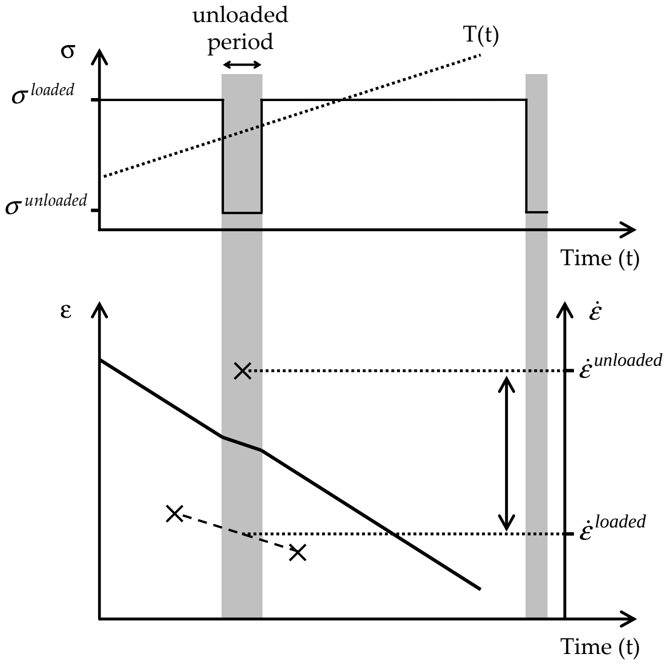
unloaded period
T(t)
σ
σ^{loaded}
$\sigma^{unloaded}$
Time (t)
ε
$\dot{\varepsilon}$
$\dot{\varepsilon}^{unloaded}$
$\dot{\varepsilon}^{loaded}$
Time (t)

Figure 2.4.: Graphical representation of the experimental method for the determination of the strain rates during cyclic unloading method

3. Experimental techniques

3.1. Materials

3.1.1. Partially stabilized zirconia

A commercial partially stabilized zirconia powder with 6.5 wt% of Y_2O_3 (Unitec) is chosen for this study. The powder is first milled in an attritor (with 2 mm milling balls during one hour) in a wet mixture of isopropanol and vegetal oleic acid (Merck; concentration relative to the powder specific surface: 8 µmol/m^2). After drying at 80 °C, agglomerates are crushed and sieved (180 µm mesh). Some of the powder is thermally treated at 400 °C for 1 hour to burn out the organic part for the XRD investigations.

The powder size after attrition is experimentally determined in pressed green-bodies (see the procedure for sample preparation in the following paragraph) using the linear intercept analysis (see Section 3.3.2) on SEM images. The cross-sections of the samples are prepared with the CSP method (see an examplary image in Figure 3.1 and the experimental results in Section 4.4.1).

Sample shaping is carried out using cold isostatic pressing (CIP) in two steps. First the powder is filled in a silicon mould and pressed with 45 MPa. Afterwards the silicon mould is removed and another pressing step up to 200 MPa is carried out in order to improve the pressing homogeneity. The pressed cylinders are 20 mm in diameter and 50 mm in length. Samples are debinded and pre-sintered at 850 °C for 1 h in order to increase the strength of the bodies and to prevent dramatic failures during the final preparation step. The samples are machined down to 7.5 mm in diameter and 17 mm in length considering plane parallel surfaces (using a sharp blade on the turning machine). Plane-parallel end faces are achieved with a cutting saw. The final green density is geometrically determined (with more than 50 samples): (3.60 ± 0.01) g/cm^3 which is equivalent to 59.0% in relative density (indicative theoretical density 6.1 g/cm^3). The homogeneity of the green-body is controlled using the microscopy technique (SEM) on pre-sintered bodies (see Figure 3.1). The green-body preparation necessitates the use of the CSP method (see complete description in Section 3.3.2) due to the weakness of the structure.

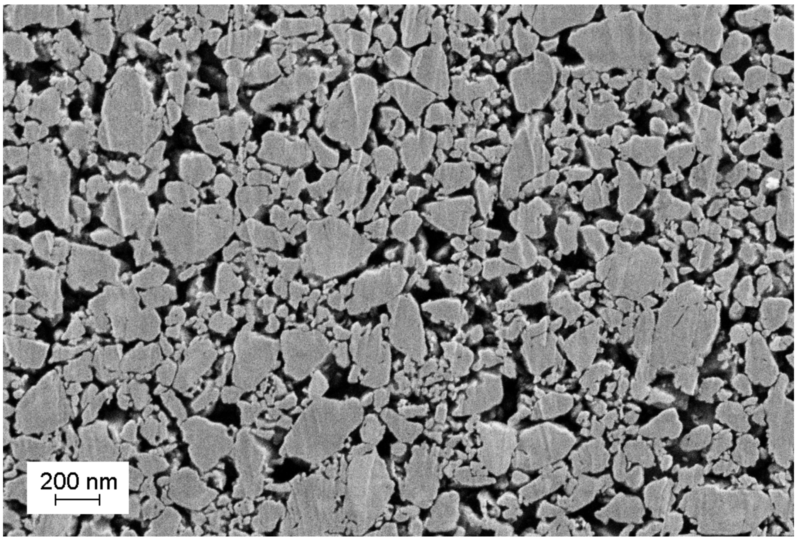

Figure 3.1.: SEM image of the ZrO_2 green-body after pre-sintering at 850 °C, in grey the ZrO_2 grains and in black the voids between the grains (SE detector, Magnification 50000X, WD 3 mm, voltage 1.5 kV)

3.1.2. Bi-layer alumina/zirconia

The fabrication of bi-layers is carried out by association of one pure Al_2O_3 tape and one fully stabilized ZrO_2 tape (Kerafol, Germany). These materials are chosen because (i) the sintering mechanisms of these materials are diffusion controlled; (ii) the materials are expected to show a sufficient strain rate mismatch; (iii) the materials are simple, without glass formation, crystallization and phase change. Some additional information delivered by the supplier is listed in Table 3.1.

Two sorts of samples are fabricated: (1) mono-component stacks of only A-tape and only B-tape and (2) asymmetric composites (type bi-layer AB). Mono-component stacks are fabricated by punching 8 mm discs in the tapes and then by piling them up in a matrix (no attention is paid at the orientation of the casting direction, i.e. the tapes are randomly oriented). Stacks are heated up at 85 °C for 30 min and laminated with 4.5 MPa during 10 min using a pressing device (Zwickiline 2.5 kN, Zwick Roell). The final stacks are 17 mm high. The green densities are 2.10 g/cm^3 ($\approx$ 52 vol%) for the Al_2O_3 stacks and 2.51 g/cm^3 ($\approx$ 42 vol%) for the ZrO_2 stacks. Asymmetric

Table 3.1.: Characteristics of the tapes used for the bi-layers

	Tape A	**Tape B**
Material	99.90% pure Al_2O_3	8Y-ZrO_2
Thickness	170 µm and 350 µm *	200 µm
Grain size	$0.3 < d_{50} < 0.4$ µm	d_{50}=0.6 µm
Solid-loading	80 wt% ($\approx$ 52 vol%)	80 wt% ($\approx$ 42 vol%)

* Tape A is available in two thicknesses: 170 µm and 350 µm

bi-layers are prepared following the same procedure in order to conserve the particle packing in the green-bodies. Assemblies with 3×Al_2O_3 (350 µm) and 1×ZrO_2 (200 µm) are fabricated and their dimensions were (45×5) mm^2.

3.1.3. Bi-layer glass-ceramic/alumina

The glass-ceramic (GC) is a SiO_2-CaO-Al_2O_3-B_2O_3 glass[1] mixed with Al_2O_3 particles in proportion 60 vol% and 40 vol% respectively. The material is available in 190 µm tapes (internal Bosch supplier). In addition to sintering this material undergoes crystallization from a chemical reaction between the glass and the Al_2O_3 particles. During crystallization, change of the glass composition and reduction of the glass fraction is expected, leading to the variation of the apparent viscosity during the thermal treatment.

The second material used in the fabrication of the composite is a porous 290 µm thick Al_2O_3 tape (particle size $\approx$ 0.4 µm). The onset of shrinkage of this material is expected to be above the sintering temperature of the glass-ceramic (above 890 °C).

Two samples types are prepared to satisfy the requirements related to the measuring setups:

1. the material becoming soft in temperature, thicker tapes exhibit experimentally better stability during free sintering measurements (see standing tapes in Section 3.2.4.1). To make the tapes thicker, two glass-ceramic tapes are laminated with 180 MPa at 80 °C. Two formats are cut out using a sharp heated blade at 60 °C: (25×15×0.28) mm^3 for the free sintering measurements and (45×5×0.28) mm^3 for the bending measurements.
2. the fabrication of the bi-layer is done by lamination of one GC-tape and one Al_2O_3-tape. The lamination and cutting conditions are kept constant for all samples in order to overcome any influence of the sample fabrication.

Finally, samples are debinded up to 400 °C for 1 h (108 K/min up to 100 °C, 450 K/min up to 250 °C, 108 K/min up to 400 °C). The density after debinding is (1.87 ± 0.08) g/cm^3.

3.2. Optical dilatometry

3.2.1. Instrument

The optical dilatometer TOMMI[2] is used in this work (see illustration in Figure 3.2). The hot chamber of dimensions (250×150×200) mm^3 (width, depth, height) is made of alumina based refractory material. In each corner there are $MoSi_2$ heating elements (4 in total) delivering heat for temperatures up to 1700 °C in the furnace. Two openings closed by quartz glass windows

---

[1] no quantitative information on the glass composition is given in this work

[2] Thermo-Optisches Mess-system MIni, Fraunhofer ISC, Germany

(50 mm in diameter) are aligned on both lateral sides in order to enable in-situ observations in the hot zone. On the left side a halogen lamp illuminates the inside of the furnace chamber and on right side a C-MOS camera with a telecentric objective is placed. The projection of objects along the optical axis is collected by the camera and recorded by the computer. The frequency of image collection is defined in the measurement program, typically one image every 45 s or 60 s [47]. On the top side, another 20 mm opening allows vertical positioning of one stamp as more described in Section 3.2.4.

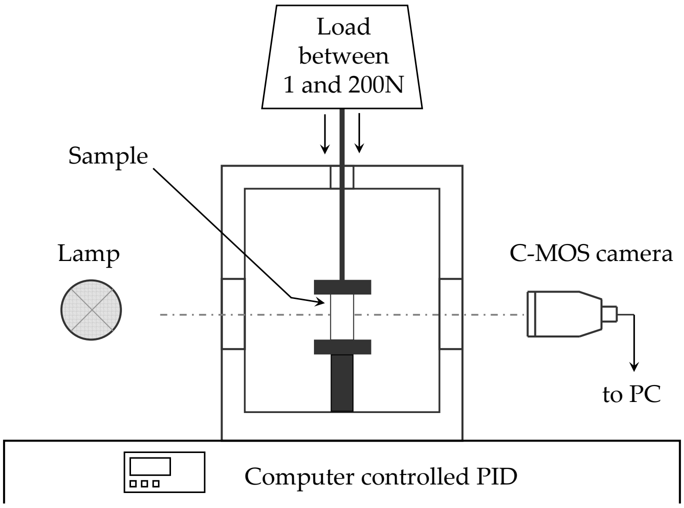

Figure 3.2.: Sketch of the optical dilatometer TOMMI

3.2.2. Image analysis: principle, precision, repeatability and deviation

Dimensional measurements are done with the analysis of the projected image of the sample. A software developed by the Fraunhofer ISC is delivered with the apparatus. The contour of the sample is detected after setting two background windows defining the position of the image baseline. Specific parts of this contour are evaluated on demand setting additional measuring windows like for instance vertical and horizontal distances or radius curvature (see Figure 3.3).

Linear dimensions are delivered by the instrument in the form L/L_0, where L is the instant dimension and L_0 the initial dimension (the term dimension can stand either for the height or for the width of a projected sample). Instant curvatures κ are given in mm^{-1} and defined as the inverse of the radius of a perfect circle.

Samples with rotational geometries or thin samples are favourable in order to reduce measurement errors during eventual sample displacements or tilts in the furnace (shadowing effect). Precision of the apparatus is experimentally estimated using a dense cylinder. During thermal treatment, length and diameter of the sample are recorded. The resolution is calculated from the deviation to a linear regression of each dimension (last square method): the resolution of the apparatus is 2 µm. Similar procedure is carried out for the radius curvature measurement. A perfect cylinder is measured 160 times at room temperature with TOMMI. A standard deviation of 1% is calculated.

The reproducibility between two measurements is also checked doing blank tests (thermal expansion measurements) with dense ZrO_2 pressed samples (see Figure 3.4). Reproducibility below 1% is obtained between the measurements. The difference between the axial and radial measurements is caused by the presence of additional Al_2O_3 discs in the height measurements (see more detailed description of the setup in Section 3.2.4.2).

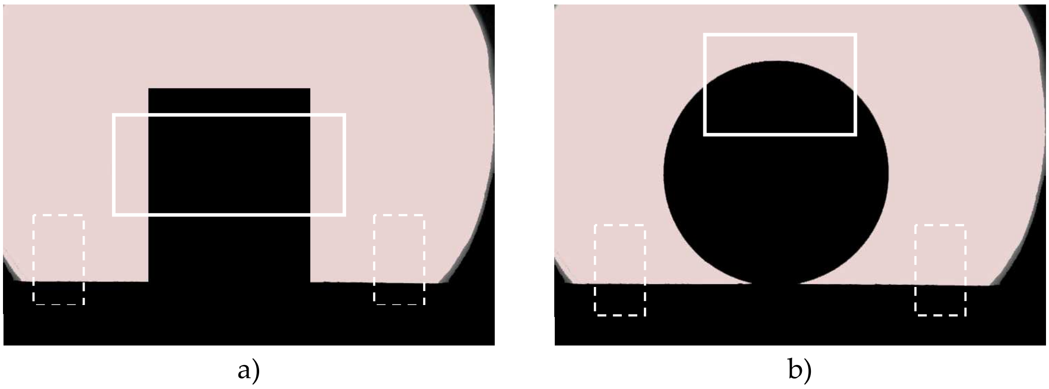

Figure 3.3.: Examples of in-situ images evaluated by TOMMI: a) projection of a standing cylinder and b) projection of the front side of the same cylinder. The dashed-line rectangular areas are the background windows set by the user for the contour finding of the object and the full-line rectangular areas are the measuring windows within which the contour of the sample is evaluated: a) a "width" window and b) a "curvature" window.

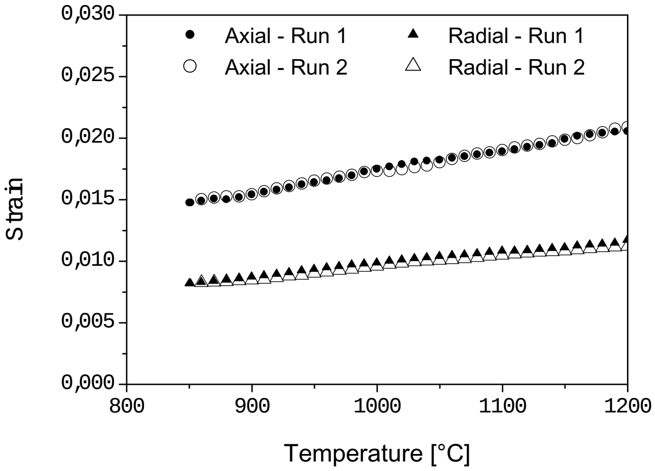

Figure 3.4.: Reproducibility of the thermal behaviour of a fully dense ZrO_2 cylinder in radial and axial direction, with 1 K/min

In this work the correlation between two data sets (two strain measurements for instance) is quantified by the average deviation of the data points and by the maximum deviation.

3.2.3. Data treatment

Linear true strains ε are calculated from the dilatometer output (see Appendix A for the definition of the true strain).

The relative densities are derived from the 2D shrinkage strains assuming isotropic shrinkage in the horizontal plane, i.e. $\varepsilon_x = \varepsilon_y$, using the relation:

$$\frac{\rho}{\rho_0} = exp\left(-2\varepsilon_x - \varepsilon_z\right) \tag{3.1}$$

where ρ_0 is the green density and $\varepsilon_{x,y,z}$ are the true strains in the Cartesian directions x, y, z.

The time differential (the rates) of strains, curvatures and densities are calculated taking the local slope of two consecutive points: $\dot{y} = \Delta y / \Delta t$. Reduction of noise without loss of information is assessed by averaging 5 to 10 data points.

3.2.4. Specific setups

3.2.4.1. Free sintering of tapes

Linear shrinkages are measured placing the tapes vertically in the normal plane to the optical axis (see Figure 3.5). Sample holders have to satisfy two requirements (i) to assess stability of the tape and (ii) to minimize thermal flux between sample and supporting plate. A satisfying shape for the sample holders is obtained by machining Al_2O_3 refractory blocks (4 mm large) with a 400 µm slot

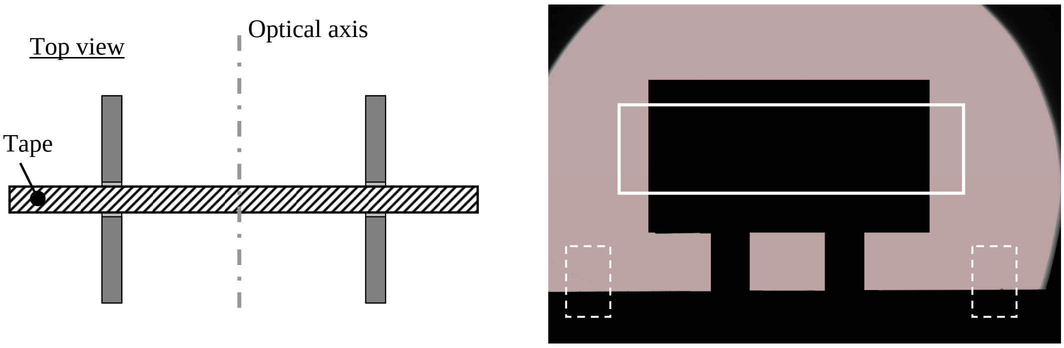

a)

b)

Figure 3.5.: a) Sketch of the setup for the optical free sintering measurements of tapes (top view) and b) the corresponding image taken by the optical dilatometer. The dashed-line rectangular areas are the background windows and the full-line rectangular area is a width measuring window

in the middle. The slots are approximately 5 mm deep and biased at the bottom, so that the tapes are supported by only two contact points and are maintained on each side.

3.2.4.2. Loading setup

Above the hot chamber, a loading setup allows dynamic applications of load between 1 N and 200 N. An Al_2O_3 tube transmits the load from the outside into the hot chamber. At the end of the tube, an Al_2O_3 punch applies the weight to the system {sample/sample holders}.

The loading system is controlled by an electrical motor regulating the tension of a spring and finally the applied load. The electrical motor is calibrated placing a pressure cell in the sample position at room temperature. Maximum of 2% of load variation is tolerated above 10 N, 10% by 10 N and 100% by 1 N. No better regulation at low load levels is achieved since the motor specifications are more suitable for high load ranges. However, loads between 1 N and 10 N correspond to 20 kPa to 200 kPa respectively (related to the initial sample diameter). This compression range remains below the sintering stresses of ceramic materials typically in the range 1 MPa to 5 MPa, therefore strain rates are expected to be insensitive to compression stresses up to 10 N.

Any displacements and tilting of the {sample/sample holders} during sintering are difficult to prevent and generate significant imprecision mostly in the height measurement due to a shadowing effect. For instance, when a 20 mm broad supporting plate undergoes a lateral tilt of 1°, an apparent height reduction of about 170 µm is generated (see Figure 3.6.a). Maximization of the precision in the height is assessed using “V-shape” sample holders (see Figure 3.6.b). The samples are placed onto the flat surface in the middle part and the height measured on each side of the sample. Using this kind of sample holders, the shadowing effect in the same tilting conditions is overcome. Additionally, on top and bottom of the sample, between the sample and the sample holders, one

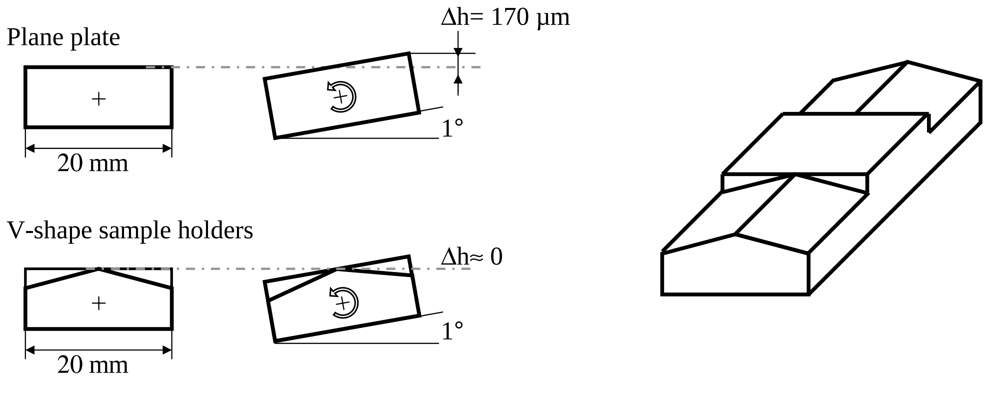

a) b)

Figure 3.6.: a) Illustration demonstrating the measurement error done with a quadratic supporting plate undergoing tilting of 1° and the improvement using V-shape sample holders and b) 3D-representation of the V-shape sample holders

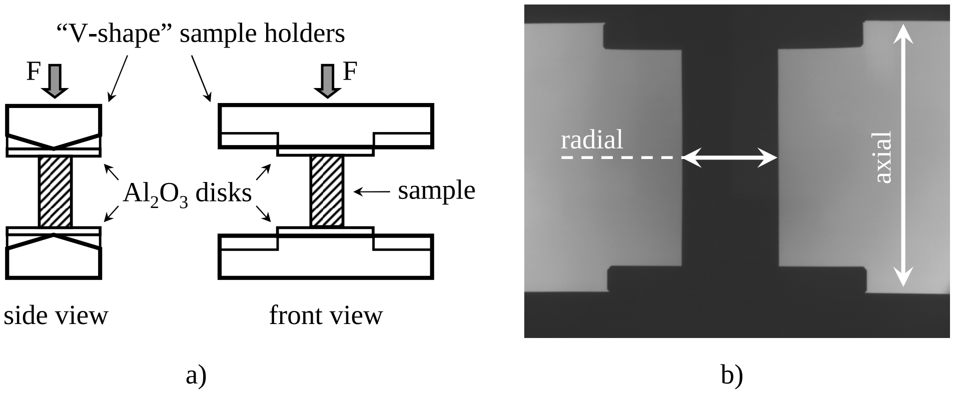

Figure 3.7.: Sample setup for the cycling unloading measurement: a) sketch with side and front views and b) projected image taken by the optical dilatometer

Al$_2$O$_3$ disc (2 mm high) is placed. They help to prevent from sticking between the sample and the sample holders, therefore contribute to a longer life-time of the sample holders. The measurement setup is represented in Figure 3.7 together with an exemplary projected image of the loading setup in TOMMI.

3.2.4.3. Bending setup

Adapted for tapes and long structures, the bending setup is designed for creep measurements under gravity (shape and dimensions given in Figure 3.8). Stabilized in each upper groove, 2 mm rods are placed to support the sample. The rods are covered by a thin BN-coating (drying phase prior to sintering at 80 °C for 2 h) for friction reduction.

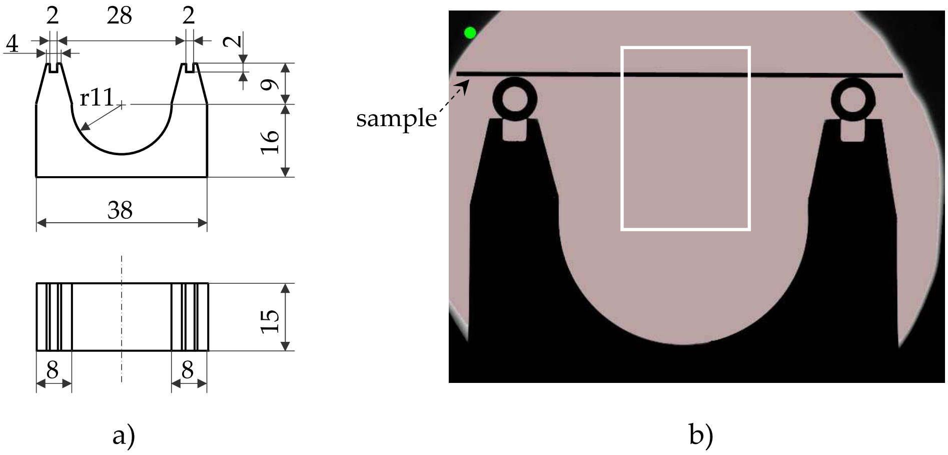

Figure 3.8.: Sample setup for bending tape measurement: a) sketch with side and front views and b) projected image taken by the optical dilatometer (the full-line rectangular area indicates the position of the curvature measuring window.)

Stripe samples (typically 45×5 mm^2) are positioned across the bending setup on the 2 rods. During sintering, the curvature of the stripes at the point of maximum deflection (in the middle part) is measured using the “curvature” window of the TOMMI software.

3.2.5. Experimental procedures and data treatment

3.2.5.1. Free sintering of tapes

This experimental procedure is used for the free sintering experiments of glass-ceramic tapes. The tapes are placed in the appropriated sample holders (see Section 3.2.4.1). Thermal treatments are carried out up to 890 °C with constant heating rates: 2 K/min, 5 K/min, 10 K/min, 15 K/min, 20 K/min. The holding time at 890 °C is 10 min and cooling is set to 5 K/min.

Shrinkage is measured by setting width windows on the middle part of the sample and images are recorded every 45 s (every 15 °C with 20 K/min).

Quenching of the glass-ceramic tapes during sintering is performed by taking the samples out of the furnace and placing them on a metallic plate. The cooling is effective within seconds. Several target temperatures are chosen in accordance to experimental results: 750 °C, 800 °C, 850 °C, 890 °C, 890 °C after 10 min holding time and 750 °C during cooling (experiments carried out with 20 K/min).

3.2.5.2. Cyclic unloading dilatometry

Compressive cyclic unloading dilatometry is used to characterize three different samples:

1. pressed compact cylinders of partially stabilized ZrO_2 undergo 5 load levels: 1 N, 50 N, 100 N, 150 N and 200 N (between 20 kPA and 4.5 MPa respectively with respect to the initial diameter),
2. stacks of Al_2O_3 (tape A) undergo 2 load levels 1 N and 150 N (between 20 kPa and 3 MPa with respect to the initial diameter),
3. stacks of ZrO_2 (tape B) undergo 2 load levels 1 N and 150 N (between 20 kPa and 3 MPa with respect to the initial diameter).

The smallest load (1 N, equivalent to 20 kPa) is small compared to the estimated sintering stress (in the MPa range[3]) and is not expected to generate creep. This small load serves the stabilization of the upper sample holder during the measurements for the sake of conserving the same experimental conditions for free sintering and loaded sintering measurements.

---

[3] A rough estimation of the sintering stress σ_s is calculated with $\sigma_s \approx 2\gamma_s/G$ (with the surface energy $\gamma_s \approx 1\ J/m^{-2}$ and the grain size $G \approx 0.2\ \mu m$) [48]

The largest part of the loading procedure remains the same for all three samples. A load of 10 N is first applied at the start of the measurement to ensure a careful adjustment of the contact {sample-to-sample holder}, therewith to prevent the green-body from breaking. During an isotherm at 850 °C, the maximum load is progressively applied within 30 min. When further unloading is required, the motor releases the load within seconds. The length of unloaded sequences are chosen as short as possible (to fulfil the requirements of the model), still long enough to obtain strain rates with sufficient accuracy. A good compromise is found with an unloading time of 7 min. Quick re-loadings within 2 min are done during the rest of the thermal treatments. Unloaded sequences are carried out every 50 °C till the maximum temperature, only with 2 K/min the unloaded sequences are carried out every 100 °C. Additional cycles are applied during the holding periods at the frequency of one per hour. A little change in the procedure is done for Al_2O_3 and ZrO_2 samples due to the higher temperature range: instead of complete release of the load during the unloaded sequences, loads of 15 N are applied.

The thermal treatment is very similar for all three samples, only the maximal temperature changes. First samples are heated up with 10 K/min up to an isotherm at 850 °C for 3 h. The isotherm serves the application of load as described in the previous paragraph. Further, the thermal treatment goes on according to conditions described in the Table 3.2.

Axial and radial strains are corrected for the thermal expansion of the materials as well as any eventual thermal aberration. A specific blank measurement is established for each material, each sample dimension and each setup considered. However one single temperature profile (with 1 K/min) is estimated sufficient for all heating rates. The blank test is carried out measuring the dimensions of one dense sample during a thermal treatment (see Figure 3.4). Finally the blank is subtracted from the online measurement.

Additional experiments are carried out with the ZrO_2 pressed compacts, aiming at the verification of the predictions done by the MSD. Load and temperature profiles are independently varied, the measuring conditions are summarized in Table 3.3.

Table 3.2.: Sintering conditions for loading dilatometry of ZrO_2 pressed compacts and Al_2O_3 and ZrO_2 stacks

Material system	**Heating ramp** [K/min]	**Target temperature** [°C]	**Holding time** [h]
ZrO_2 pressed compacts	0.25	1300	3
	0.5	1325	3
	1	1350	3
	2	1375	3
Al_2O_3 and ZrO_2 stacks	0.25	1460	5
	0.5	1470	5
	1	1480	5
	2	1490	5

Table 3.3.: Experimental conditions (thermal profile and load) for the verification of the MSD in free sintering and loaded conditions

Program	Step	Heating ramp [K/min]	Target temperature [°C]	Holding time [h]	Load [N]
1	1	1.5	1360	3	1
2	1	1.5	1200	0.5	1
	2	1	1360	3	1
3	1	1	1100	-	50
	2	1	1250	-	150
	3	1	1350	3	100
4	1	1	1100	-	50
	2	1	1250	-	1
	3	1	1350	3	100

Finally quenching measurements are carried out for microstructure investigations. In order to prevent the damaging of the loading setup by thermal shocks, the furnace is suddenly stopped at the required temperature (instead of taking the whole setup out). The thermocouple indicates a drop of temperature below 1000 °C with 5 to 7 min.

3.2.5.3. Warpage of asymmetric composites

Asymmetric composites (Al_2O_3/ZrO_2) are placed on an alumina plate and the curvature measured in the middle part of the bi-layer (see Figure 3.9). The co-sintering experiment is operated with 1 K/min up to 1450 °C for 5 h.

Two different mechanical models are used for the prediction of the warpage of the bi-layer: one based on the classical beam theory after Cai et al. [49] and another one based on the thin plate

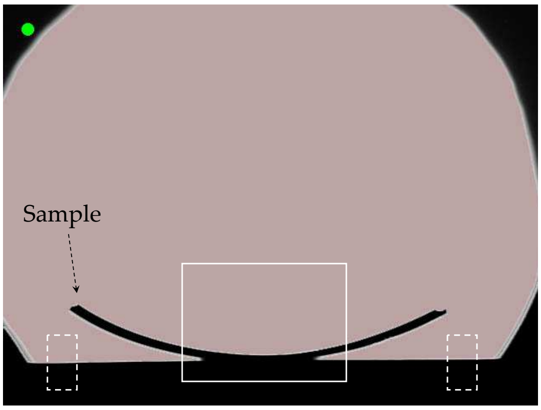

Figure 3.9.: Exemplary in-situ image of a warped bi-layer evaluated by TOMMI. The dashed-line rectangular areas are the background windows and the full-line rectangular area indicates the position of the curvature measuring window.

Kirchhoff theory after Kanters et al. [4]. Both authors used these equations in the past to describe the warpage of bi-layers.

Cai's formulation is based on the elastic beam theory using an infinite plate solution. It was applied to asymmetric bi-layers and linear viscous densifying materials. The curvature rate of the bi-layer is given by:

$$\dot{\kappa} = \frac{6hE(h+1)^2}{h^4E^2 + 2hE\left(2h^2 + 3h + 2\right) + 1} \cdot \frac{\Delta\dot{\varepsilon}}{1 - \nu_{v1}} \tag{3.2}$$

$$\text{with} \qquad h = \frac{h_1}{h_2} \qquad \text{and} \qquad E = \frac{\eta_{v1}(1 - \nu_{v2})}{\eta_{v2}(1 - \nu_{v1})}$$

$\dot{\kappa}$: curvature rate
$\Delta\dot{\varepsilon}$: sintering strain rate mismatch
η_v: uniaxial viscosity
ν_v: viscous Poisson ratio
h: ratio of the layer thickness of the layers 1 and 2
E: ratio of the viscous moduli of the layers 1 and 2

Kanters [4] used the thin plate theory description making the following assumptions:

- plate thickness is either uniform or varies slowly so that three dimensional stress effects are ignored,
- the plate is thin in the sense that the thickness is small compared to the characteristic length,
- there is no stresses in the z-direction (bi-axial stresses only),
- there is negligible shear between the layers.

Using the continuum mechanics approach, the radial stress in the composite can be defined for each point along the z-axis by:

$$\sigma_r(z) = \frac{\eta_v}{1 - \nu_v} \cdot \left(\dot{\varepsilon}_0 - \dot{\varepsilon}^f(z) - z\dot{\kappa}\right) \tag{3.3}$$

$\sigma_r(z)$: radial stress in the z-plane
$\dot{\kappa}$: curvature rate
$\dot{\varepsilon}_0$: lateral strain rate in the middle of the laminate where z=0
$\dot{\varepsilon}^f(z)$: lateral free sintering strain rate of the z-plane
η_v: uniaxial viscosity
ν_v: viscous Poisson ratio

For a multi-layer warping without additional external stresses, the integral of the stresses over the whole thickness compensate each other. Furthermore, if no external stresses are applied, then the moments also compensate each other. Therefore, it can be written:

$$\int \sigma_r(z)\, dz = 0 \tag{3.4}$$

$$\int \sigma_r(z)\, z\, dz = 0 \tag{3.5}$$

$$\tag{3.6}$$

Implementing Eq. 3.3 in the Eqs. 3.4 and 3.5, the system of equations can be solved and $\dot{\kappa}$ can be determined.

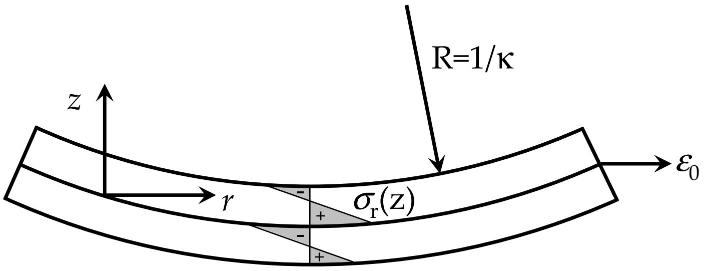

Figure 3.10.: Sketch of a warped bi-layer as illustration for Kanters' approach

3.2.5.4. Bending

The bending method is used in this work for the determination of the uniaxial viscosity of the glass-ceramic during sintering.

The bending of these stripes is only due to the effect of the gravity on the weight. The viscous behaviour of rectangular section beams was described by Lee et al. [50] doing the analogy to the elastic bending beam theory. The viscosity can be determined also for large deflections with:

$$\eta = \frac{3\rho g L^2}{2h^2 \dot{\kappa}_{max}} \tag{3.7}$$

η: uniaxial viscosity
ρ: absolute density in g/cm^3
g: gravity acceleration
L: span distance
h: thickness of the stripe
$\dot{\kappa}_{max}$ curvature rate at the maximum deflection

For the calculation, ρ and h are determined from the free sintering measurements in the same thermal conditions.

Measurements are carried out with constant heating rate between 2 K/min and 20 K/min. The samples (stripes with dimensions 45 mm×5 mm) are placed on the appropriated sample holder (see Section 3.2.4.3). Part of the stripes is hanging out on each side of the span in order to prevent the stripe from falling between the span while shrinking. The counterweight effect on the stripes is therefore more significant at the early stage of sintering, where the viscosity of the tape is still high. Later in the sintering, the stripe shrinks and the sample length responsible for counterweight becomes small.

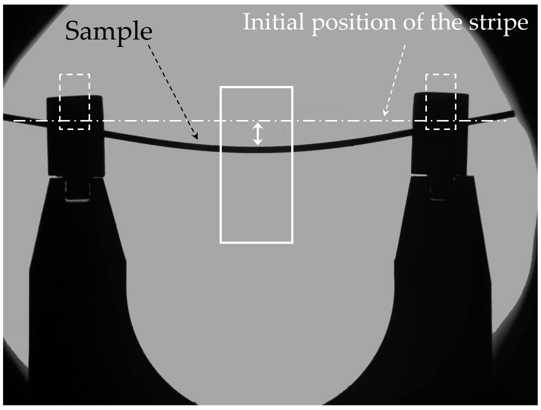

Figure 3.11.: In-situ image evaluated by TOMMI of a glass-ceramic tape bending under its own weight at 775 °C (2 K/min). The dashed-line rectangular areas are the background windows and the full-line rectangular area indicates the position of the curvature measuring window.

3.3. Additional characterization methods

3.3.1. X-ray diffraction

The powdered materials are characterized using a X-rays diffractometer (Bruker-AXS D8 Advance) in reflective mode with sample holders of about 2 mm in thickness and surface of roughly 15 mm in diameter. Samples are illuminated with a Cu-K_α beam (40 kV, 50 mA) and the scattered radiations are acquired in the standard Bragg-Brentano configuration. The measurement range is between 5° and 110° (2θ) with 0.02° steps and 6 seconds per step. Data evaluations are carried out with the program TOPAS 3 (Bruker-AXS) with the Rietveld standard method. The uncertainty of the phase concentration is estimated about 10% for amorphous phase and 5% for crystalline phase.

The sintered samples are characterized using a micro-diffractometer (Bruker-AXS D8 Discover) in reflective mode. Samples are stuck with an even surface facing out (measurement on end faces of the cylinders = measurement at the surface) and are illuminated with a Cu-K_α beam (40 kV, 50 mA) focused with a 100 µm capillary. The scattered diffractions are acquired on a flat detector frame in the standard Bragg-Brentano configuration, scanning the 2θ range between 12° and 103°. In total 23 frames are juxtaposed to generate complete diagrams, each frame is illuminated 900 s.

Data analysis is carried out with the program TOPAS 3 (Bruker-AXS) with the Rietveld standard method. The uncertainty of the phase concentration is estimated about 20% for amorphous phase and 10% for crystalline phase. High measurement uncertainties are due to the narrower investigated angle cutting part of the amorphous background.

The amorphous part is quantified using a structural model developed specifically for this material. The model is based on a crystalline quartz with doubled a-lattice parameter and a crystal size of 1 nm.

3.3.2. Microstructure investigation

Imaging green-bodies requires caution due to the weak particle bonding and the easy destruction of the microstructure with classic polishing procedures. Therefore, the green-bodies are prepared with a Cross Section Polisher device (CSP by Jeol). The principle is the cut of materials using an accelerated ion beam (in the present case with Ar^+, acceleration current 6 kV with 155 mA). This method is extremely time-consuming for ceramics but has the advantage to produce cross-sections without alteration of the microstructure.

For all other samples with advanced sintering stage, the polishing procedure remains the same: samples are ground down to 1 µm and further fine polished with an OPS-suspension (fine $\gamma-Al_2O_3$ suspension ≈0.3 µm). Further, dense samples are thermally etched at 1170 °C for 2 h and porous samples at 1050 °C for 1 h. Prior to Scanning Electron Microscope (SEM) investigations, samples are sputtered with Pt/Pd. Electronic images are taken with a Leo/Zeiss Supra 35VP microscope in the middle part of the samples. Only for the porous samples, the images are taken near the lateral surface (about 400 µm away from the surface) due to the grinding artefacts created in the middle part of the sample.

For grain size analysis, images are taken with the secondary electron (SE) detector with 25000× magnification, voltage 5 kV and working distance of 3 mm. The images are then transformed into a binary format using a relevant feature of the software AxioVision 4.6 (Zeiss) for the recognition of the grain-boundaries and pores. The linear intercept method is favoured to quantify possible grain anisotropy. The software ImageC (Imtronic, Germany) is used for this purpose. Cord-lengths are equidistant of 350 nm in both directions axial and radial (with respect to the loading direction). Caution is paid to the statistic, i.e. the average cord-length $\bar{l}$ is calculated with more than 500 grains (between 3 and 6 analyzed images). The average cord-length is annotated $\bar{l}_0$ for the axial direction and $\bar{l}_{90}$ for the radial direction. The anisotropy factor for the grains χ is defined with:

$$\chi = \frac{\bar{l}_0}{\bar{l}_{90}} \tag{3.8}$$

The grain size can be estimated by multiplying the average cord-length by the factor $\pi/2$ [51].

For the pore size analysis of porous structures, the SE detector is used with 20000× magnification, voltage 5 kV and working distance of 5 mm. The images are transformed in a binary format. Each pore is fitted with an ellipse of radii D_p and d_p. The orientation of one pore is defined by the angle made by the longest axis of the ellipse D_p with the vertical (see Figure 3.12): with $\theta = 0°$ the pore is oriented along the vertical axis (parallel to the load) and with $\theta = 90°$ the pore is oriented along the horizontal axis (radial to the load). An experimental limit is fixed to distinguish elliptic and circular pores: when $1 < D_p/d_p < 1.15$, then the pore is considered as circular having therefore no preferential orientation. About 500 pores are analyzed in total.

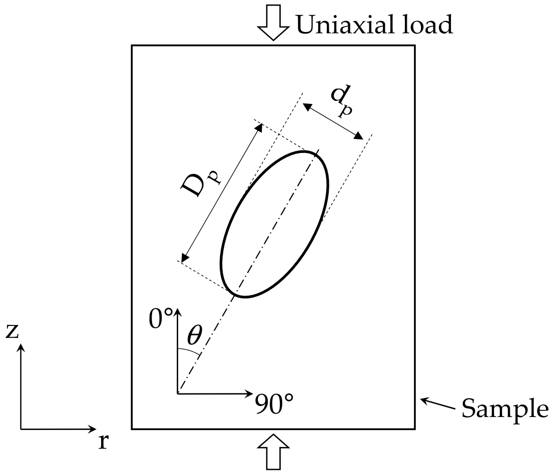

Figure 3.12.: Sketch of an elliptic pore with radii D_p and d_p oriented by θ to the vertical

3.3.3. Density

The density was measured according to the Archimedes method with water infiltration.

4. Material model construction for one specific material: zirconia pressed compacts

4.1. Sintering characterization and input data

4.1.1. Free sintering kinetics

Axial and radial shrinkage strains are measured during free sintering experiments and are plotted versus temperature in Figure 4.1 for four different heating rates between 0.25 K/min and 2 K/min. For each thermal treatment, the average deviation between the axial and radial strain curves is very low and the maximum deviation is below 3% (see Table 4.1): it indicates the isotropic shrinkage of these powder compacts, thus the microstructure homogeneity of the green bodies. Increasing the heating rate, the shrinkage curves are shifted toward higher temperatures, meaning that the same strain is reached at higher temperature with a quicker heating rate. It results from a typical thermal kinetic effect: in a same temperature range, the material has more time to response to the driving forces with a slow heating rate compared to larger heating rates. The observed temperature shift of the strain curves is the accumulation of the previously cited effect. Further quantitative description of the shrinkage curves are presented in the Table 4.2 together with the final density values either calculated from the shrinkage curves applying Eq. 3.1 or experimentally measured with the Archimedes method.

The agreement between the density calculated with two different methods (see Table 4.2) is an indirect validation for the measurement precision of the optical dilatometer. Nevertheless, both methods indicate a slight variation in absolute final density (±1% around the average) with the sintering profile (both heating rate and maximal temperature changed). Being clear that this variation is small, phase analyses are further undertaken to identify any relative variation in the crystallographic distribution from one to another sample (see the phase diagram for ZrO_2-Y_2O_3 in Appendix B). The measurements are carried out at room temperature, but it is assumed that the phase distributions at room temperature are relevant from the state at high temperatures (rapid

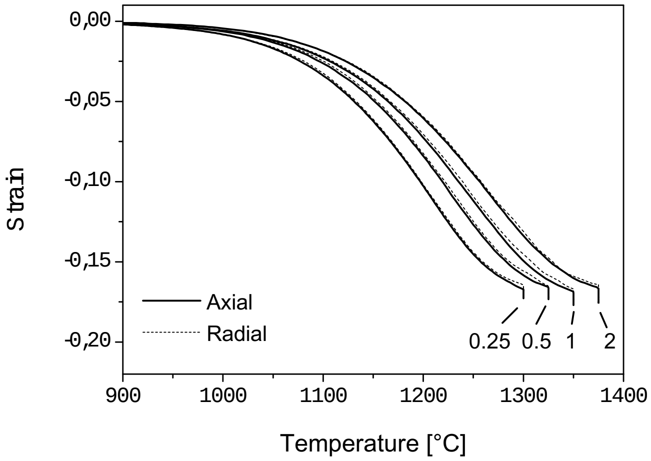

Figure 4.1.: Free sintering shrinkage strains in axial and radial directions of ZrO_2 pressed samples measured for four different heating rates: 0.25 K/min, 0.5 K/min, 1 K/min and 2 K/min

Table 4.1.: Experimental deviations between the radial and axial strains of the free sintering runs displayed in Figure 4.1. Only the data points above the onset of shrinkage (see Table 4.2) are considered.

Heating rate [K/min]	Average deviation	Maximum deviation	Relative max. deviation
0.25	0.001	0.003 at 1300 °C	1.7%
0.5	0.001	0.003 at 1300 °C	1.9%
1	0.002	0.004 at 1300 °C	2.7%
2	0.001	0.003 at 1300 °C	2.3%

Table 4.2.: Quantitative description of free sintering shrinkage curves: temperatures at the shrinkage onset* and at half of the maximal strain as well as final densities calculated from shrinkage strains and measured according to the Archimedes method

Heating rate [K/min]	Shrinkage onset [°C]	T [°C] for $\varepsilon = 0.5\varepsilon_{max}$	Density [g/cm^3] Shrinkage	Density [g/cm^3] Archimedes
0.25	990	1182	5.97 ±0.06	5.98 ±0.01
0.5	1010	1204	6.01 ±0.06	6.02 ±0.01
1	1020	1220	6.07 ±0.06	6.07 ±0.01
2	1030	1238	6.04 ±0.06	6.04 ±0.01

* The onset temperature for shrinkage is defined by the intersection of the line $\varepsilon = 0$ and the tangent of the strain curve at $\varepsilon = -0.02$

cooling). Additionally to the sintered samples, the raw powder and a crushed pre-sintered green-body (at 850 °C for 1 h) are also analyzed. All results are given in Table 4.3. The initial raw powder contains 36 wt% of monoclinic (M) phase and 64 wt% of tetragonal (T) phase. No cubic (F) phase is detected. After pre-sintering, a large part of the powder is stabilized in tetragonal phase (9 wt% of monoclinic and 91 wt% of tetragonal) and no cubic phase is formed. During pre-sintering at 850 °C the eutectoid transition M to T is exceeded (transition at 550 °C), thus a large part of the M phase transforms in tetragonal crystal structure. The reverse transformation T to M by cooling is hindered by the pre-sintering of the grains preventing the volume change associated with the transformation T to M [52]. The presence of 9 wt% of M phase in the pre-sintered structure can be explained by (i) the non-complete transformation during the thermal treatment or (ii) the reverse transformation T to M during crushing (typical effect of the toughening of zirconia) [52]. Further characterization of the pre-sintering bodies without crushing could help to valid one or the other hypothesis. After sintering, the monoclinic phase disappears at the benefit of 75 wt% of tetragonal and 25 wt% of cubic phase independently of the thermal treatment used (small variations within the measurement error of 5% can be noticed). In conclusion, all thermal treatments lead to the same repartition of crystal structure T and F. Thereby, the slight variation of final density cannot be caused by differential crystalline phase distribution.

Table 4.3.: Crystalline phase distribution in ZrO_2 after thermal treatment (given in wt%)

Thermal treatment	Monoclinic	Tetragonal	Cubic
none	36.1	63.9	-
1 h at 850°C	9.4	90.6	-
3 h at 1300°C (0.25 K/min)	-	76.4	23.6
3 h at 1325°C (0.5 K/min)	-	76.7	23.3
3 h at 1350°C (1 K/min)	-	73.4	26.6
3 h at 1375°C (2 K/min)	-	73.9	26.1

4.1.2. Sintering kinetics with load

Sintering strain under uniaxial compressive load is plotted for several loads between 1 N and 200 N and for one exemplary heating rate (0.5 K/min) in Figure 4.2. With the application of uniaxial compression during sintering, it becomes necessary to distinguish dimensional change in the axial z-direction (in load direction) and in the radial r-direction (in the normal plane to the load): creep is summed up to the sintering shrinkage resulting in (1) larger axial strains and (2) smaller radial strains. With increasing the load, the latter effect is greater. During the holding time at 1350 °C, the samples exhibit further shrinkage with 1 N and 50 N, no significant shrinkage with 100 N and a reduction of the strain with 150 N and 200 N. This result points out the competition between sintering and creep: as sintering slows down, the sintering stress diminishes and becomes smaller than the stresses which are generated by external loads above 100 N in the radial direction. The creep behaviour stress-strain rate of this material is linear over the whole range of temperature in

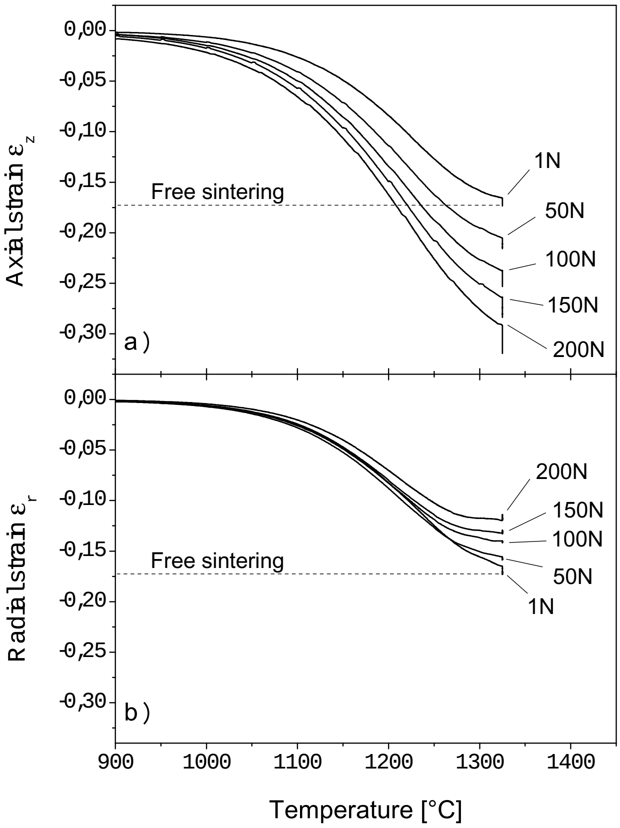

Figure 4.2.: a) axial and b) radial strains of ZrO_2 pressed samples during sintering under uniaxial load between 1 N and 200 N and for one thermal treatment: 0.5 K/min up to 1325 °C for 3 h. Some steps on the curves corresponding to the unloaded periods can be noticed (more pronounced on the axial curves) but do not disturb much the overall strain curves.

the studied load range (see Figure 4.3). Finally, the influence of external stresses on the densification curve is shown to be limited: either 50 N or 200 N enhances equally the densification by 5% of relative density compared with free sintering. This effect is further discussed in Chapter 7.

The strain rates in loaded and unloaded sequences of the same measurement (150 N, 1 K/min) are compared in Figure 4.5. Strain rates in unloaded sequences (1 N) are smaller than strain rates in loaded sequences (150 N) in the axial direction (Figure 4.5.a) and vice-versa in the radial direction (Figure 4.5.b). The release of load (during unloaded sequences) suppresses the contribution of creep, thus only sintering shrinkage contributes to strain. This explains the slower axial strain rates and the faster radial strain rates in the unloaded sequences.

The strain rates of unloaded segments are further compared with the free sintering rates (Figure 4.6). Despite the equal load (1 N in both free and unloaded cases) and the equal temperatures (the same matter transport are activated) the unloaded strain rate in the axial direction is slower than the free sintering rate (higher the load, lower the strain rate). During the loaded period, large

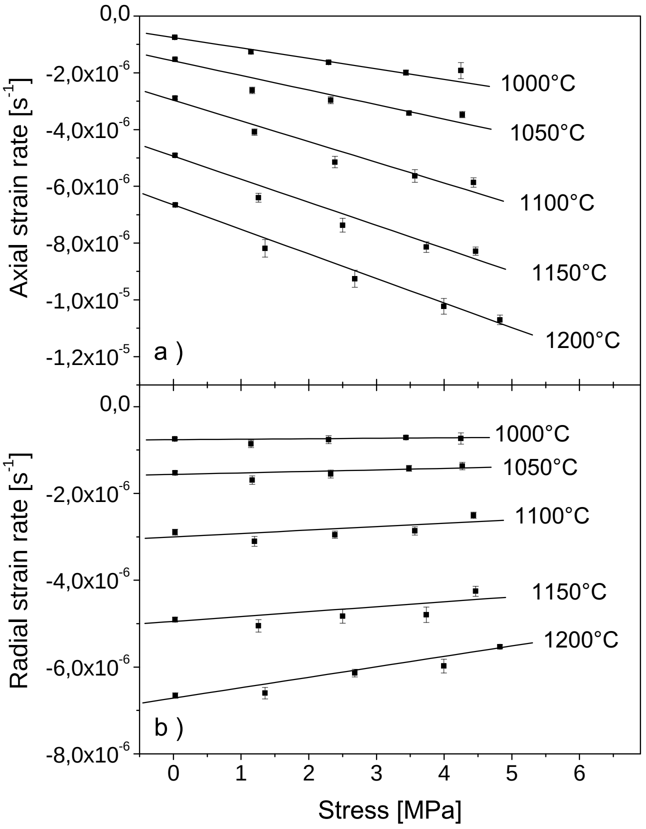

Figure 4.3.: Creep behaviour in sintering ZrO_2 samples illustrated by the relation stress-strain rates in a) axial and b) radial directions at several temperatures and for one thermal treatment: 0.5 K/min up to 1325°C for 3 h

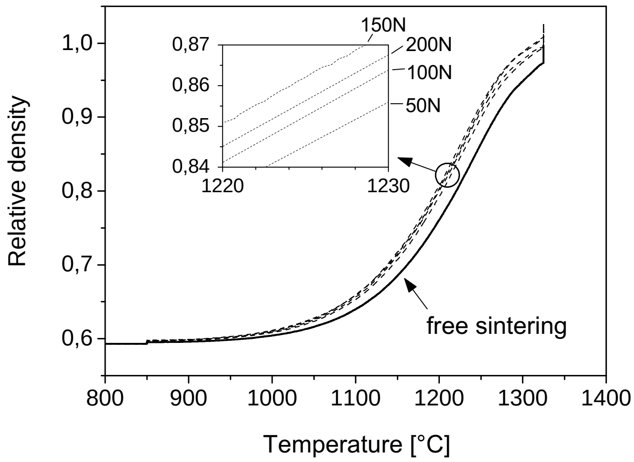

Figure 4.4.: Influence of the load 50 N, 100 N, 150 N and 200 N on the densification of ZrO_2 powder compacts with one thermal treatment: 0.5 K/min up to 1325°C for 3 h

part of the sintering potential is consumed (enlarged necks, larger curvatures, narrowed particle centres), therefore when the creep contribution is cut off, the strain rate due to sintering is smaller compared to that of a fully free sintered sample. In the radial direction, no clear trend can be identified.

Since the load and the temperatures are equal (Figure 4.6), the difference in strain rate can be only attributed to different microstructure topologies comparing free with (cyclic) loaded samples. This conclusion was already drawn by Zuo et al. [20] with Al_2O_3 sintering bodies under uniaxial load, by stating the formation of microstructure anisotropy under uniaxial load and introducing the notion of loading memory.

The loading memory is also remarkable when the load is increased: the plot in Figure 4.7 displays the axial strain rate of two measurements: one measurement with cyclic unloading 150 N and the other one a load step from 50 N to 150 N at 1100 °C (1 K/min for both). Below 1100 °C, both measurements undergo two different loads, thus the strain rate of the measurement with 50 N is lower (about -20%) than the one with 150 N (see also the equivalent strains in Figure 4.2). As

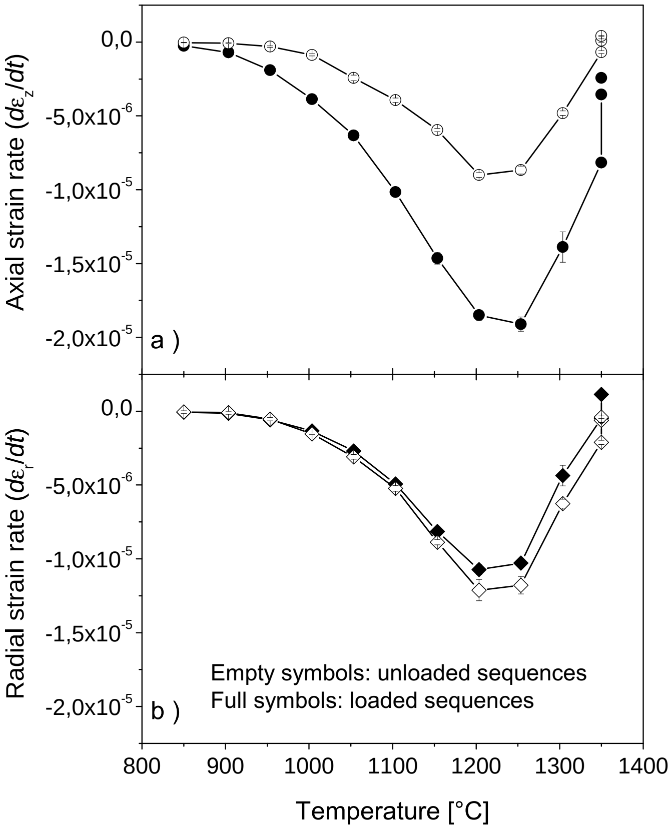

Figure 4.5.: Comparison of the sintering strain rates in loaded and unloaded sequences of a cyclic loading measurement (150 N and 1 K/min) in a) axial and b) radial directions

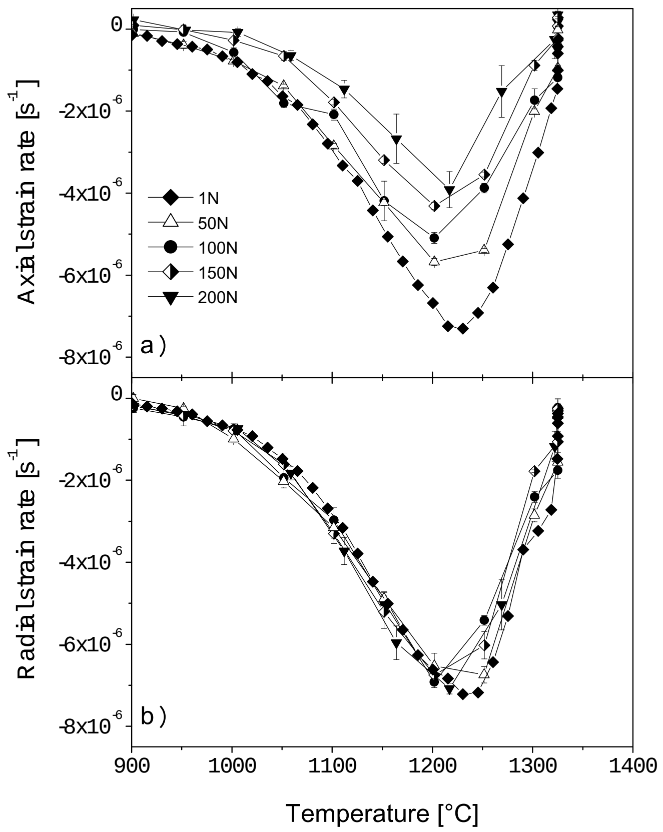

Figure 4.6.: Free sintering strain rates and strain rates during the unloaded sequences of cyclic unloading dilatometry in a) axial and b) radial directions for 50 N, 100 N, 150 N and 200 N and 1 K/min

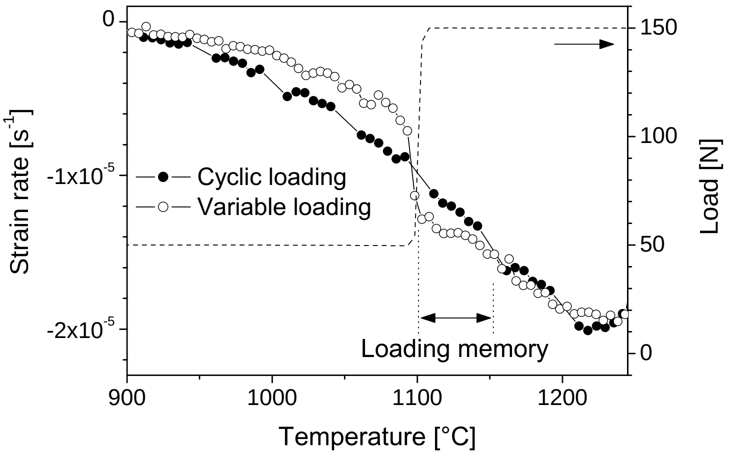

Figure 4.7.: Axial strain rates of one cyclic unloading measurement (150 N) and one other measurement under variable load 50 N then 150 N. The heating rate is the same for both measurements (1 K/min).

the load is increased from 50 N to 150 N, the axial strain rate becomes significantly larger (about +30%) than the cyclic loading measurement with 150 N despite the same load and temperature conditions. Since less creep takes place during the sequence with 50 N, more creep potential is available when 150 N is applied. It takes about 50 °C (in this case 50 min) before both strain rate curves reach each other.

4.2. Construction of the MSD with the input data

The cross-section of the MSD for F=1 N is presented in Figure 4.8 with a couple of iso-strain lines between $\varepsilon = 0.03$ and $\varepsilon = 0.17$ (see the detailed description of the construction in Chapter 2). The anticlockwise rotation of the iso-strain lines with shrinkage (see Figure 4.8) is also expressed by the steady decrease of their slope. According to Eq. 2.4, the slope is directly proportional to the apparent activation energy for sintering E_a (see E_a versus strain in Figure 4.9): values between 750 kJ/mol and 600 kJ/mol are found.

Other cross-sections of the MSD with uniaxial compressive loads between 50 N and 200 N are plotted in Figure 4.10. Due to anisotropic strains, two plots are necessary for axial and radial directions respectively. The relative position of the iso-strain lines from one to another cross-section are presented in the 2D-projection of the MSD in Figure 4.11. In both axial and radial directions, a parallel shift of the iso-strain lines is generated by the load, either to lower temperatures in the axial direction or to higher temperatures in the radial direction. The parallel shift is an experimental confirmation that densification and creep are supported by thermally activated mechanisms with the same activation energy.

Each Arrhenius plot in Figure 4.10 displays the well defined sintering kinetics for constant load (1 N, 50 N, 100 N, 150 N or 200 N). The change in sintering kinetics with changing load is assessed by interpolating between one cross-section to the next cross-section. The mathematical interpolation can be visualized making a cross-section in the MSD for one specific strain rate, for example $ln(-T \cdot \dot{\varepsilon}) = -4.5$ is given in Figure 4.12. The interpolation between the sintering kinetics of defined loads in the axial direction can be done using exponential fits. In the radial direction, the scattering is a bit larger, therefore linear fits should give sufficient accuracy.

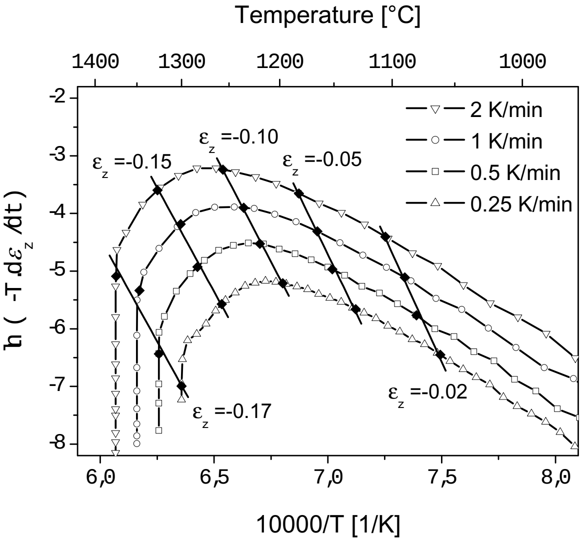

Figure 4.8.: Cross-section of the MSD for 1 N measurements in the axial direction (note that the diagram is identical for radial directions) with $\dot{\varepsilon}$ in seconds and T in K

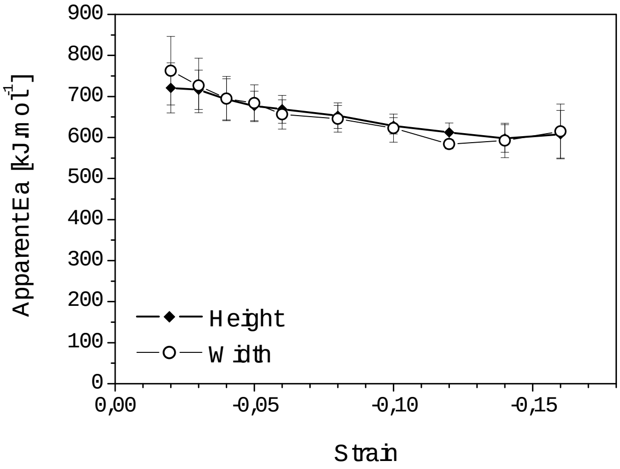

Figure 4.9.: Apparent activation energy for free sintering (1 N) as function of densification (expressed by the linear strain)

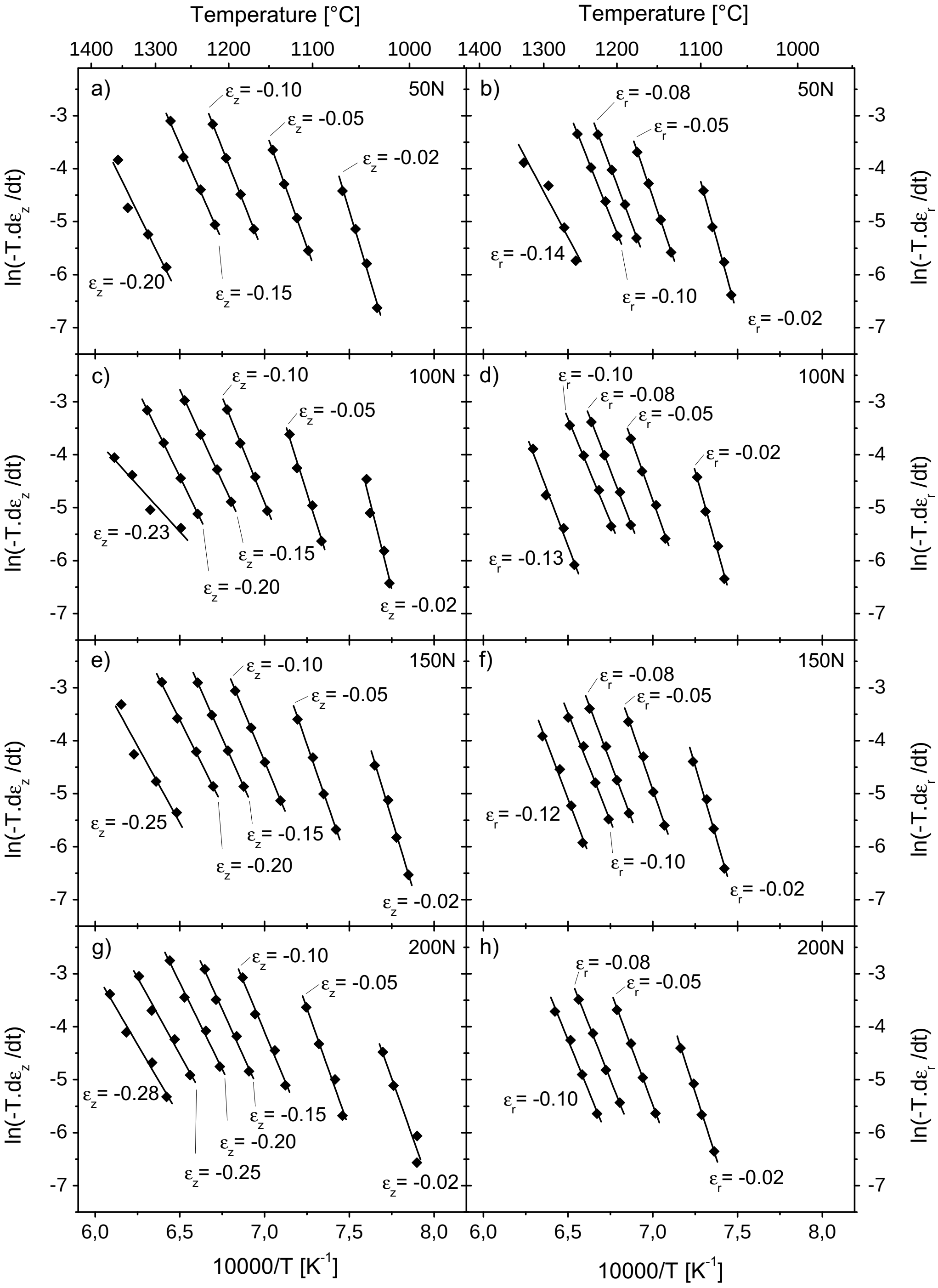

Figure 4.10.: Cross-sections of the MSD for axial strains on the left and radial strains on the right at defined loads: a) and b) for 50 N, c) and d) for 100 N, e) and f) for 150 N and g) and h) for 200 N ($\dot{\varepsilon}$ is in seconds and T in K)

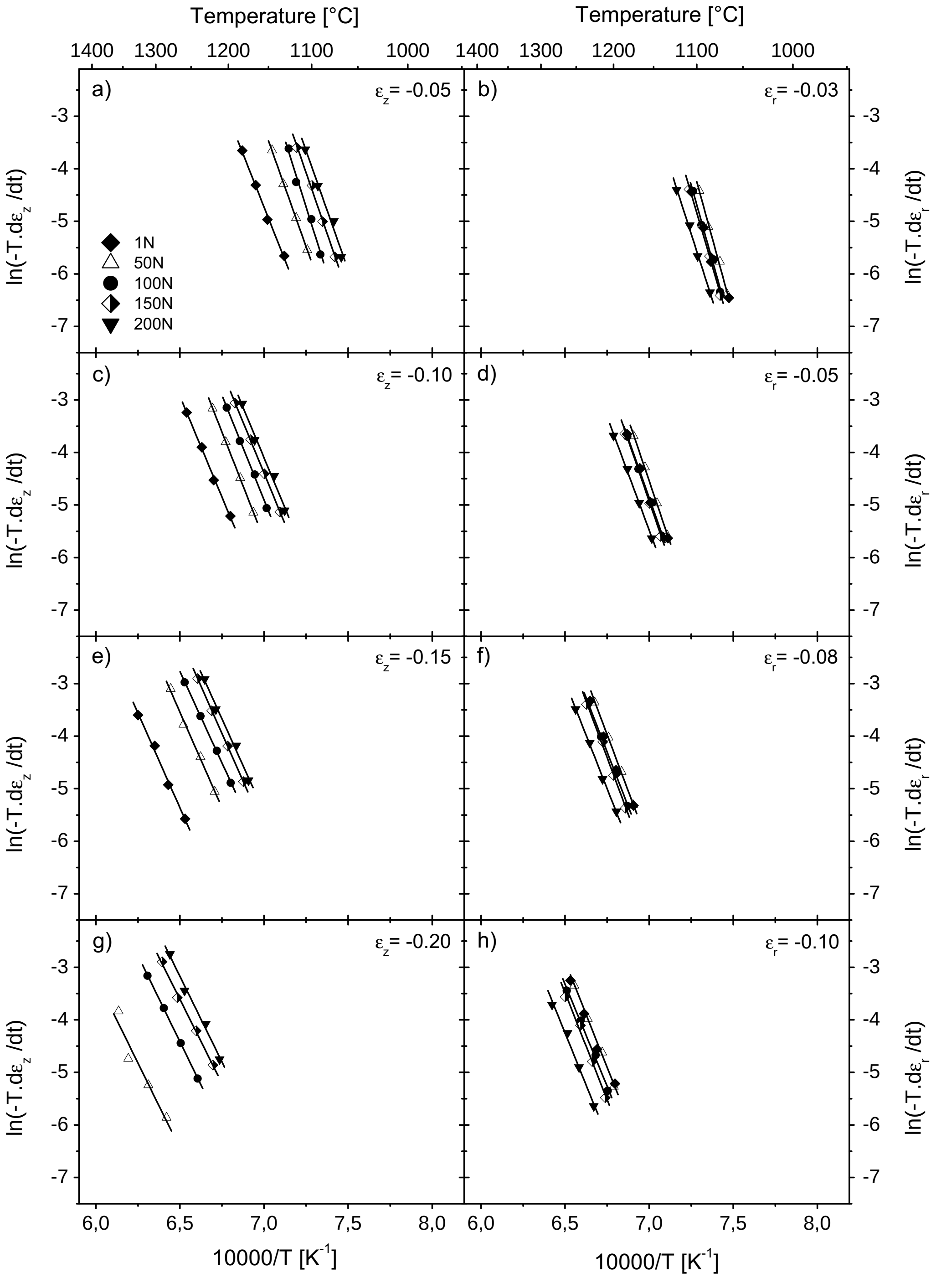

Figure 4.11.: 2D-projection of the MSD showing the iso-strain lines belonging to 5 different planes of the MSD with 50 N, 100 N, 150 N and 200 N for strains between 3% and 20%

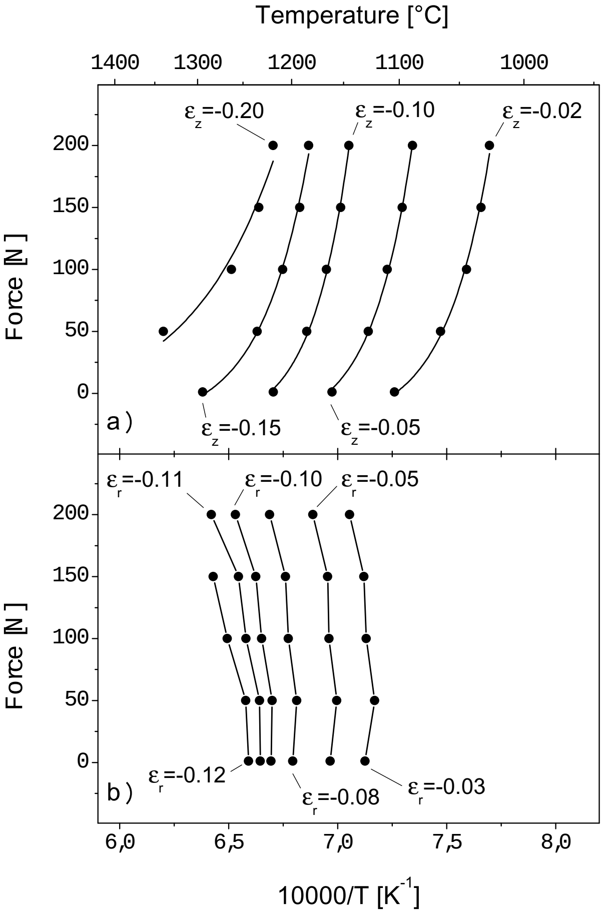

Figure 4.12.: Horizontal cross-section of the MSD at $ln(-T \cdot \dot{\varepsilon}) = -4.5$ in a) axial and b) radial directions

4.3. Viscous behaviour during sintering

4.3.1. Experimental determination of the viscous moduli

The strain rate difference in axial and radial directions occurring with a sudden change of load is utilized for the calculation of the viscous moduli (see Section 2.2). The experimental results for both viscous moduli are given in Figure 4.13 using the information contained in one sintering run (with 200 N and 1 K/min). The uniaxial viscosity is in the range 400 to 10000 GPa.s and shows a minimum at 1250 °C. This minimum corresponds to 90% of relative density, as the final sintering stage starts. The viscous Poisson ratio ν_v apparently increases in the range 0 to 0.5. The experimental difficulty to assess the latter parameter is expressed here by the large error bars about ±20% at best. Below 1000 °C experimental data scattering becomes even larger due to the small viscous behaviour at these temperatures. At the highest temperatures, ν_v ends by about 0.3.

The decrease and later increase of η_v (see Figure 4.13) can be attributed to the simultaneous effects of temperature and densification. On the one hand, the diffusion between two regions of different chemical potential (between the zones undergoing compression and these under tension) becomes easier with increasing temperature. Subsequently creep is larger and η_v apparently decreases. On the other hand, as densification takes place, the compressibility of the structure becomes less due to smaller, more isolated and rarer pores. Both effects result in the increase of η_v. The increase of ν_v within the range 0 to 0.5 is in adequacy to the expectations [45]. However, the large scattering of the data at low temperatures does not permit to make clear conclusions on the starting value of ν_v.

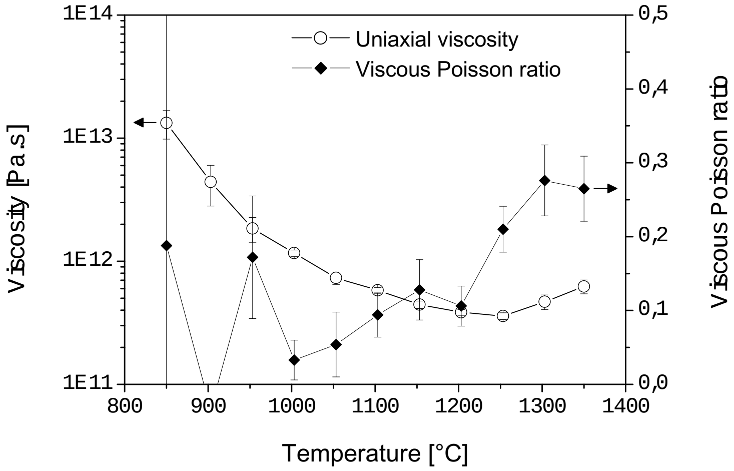

Figure 4.13.: Uniaxial viscosity and Poisson ratio for ZrO_2 pressed powder determined with one sintering run (200 N and 1 K/min)

4.3.2. Influence of the load on the viscous moduli

The same calculations are repeated for the cyclic unloading measurements with 100 N, 150 N and 200 N. Using the equivalence equations between the viscous moduli (Eqs. 2.5 and 2.6), the bulk K_v and shear viscosities G_v are given in Figure 4.14 for one single thermal profile (0.5 K/min up to 1325 °C). Obviously K_v and G_v are insensitive to the load. This result can be expected since (i) the viscous moduli are material characteristics, (ii) the creep behaviour is shown to be linear (see Figure 4.3) and (iii) the density remains unchanged with the load (Figure 4.4). Consequently, averaging K_v and G_v is found to be an acceptable method to reduce the data scattering.

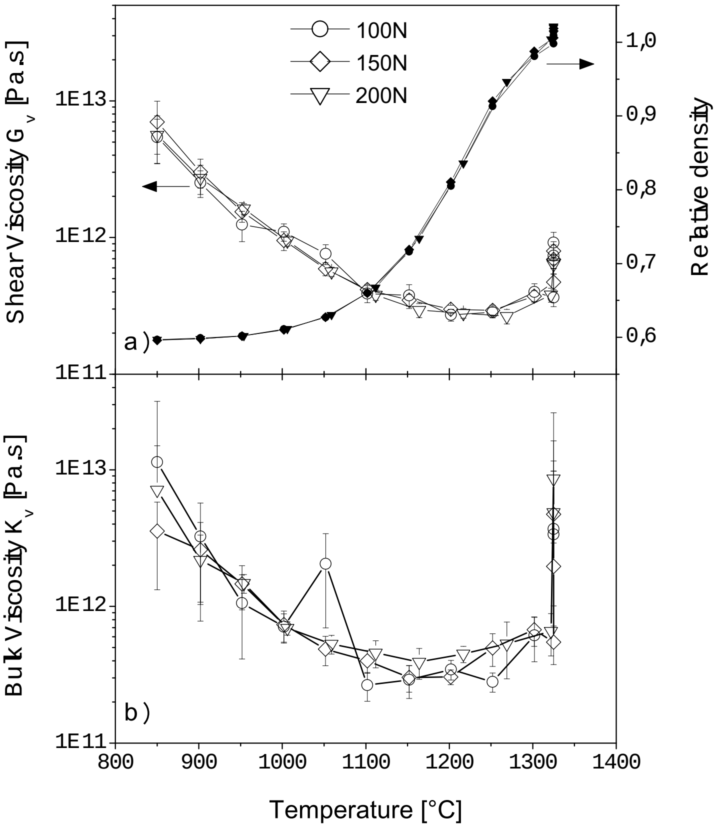

Figure 4.14.: a) Shear and b) bulk viscosities for ZrO_2 pressed powder compacts determined with three measurements of different load 100 N, 150 N and 200 N for one thermal profile 0.5 K/min up to 1325°C. The densification is also given as function of temperature in a).

4.3.3. Influence of the heating rate on the viscous moduli

The uniaxial viscosity η_v is reversely calculated using Eqs. 2.5 and 2.6 and the averaged K_v and G_v values obtained from several cyclic unloading measurements (100 N, 150 N and 200 N). The uniaxial viscosity η_v is displayed in Figure 4.15 versus temperature for 4 heating rates. For the

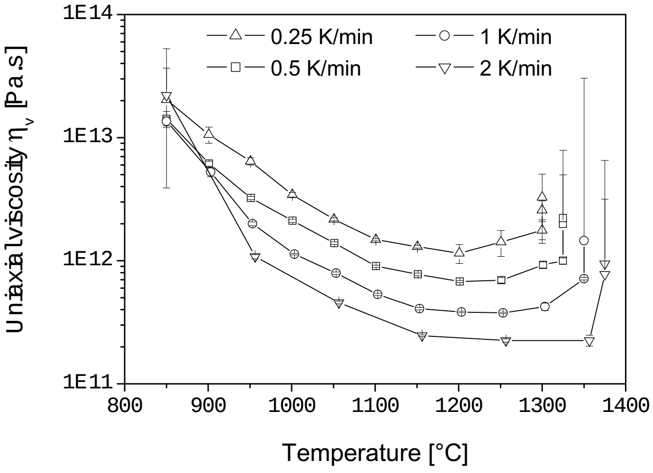

Figure 4.15.: Influence of the heating rate on the uniaxial viscosity η_v calculated from averaged K_v and G_v values presented in Figure 4.14

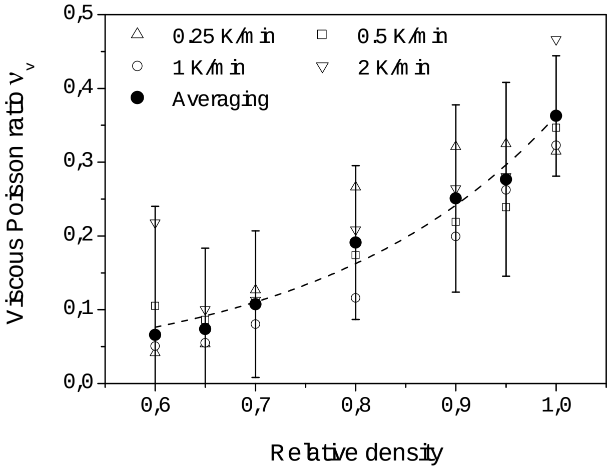

Figure 4.16.: Viscous Poisson ratio ν_v calculated from averaged K_v and G_v values presented in Figure 4.14 and for 4 heating rates (0.25 K/min till 2 K/min). The averaged Poisson ratio (averaging of 4 heating rates) are fitted by an exponential function.

same temperature, η_v increases significantly with slower heating rates (about one order of magnitude). This is attributed to the difference in density of the samples: at one same temperature, different densities are reached with different heating rates (equivalent effect to the one presented in Figure 4.1). This is an experimental demonstration of the dependence of η_v on both temperature and density.

The viscous Poisson ratio ν_v is per definition related to the geometrical ratio of the strain rates. Consequently, the main dependence of ν_v is expected to be on density and not on temperature. The viscous Poisson ratio ν_v is given in Figure 4.16 for 4 different heating rates. The viscous Poisson ratio being more dependent on density than on temperature, the data averaging of the 4 heating rates is done. Due to the large scattering of the data points, the error bars of these averaged values are necessarily high since they are calculated considering the uncertainty of each point. Finally, an exponential fit of the data points is proposed with the form $\nu_v = A_0 + A_1 \exp(\bar{\rho}/A_2)$ with $A_0 = 0.01153$, $A_1 = 0.00513$ and $A_2 = 0.23659$. The agreement of the fit with the experimental results is acceptable (average deviation: 0.013; maximal deviation: 18% by 80% of relative density). The fit predicts $\nu_v = 0.07$ for the green-bodies ($\bar{\rho} = 0.59$) and $\nu_v = 0.36$ for the maximum density.

Combining Eqs. 2.5, 2.6 and 2.7, G_v and K_v are reformulated in:

$$G_v = \frac{\sigma_z}{2\,(\Delta\dot{\varepsilon}_z - \Delta\dot{\varepsilon}_r)} \tag{4.1}$$

and

$$K_v = \frac{\sigma_z}{3\,(\Delta\dot{\varepsilon}_z + 2\Delta\dot{\varepsilon}_r)} \tag{4.2}$$

The strain rates being thermally activated and the viscous moduli G_v and K_v being directly dependent upon $\Delta\dot{\varepsilon}_z$ and $\Delta\dot{\varepsilon}_r$, both moduli G_v and K_v can be reasonably plotted in an Arrhenius form. They are displayed in Figure 4.17 for several heating rates between 0.25 K/min and 2 K/min (note that the fitted ν_v values are taken for the reverse calculation of G_v and K_v). The representation of iso-strain lines (here axial iso-strain lines are exemplarily shown) recalls the construction of the MSD. This solution is proposed as an elegant manner to combine the dependence of G_v and K_v on temperature and density.

4.3.4. Influence of the holding time on the viscous moduli

In Figure 4.15 the uniaxial viscosity increases further although the maximum temperature is reached. In order to appreciate the evolution of η_v in dense bodies, one single cyclic unloading measurement is carried out with a longer holding time at 1350 °C. Both viscous moduli η_v and ν_v are plotted in Figure 4.18 versus the time. The first comment goes to the viscous Poisson ratio whose scattering was already described in Section 4.3.1. However, in contrast to the results in Section 4.3.2, ν_v reaches values closer to 0.5. Secondly, η_v is multiplied by a factor of 4 during the first 5 hours of the holding time. Beyond this time, the uniaxial viscosity does not increase significantly. Since the sample is already dense, the increase of η_v can only related to the grain growth. This result will be further discussed in Chapter 7.

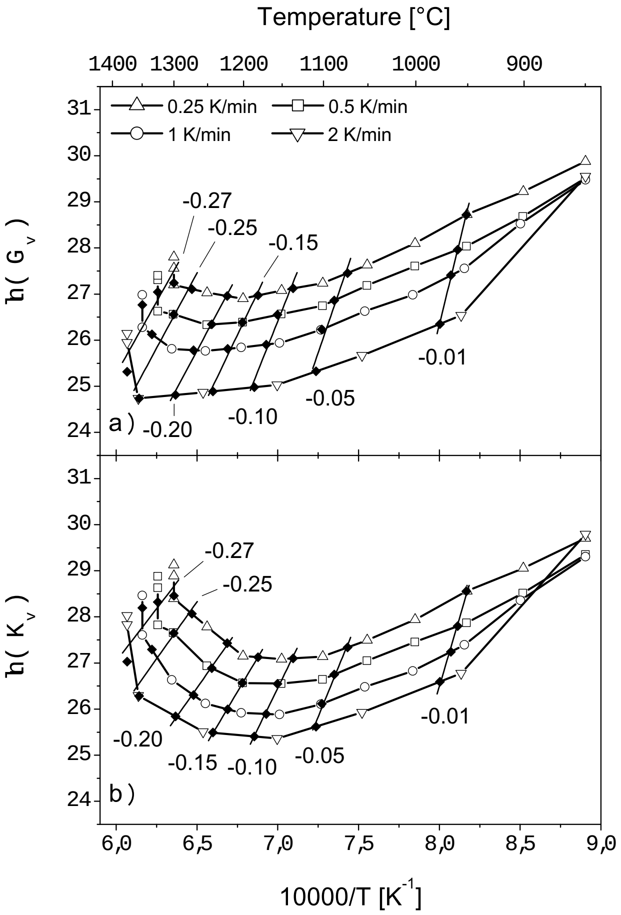

Figure 4.17.: Arrhenius representation of a) the shear G_v and b) the bulk K_v viscosities for ZrO_2 pressed powder for 4 heating rates (0.25 K/min till 2 K/min). Iso-strain lines (ε_z) for 150 N are drawn.

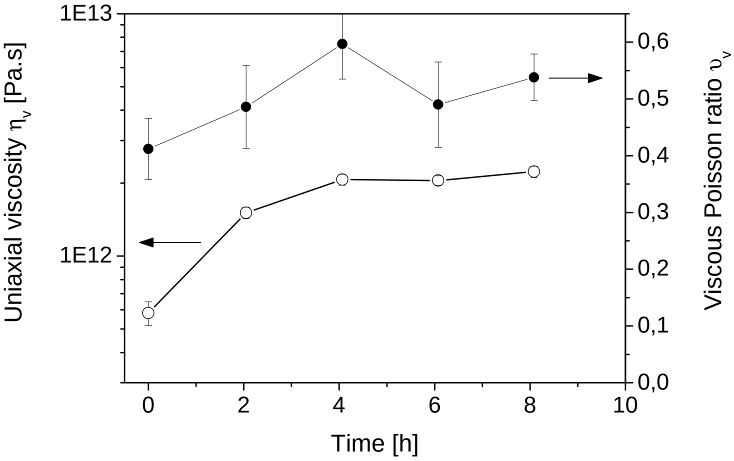

Figure 4.18.: Evolution of the viscous moduli η_v and ν_v during holding time at 1350 °C (heating rate 1 K/min, load 150 N)

4.4. Microstructure investigations

4.4.1. Measurement of the particle size in the green-body

The particle size before sintering is assessed by image analysis of cross-sections of a green-body (see Figure 3.1). The average cord-length is (135±4) nm.

4.4.2. Influence of the thermal treatment on the microstructure of free sintered samples

The influence of the thermal treatment is investigated with 4 free sintered samples (free sintering runs displayed in Figure 4.1). An image of the microstructure of each sample is given in Figure 4.19 and the average cord-length is presented in Figure 4.20.

The anisotropy factor χ is close to 1 (see Figure 4.20) and are not significantly different from one or the other sample. Between the two extreme sintering temperatures (1300 °C at 0.25 K/min and 1375 °C at 2 K/min), the average cord-length increases from (175±4) nm to (225±7) nm. The increase of the average cord-length is respectively about 30% and 66% in comparison with the initial particle size. The grain growth of this material can be considered to be small.

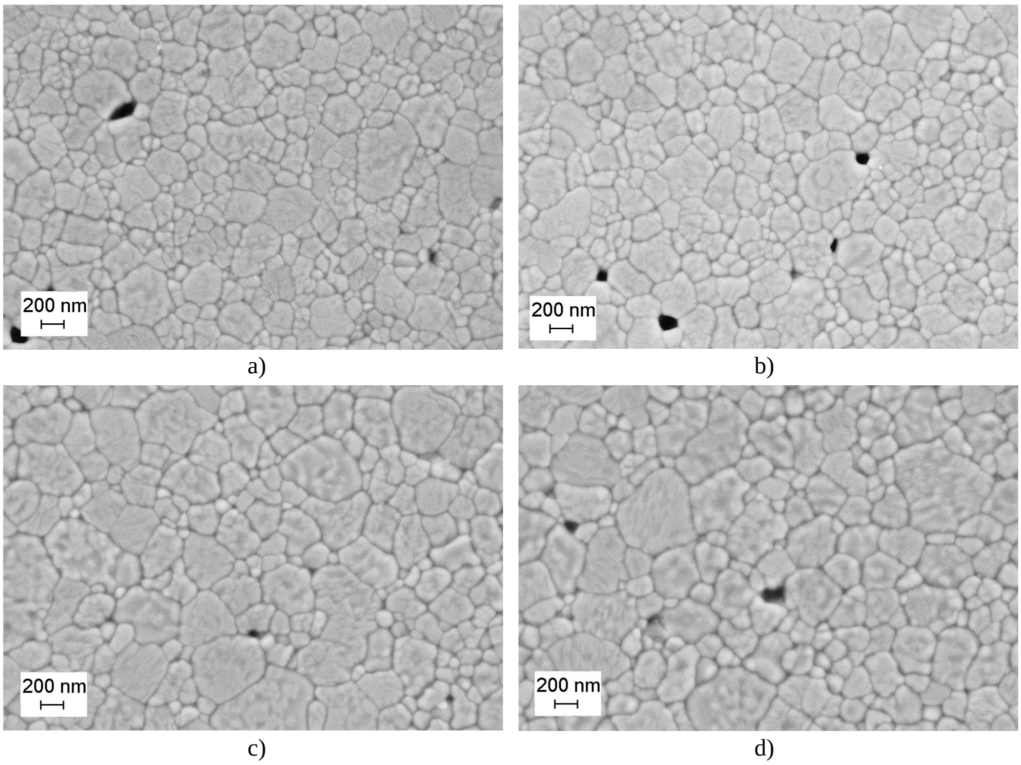

a) b) c) d)

Figure 4.19.: SEM images (SE detector, current 5 kV, WD 3 mm) of the microstructure of ZrO_2 dense samples (free sintering) a) with 0.25 K/min up to 1300 °C, b) with 0.5 K/min up to 1325 °C, c) with 1 K/min up to 1350 °C, d) with 2 K/min up to 1375 °C

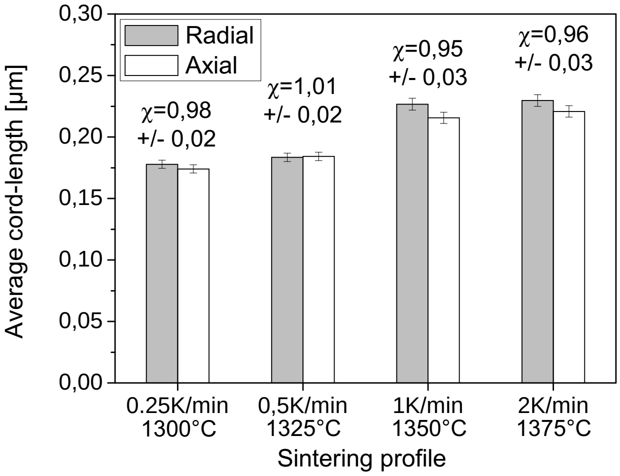

Figure 4.20.: Influence of the sintering profile on the average cord-length in the axial and the radial directions (χ is the anisotropy factor)

4.4.3. Microstructure evolution during loaded sintering

The influence of the uniaxial load on the microstructure is investigated with dense samples sintered with several holding times (1 K/min up to 1350 °C, 150 N load). The average cord-lengths in axial direction ($\bar{l}_0$) and radial ($\bar{l}_{90}$) directions are given in Figure 4.21.

At the beginning of the holding $t = 0$ the anisotropy factor $\chi = 0.95 \pm 0.04$. There is not significant change with longer holding time. It can be thus concluded that no grain anisotropy occurs during the holding time at 1350 °C and with a load of 150 N. The anisotropy factor does not change significantly with the free sintering experiments either (see Section 4.4.2). The average cord-length increases by 53% between t=0 and t=24 h.

The influence of the load (150 N) is further investigated with the analysis of the pore orientation in porous structures with a relative density of 85%[1] (see procedure in Section 3.3.2). An exemplary binary image of the porous samples is shown in Figure 4.22. About 560 pores are analyzed and 7% of these are circular (the ratio of the ellipse radii are between 1 and 1.25). The orientation of the remaining pores (more than 500 pores) is plotted in Figure 4.23 displaying the angle θ made by the longest radius D_p with the horizontal. About 20% of the pores are oriented between 60° and 90°. The other 80% of the pores is distributed between 0° and 60° but no significant preferential orientation can be noticed. Finally, no difference was observed between the orientation of small and large pores.

---

[1] more porous samples (75% dense) are found to be not adapted for this type of evaluation since the pores are not fully closed, therefore hardly fitted by an ellipse with a good agreement.

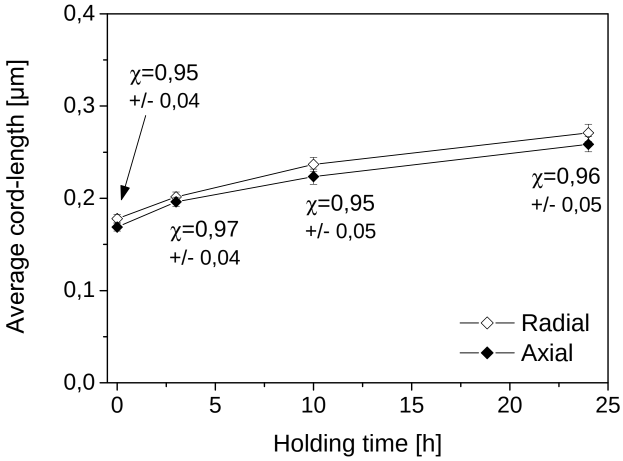

Figure 4.21.: Influence of the sintering time on the average cord-length during the dwell time of loading sintering measurements (150 N) at 1350 °C and with dense samples (χ is the anisotropy factor)

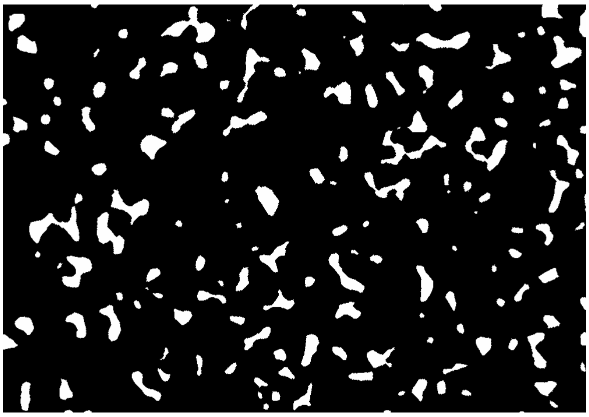

Figure 4.22.: Binary-converted images taken by SEM of a porous ZrO_2 body (85% relative density), in black: the ZrO_2, in white: the pores

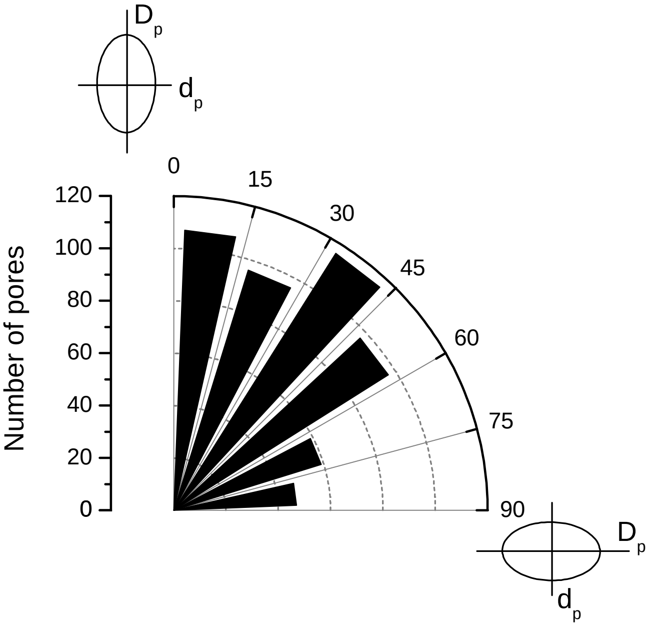

Figure 4.23.: Pore distribution classified according to their orientation in a 85% dense structure sintered under 150 N: with 0° the pore is oriented along the axial direction (parallel to the load), with 90° the pore is oriented along the radial direction.

5. Model validation

5.1. Validation procedures

5.1.1. Procedure for the validation of the sintering kinetics with the MSD

The MSD is validated by comparing the predicted sintering kinetics and experimental results. The validations include measurements with and without external load with the MSD constructed for the ZrO_2 compacts (Chapter 4). An application program is required to “read” and make sintering kinetics predictions using the time iterative process described in Figure 2.2. Such program was edited at the Fraunhofer Institute ISC.

The loading memory of the material and its incidence on the sintering kinetics were often highlighted in Chapter 4. The corrections for the loading memory can be done directly with the application program adding a parallel calculation, for example: let consider one sintering measurement where the load jumps from 0 N to 100 N at a time t_0. About 100 min before t_0, a calculation of the sintering kinetics for 100 N runs in parallel too (of course the application program gives out only the sintering kinetics with 0 N). At t_0, the strain calculated for 100 N in the time segment before t_0 is used to calculate the new strain rate.

At the time of writing this work, the thermal history is not considered in the application program. This is a crucial point to keep in mind for the interpretation of the comparisons predictions and experimental results. With the implementation of thermal history, better predictions can be expected.

5.1.2. Procedure for the validation of the viscous moduli

The experimental verification of the viscous moduli is based on the study of a co-sintering case. The sintering rate mismatch existing between two layers of a bi-layer (Al_2O_3 and ZrO_2) generates stresses leading to a subsequent warpage. Since the warpage is a macroscopic deformation, it must be dependent on the creep behaviour of each material, i.e. the viscous moduli.

Two ceramic tapes are experimentally investigated: one pure alumina and one fully stabilized 8Y-zirconia (see Chapter 3 for more information on the samples). The setup for the cyclic unloading method being not adapted to tape geometries, stacks are fabricated by laminating tapes (see Section 3.1.2). Therewith the comparability between the green-body properties of the single samples (sintering kinetics and viscous moduli) and the composites is ensured.

The warpage is predicted with:

- the free strain rate mismatch: the variations of the sintering kinetics due to the stresses are neglected,
- the experimentally determined viscous moduli: it is assumed that, the viscous moduli in compression equal the viscous moduli in tension.
- the warpage is predicted using two existing approaches: the models presented by Cai [49] and Kanters [4] (see Chapter 3).

5.2. Prediction of the sintering kinetics with the MSD

The first prediction is a free sintering measurement with a constant heating rate (1.5 K/min). The comparison between the predicted and the measured strains is done in Figure 5.1. The deviation between the prediction and the measurement is:

- the average deviation:	0.004
- the maximum deviation:	0.009 at t= 510 min is about 9%.

Prediction and measurement are in good agreement. The average deviation indicates a systematic temperature shift of about 7 °C. The time-iterative algorithm of the MSD is verified (but not shown)

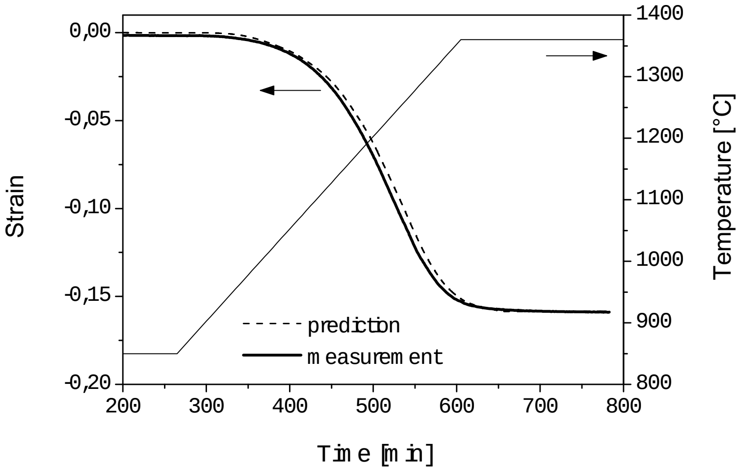

Figure 5.1.: Predicted free sintering strain of a measurement with constant heating rate (1.5 K/min) compared to the experimental measurement

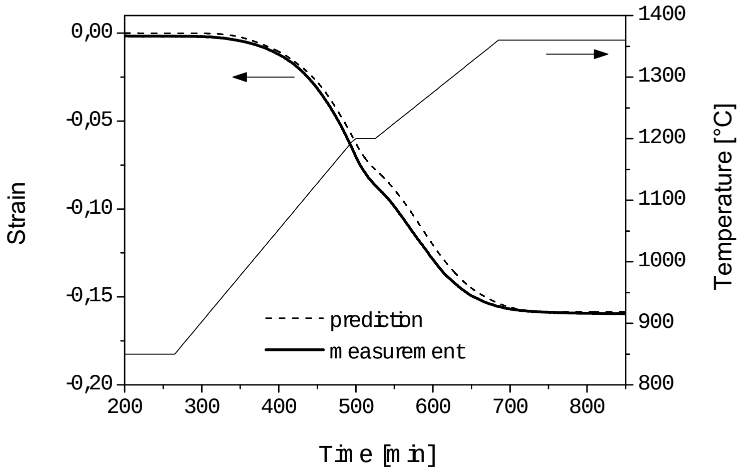

Figure 5.2.: Predicted free sintering strain of a thermal treatment with a temperature dwell at 1200°C compared to the experimental measurement

by predicting input data of the MSD. Consequently, the small temperature shift is attributed to different measuring conditions between the input data and the verification measurement (for instance aging of thermocouple over several months).

For another validation case, a 30 min temperature dwell at 1200 °C is introduced between two constant ramps of 1.5 K/min (before 1200 °C) and 1 K/min (after the temperature dwell). The comparison of the predicted and measured strains are given in Figure 5.2. The deviation between the prediction and the measurement is:

- the average deviation: 0.004
- the maximum deviation: 0.010 at t= 570 min is about 9%.

Like in the previous validation case, a systematic temperature shift of about 7 °C is observed (phenomenon explained in the previous paragraph). During the temperature dwell the agreement becomes less accurate for a restricted time beyond which the systematic temperature shift is reproduced. This temporary failure is intrinsic to the sintering kinetics prediction with changes of the temperature ramp and without consideration of the thermal history: the densification prediction with the MSD interpolates from one to another iso-strain line without considering current microstructure state. With slower heating rate, larger contribution of the surface diffusion is expected suggesting coarser microstructure than at higher heating rate, though having the same density (see Chapter 7). After a restricted time, the microstructure states are comparable again and the prediction becomes more accurate.

The variation of the sintering kinetics being created by the change in external load is predicted with two 3-step-measurements:

- the run 1 simulates a unloading step according to (1) the load is set at 50 N, (2) the load is increased to 150 N between 1100 °C and 1250 °C, (3) the load is finally set back to 100 N;

- the run 2 simulates a loading step according to (1) the load is set at 50 N, (2) the load is totally released between 1100 °C and 1250 °C, (3) the load is set to 100 N;

Both predicted and measured axial and radial strains are separately plotted for the run 1 (load release) in Figure 5.3 and for the run 2 (load increase) in Figure 5.4. The deviation between the prediction and the measurement is given in Table 5.1. The predictions of axial strain rates for both runs are less accurate during the last loading stage (during a dwell at 1350 °C). This effect is caused by the thermal memory of the material, like during the dwell time in the validation experiment in Figure 5.2.

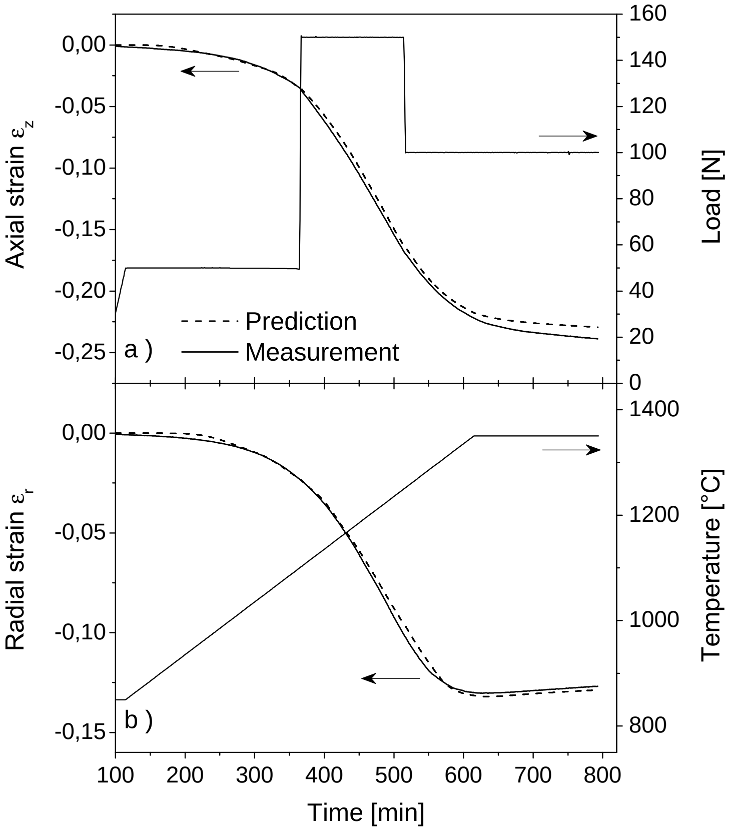

Figure 5.3.: Prediction by the MSD of the a) axial and b) radial strains of a sintering sample under uniaxial variable load (50 N - 150 N - 100 N) compared to the experimental measurement

Table 5.1.: Deviations between prediction of the sintering kinetics and measurement with variable load

		Average deviation	Maximum deviation
run 1	axial strain	0.004	0.010 at 800 min is ≈ 4%
	radial strain	0.002	0.006 at 520 min is ≈ 5%
run 2	axial strain	0.005	0.015 at 800 min is ≈ 7%
	radial strain	0.003	0.008 at 550 min is ≈ 6%

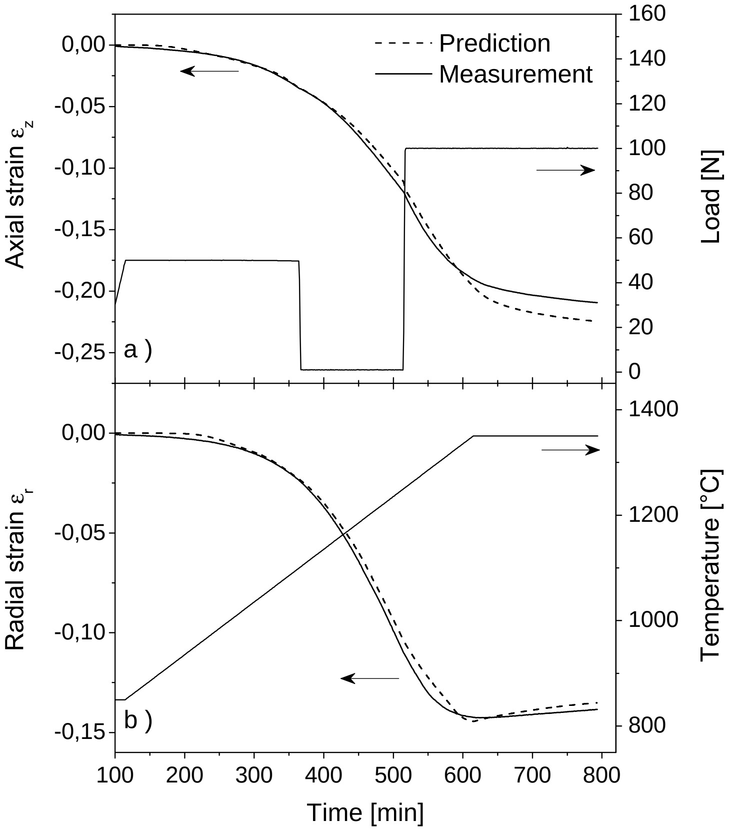

Figure 5.4.: Prediction by the MSD of the a) axial and b) radial strains of a sintering sample under uniaxial variable load (50 N - 1 N - 100 N) compared to the experimental measurement

5.3. Prediction of the warpage of a bi-layer with the experimentally determined viscous moduli

5.3.1. Free sintering mismatch between alumina and zirconia stacks

The free sintering strains for the Al_2O_3 and the ZrO_2 stacks are given in Figure 5.5 for only one heating ramp (2 K/min). Two singularities are remarkable on these curves: (i) the shrinkage in the axial direction is larger than in the radial direction, although only 1 N is applied on each sample, (ii) the shrinkage mismatch between the Al_2O_3 and the ZrO_2 stacks is evident (direction considered). Repeated experiments show similar behaviour; therefore a dysfunction of the loading setup can be excluded. The final relative densities are 0.93 for the Al_2O_3 stack and 0.97 for the ZrO_2 stack.

About the differential shrinkage of either sample, it could be argued that the uniaxial compression of 1 N leads to such anisotropic state. However, this was not the case in the first study of this work (see Figure 4.1) and since the materials are similar, this hypothesis can be excluded. The anisotropy created during the tape-casting process [12] is a plausible explanation with either (i) a density gradient in the thickness due to the segregation of the powder particles in the wet state or (ii) a texturization of green-body due to the orientation of non spherical powder grains along the casting direction. In both cases, the microstructure topology is different in the thickness direction and in the casting direction, thus anisotropic shrinkage is generated. Furthermore the microstructure investigations of sintered samples attest the presence of flaws in the materials (see an illustration in Figure 5.6 for an Al_2O_3 stack). These flaws arise from the lamination of the stacks and cause heterogeneous sintering and a lower measurement quality.

5.3.2. Characterization of the viscous moduli of alumina and zirconia stacks

The viscous moduli η_v and ν_v for the Al_2O_3 and ZrO_2 stacks are obtained using the cyclic unloading method with one load (150 N). The procedure is repeated with four heating ramps between 0.25 K/min and 2 K/min. The results η_v are plotted for the Al_2O_3 in Figure 5.7 and for the ZrO_2 in Figure 5.8. For both materials, the competition of increasing temperature and increasing density leads to the successive decrease and increase of η_v. The transition between the two regimes is reached for approximately the same temperature range 1200 °C to 1250 °C corresponding to 68% and 60% of relative density for the Al_2O_3 and ZrO_2 stacks respectively.

The viscous Poisson ratio ν_v is also given for the Al_2O_3 stack and the ZrO_2 stack in Figures 5.9 and 5.10 respectively. For both materials, the ν_v values are in the expected range 0 to 0.5. The experimental data are fitted with an exponential (like in Section 4.3.2) function of the form $\nu_v = A_0 + A_1 \exp(\bar{\rho}/A_2)$ which parameters and deviations to the experimental values are given in Table 5.2. The fit describes the increase of viscous Poisson ratio from a finite value between 0 and 0.1 to a maximum close to 0.3 for the maximum density. Note that the densities are slightly

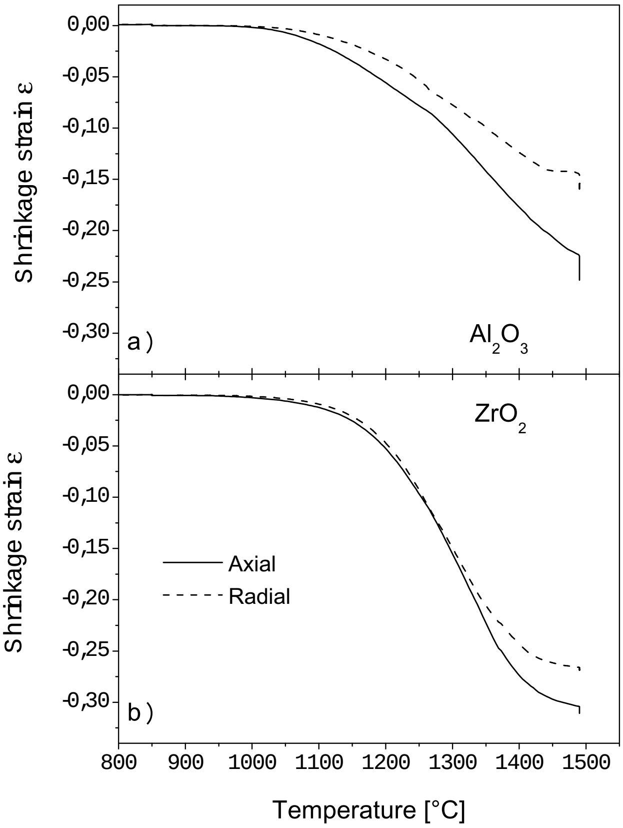

Figure 5.5.: Free sintering shrinkage strains of a) Al_2O_3 stack and b) ZrO_2 stack in axial and radial direction (heating rate: 2 K/min)

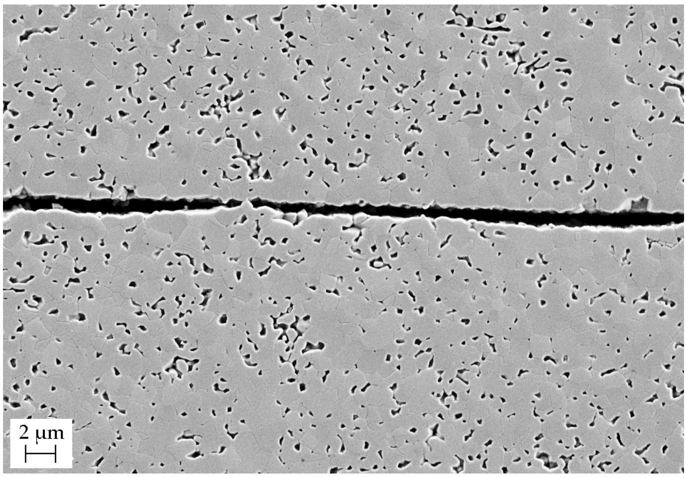

Figure 5.6.: SEM image of the microstructure of a sintered Al_2O_3 stack showing the delamination flaws at the interface between two tapes (SE detector, Magnification 25000X, WD 3 mm, voltage 5 kV)

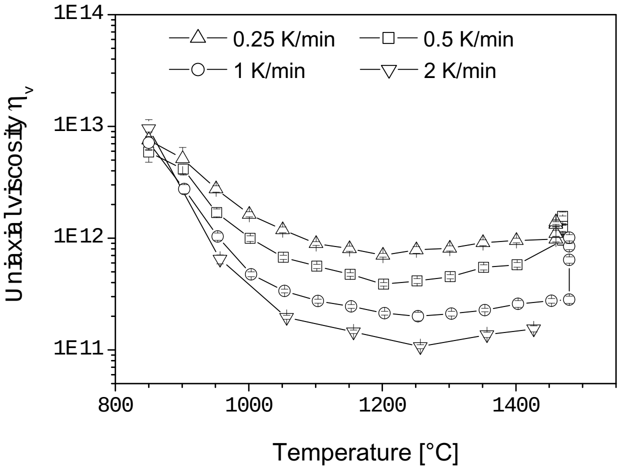

Figure 5.7.: Uniaxial viscosity η_v of sintering Al_2O_3 stacks calculated from cyclic unloading measurements under 150 N and 4 heating rates: 0.25 K/min, 0.5 K/min, 1 K/min and 2 K/min

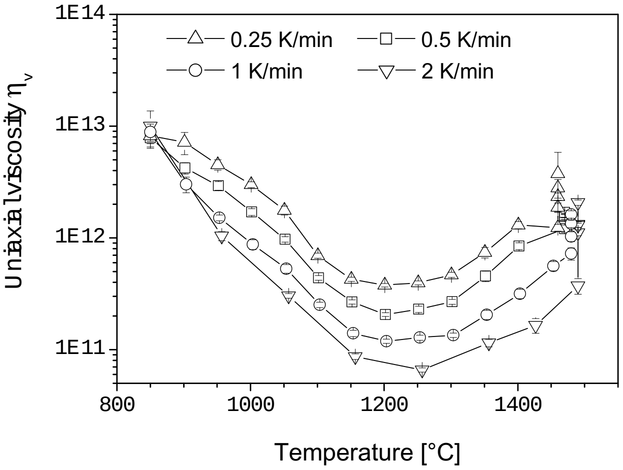

Figure 5.8.: Uniaxial viscosity η_v of sintering ZrO_2 stacks calculated from cyclic unloading measurements under 150 N and 4 heating rates: 0.25 K/min, 0.5 K/min, 1 K/min and 2 K/min

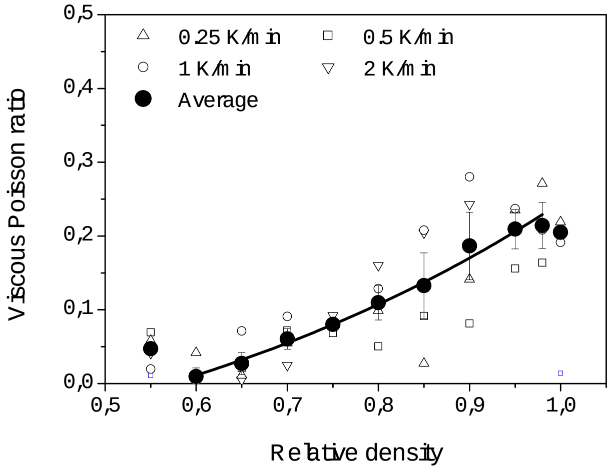

Figure 5.9.: Experimental and fitted viscous Poisson ratio of sintering Al_2O_3 stacks determined with 4 heating rates: 0.25 K/min, 0.5 K/min, 1 K/min and 2 K/min

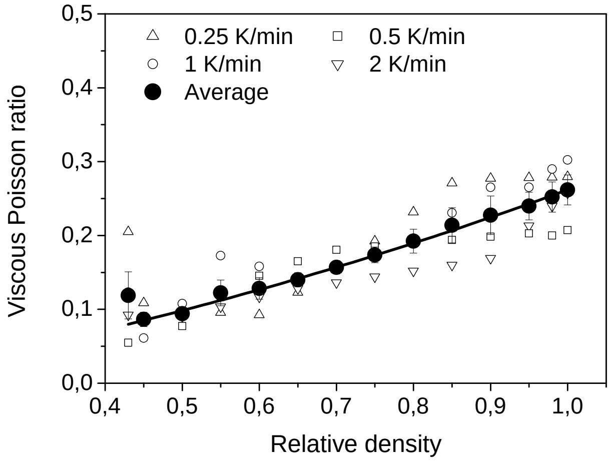

Figure 5.10.: Experimental and fitted viscous Poisson ratio of sintering ZrO_2 stacks determined with 4 heating rates: 0.25 K/min, 0.5 K/min, 1 K/min and 2 K/min

overestimated (approximately 5%) due to the exaggerated inverse barrelling (sample diameter is smaller in the middle part than at both ends).

The viscous Poisson ratio can be differently formulated from the Eqs. 2.7 with:

$$\nu_v = -\frac{\Delta\dot{\varepsilon}_r}{\Delta\dot{\varepsilon}_z} = \frac{\dot{\varepsilon}_r^{loaded} - \dot{\varepsilon}_r^{unloaded}}{\dot{\varepsilon}_z^{loaded} - \dot{\varepsilon}_z^{unloaded}} \tag{5.1}$$

In the case of an anisotropic green-body where $\dot{\varepsilon}_r^{unloaded} < \dot{\varepsilon}_z^{unloaded}$, it can be expected that $\dot{\varepsilon}_r^{loaded} \leq \dot{\varepsilon}_z^{loaded}$. According to Eq. 5.1, the viscous Poisson ratio ν_v is apparently diminished. Experimentally, a maximum value for ν_v of 0.3 is found.

Finally, bulk (K_v) and shear viscosities (G_v) are calculated and plotted in an Arrhenius form (see Figure 5.11 for Al_2O_3 and Figure 5.12 for ZrO_2) with straight iso-strain lines.

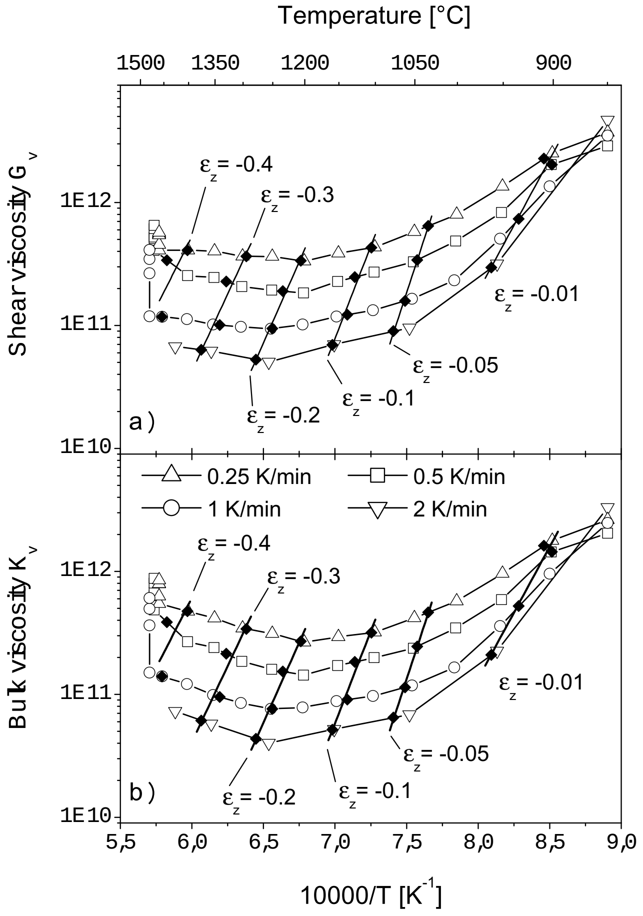

Figure 5.11.: a) Shear viscosity G_v and b) bulk viscosity K_v as function of the inverse of temperature measured for the Al_2O_3 stacks with 150 N and 4 heating rates 0.25 K/min, 0.5 K/min, 1 K/min and 2 K/min.

Table 5.2.: Parameters for the exponential fit with the form $\nu_v = A_0 + A_1 \exp(\bar{\rho}/A_2)$ of the viscous Poisson ratio and the deviation to the experimental points for the Al_2O_3 and ZrO_2 stacks

	A_0	A_1	A_2	Av. deviation	Max. deviation
Al_2O_3	-0.044	0.013	0.335	0.017	20% at $\hat{\rho} = 0.9$
ZrO_2	-0.288	0.271	1.414	0.006	32% at $\hat{\rho} = 0.43$

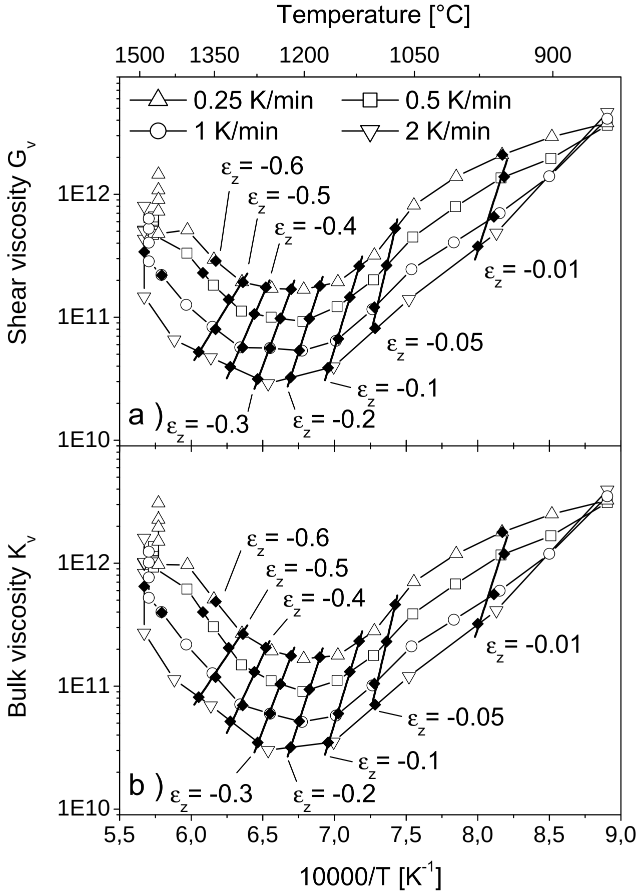

Figure 5.12.: a) Shear viscosity G_v and b) bulk viscosity K_v as function of the inverse of temperature measured for the ZrO_2 stacks with 150 N and 4 heating rates 0.25 K/min, 0.5 K/min, 1 K/min and 2 K/min.

5.3.3. Prediction of the curvature rate of a bi-layer

The prediction of the warpage of the bi-layer Al_2O_3-ZrO_2 is done analytically with the models of Cai [49] and Kanters [4] (see Section 3.2.5.3) using the measured free sintering strain rates and the experimentally determined viscous moduli. The warpage predictions for a constant heating rate of 2 K/min are given in Figure 5.13 together with the experimental warpage. The deviation between the prediction and the measurement is given in Table 5.3.

The prediction of the warpage of the bi-layer (given as curvature rate) is qualitatively in good agreement with the experimental warpage. The prediction is quantitatively worse, but can be partly explained by the small number of data points. Furthermore, four strong side-effects are not considered in these predictions:

1. the viscous properties of the materials are strongly affected by the anisotropy of the green-body (tape processing).
2. The mechanical loading is being applied in the axial direction when the stresses in the bi-layer occur in the in-plane direction (radial direction for the stack).
3. The predictions assume equal viscous behaviour under compressive and tensile stresses. This is not verified in this work.
4. The prediction is based on the free sintering rate mismatch and the loading history is ignored. The stresses which are estimated with Cai's model [49] by 1 to 3 MPa are indeed relevant for generating pore anisotropy and a loading history.
5. The coupling of creep between axial and radial directions are ignored.

Table 5.3.: Deviations between the prediction after Cai and Kanters and the measurement for the warpage of a bi-layer Al_2O_3/ZrO_2

	Average deviation	**Maximum deviation**
Cai's model	1.7×10^{-6}	4.1×10^{-6} by 1350 °C is ≈ 27%
Kanters' model	2.2×10^{-6}	6.9×10^{-6} by 1350 °C is ≈ 45%

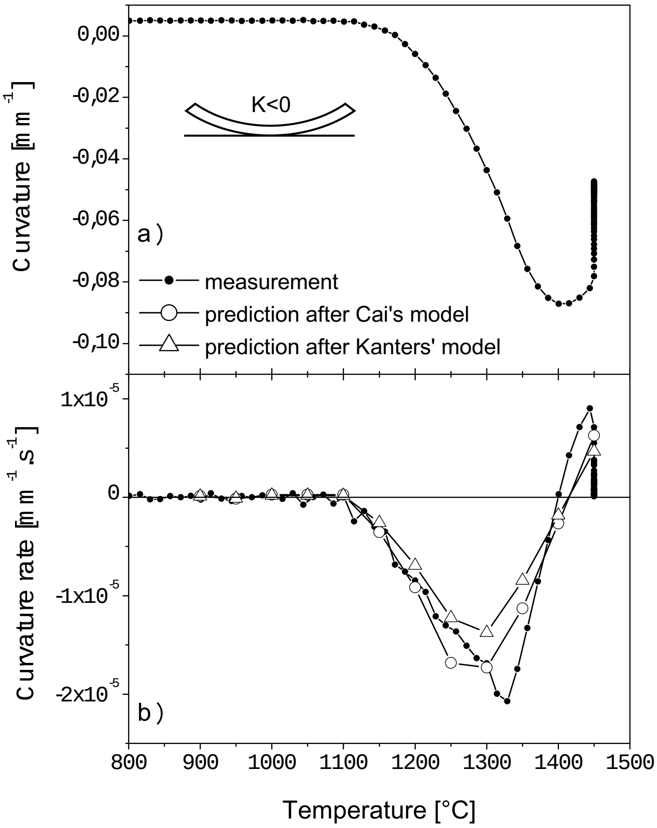

Figure 5.13.: Experimentally measured warpage and prediction according to Cai's [49] and Kanters' models [4] of a bi-layer Al_2O_3/ZrO_2 with constant heating rate of 2 K/min. In this experiment, the ZrO_2 tape is placed on the top of the bi-layer, the three Al_2O_3 tapes are in contact with the supporting plate.

6. Co-sintering of a glass-ceramic and alumina bi-layer

6.1. Foreword

The case of a layered composite fabricated by lamination of a glass-ceramic tape (GC) and an Al_2O_3 tape is studied in this chapter. As already seen in Chapter 5 the sintering rate mismatch is expected to generate warpage of the bi-layer.

Two singularities in this studies have to be noted:

1. the sintering temperature does not exceed 890 °C, being though sufficient for the densification of the glass-ceramic material. However no shrinkage of the Al_2O_3 is expected in this temperature range (experimentally demonstrated in Section 6.4.1).
2. Part of the glass contained in the glass-ceramic undergoes crystallization during the thermal treatment. The crystallization is associated with a change of glass composition and a reduction of the glass concentration, leading to a modification of the apparent viscosity of the material.

Since not only the densification and temperature can be source of viscosity change in the glass-ceramic, it is important to investigate the crystallization, especially to figure out the onset and the degree of crystallization. Only thereafter the questions of the sintering rate mismatch and the warpage of the bi-layer are addressed.

6.2. Sintering kinetics and crystallization of the glass-ceramic tape

The sintering strain of the glass-ceramic tapes is plotted in Figure 6.1.a for 5 heating ramps between 2 K/min and 20 K/min up to 890 °C. As seen already in Chapter 4, the shrinkage curves are shifted to higher temperatures with increasing the heating rate. All measurements reach the same final shrinkage by 15% (see densities according to the Archimedes method in Table 6.1). The maximum density is reached at 890 °C independently of the heating rate apart from the measurement with 2 K/min which maximal density was reached at 870 °C. The temperature of glass-transition T_g is experimentally determined at (650 ±5)°C using the method of linear intercepts before and after T_g.

Table 6.1.: Temperatures for half of the maximal shrinkage strain and final densities according to the Archimedes method

Heating rate [K/min]	**T** [°C] for $\varepsilon = 0.5\varepsilon_{max}$	**Density** [g/cm^3]
2	811	2.97 ±0.02
5	821	2.96 ±0.02
10	827	2.95 ±0.02
15	828	2.93 ±0.02
20	833	2.96 ±0.02

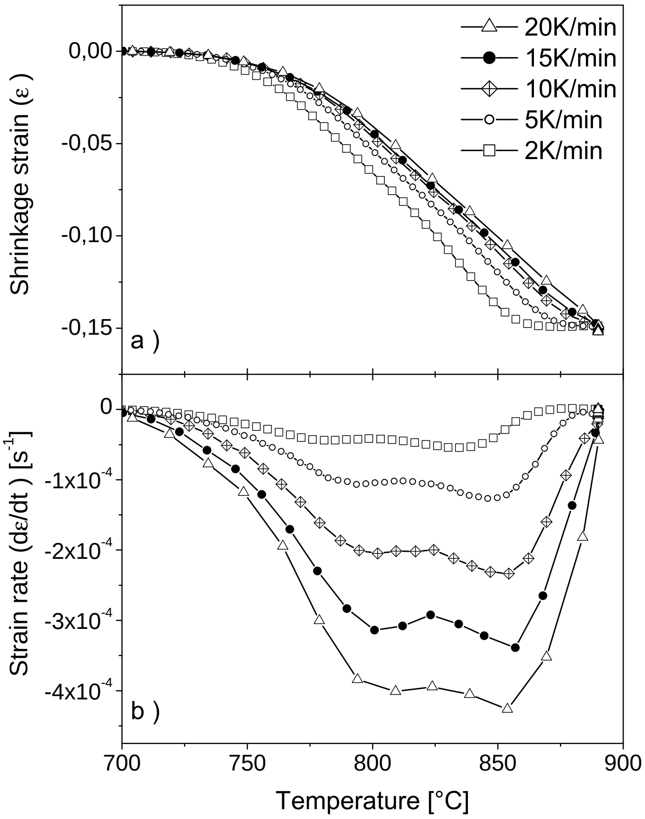

Figure 6.1.: a) shrinkage strain and b) shrinkage strain rate of the glass-ceramic tape with heating rates between 2 K/min and 20 K/min

The time derivative of the strain is plotted in Figure 6.1.b for the same 5 heating rates. The maximum shrinkage rate of this material is between 10 and 100 times faster and about 400 °C less than the ZrO_2 sample studied in Chapter 4 (see Figure 4.6). This is a good indication for viscous sintering behaviour. The kinetic-field (KF) for this material can be reformulated from a general equation for viscous sintering [53]

$$\dot{\hat{\rho}} = C_4(\rho) \times exp\left(\frac{-Q}{RT}\right) \tag{6.1}$$

with $\dot{\hat{\rho}}$ is the time-derivative function of the relative density ($\hat{\rho}$ was calculated using the strain values using Eq. 3.1 and assuming isotropic shrinkage). The KF and the iso-density lines (see Chapter 2 for a detailed description of the KF construction) for the glass-ceramic is given in Figure 6.2. All curves exhibit qualitatively the same trend, suggesting the conservation of the undergoing mechanisms (sintering but also possible chemical reaction and crystallization) independently of the heating ramp. However it can be noticed the unexpected presence of two local maxima (and one local minimum) instead of only one maximum for Al_2O_3 and ZrO_2 sintering rate curves (see Chapters 4 and 5). According to the KF, the minimum in sintering rates is reached for all heating rates by 80% of relative density (0.80 iso-density line) and the local maxima by 70% and 90% respectively.

Apart from this local minimum at 80% of relative density, the overall curve shape can be attributed to the competition of the increase of temperature and the densification. None of these can explain the local minimum but a transient chemical reaction within the glass or between the glass and the Al_2O_3 inclusions is a plausible explanation.

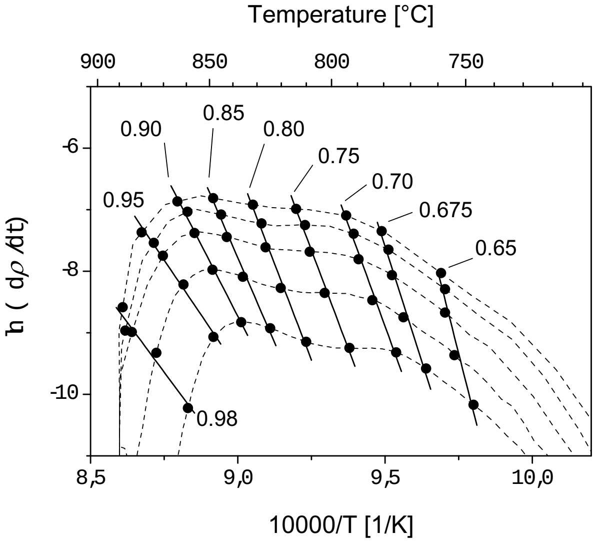

Figure 6.2.: Kinetic-field of densification rate for the glass-ceramic built with 5 heating rates (2, 5, 10, 15 and 20 K/min) and iso-density lines between 65% and 98% of relative density

The diffractogram 2θ of a sintered sample at 890 °C with 20 K/min is presented in Figure 6.3. Only two distinct crystalline structures are detected: the corundum (Al_2O_3) is identified with (◆) and the anorthite ($CaAlSi_2O_8$) with (○).

Furthermore the evolution of the phase distribution during sintering is investigated with quenched samples at several steps: 750 °C, 800 °C, 850 °C, 890 °C then after 10 min at 890 °C and finally at 750 °C during cooling (using 20 K/min heating rate). The quantitative phase distribution is given in Figure 6.4.

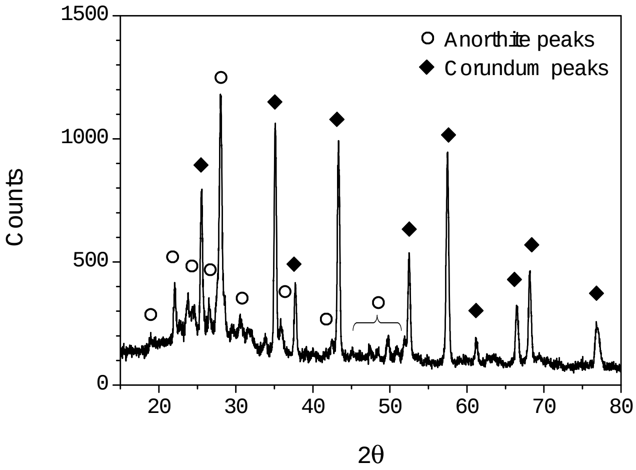

Figure 6.3.: Diffractogram of the glass-ceramic tape at room temperature after sintering at 890°C with 20 K/min and cooling with 5 K/min

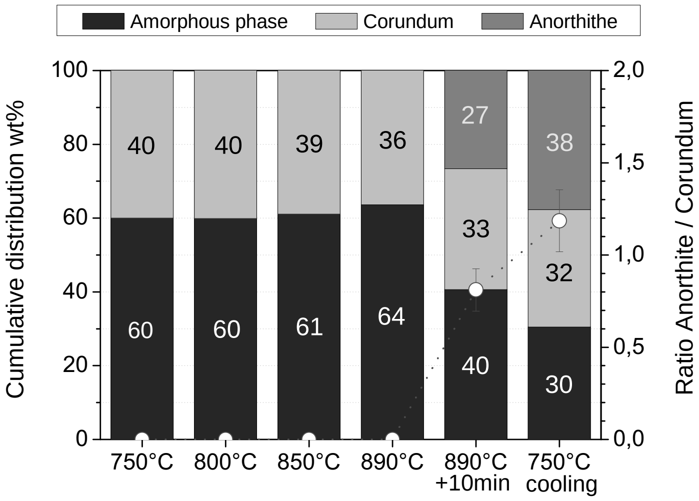

Figure 6.4.: Evolution of the phase distribution {glass-alumina-anorthite} during sintering at defined temperatures (20 K/min). The symbols (○) give the ratio of crystalline phases anorthite over corundum.

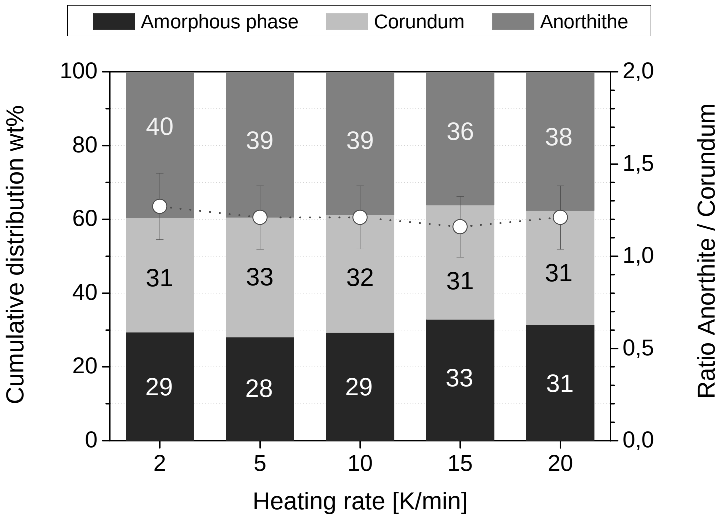

Figure 6.5.: Influence of the heating rate on the phase distribution {glass-alumina-anorthite} in the glass-ceramic after sintering (20 K/min). The symbols (○) give the ratio of crystalline phases anorthite over corundum.

The initial mixture is confirmed to be 60 wt% glass and 40 wt% corundum with the sample quenched at 750 °C. No other crystalline phase is identified at this temperature. With the temperature increase, the fraction of Al_2O_3 tends to decrease. Since no other crystalline phase is identified, the Al_2O_3 grains probably dissolve into the glass. Any new crystalline phase cannot be excluded but the amount is too little to be detected (below 1 %). In total, almost 4 wt% of Al_2O_3 dissolves into the glass up to 890 °C. Anorthite is first detected after 10 min at 890 °C indicating the onset of crystallization during the dwell time at 890 °C. The crystallization goes on during cooling as demonstrated by the XRD analysis of the sample quenched at 750 °C. About half of the glass and 10% of the Al_2O_3 particles are consumed after crystallization.

The influence of the heating rate is investigated by characterizing the phase distribution of samples sintered with 5 different heating rates (see Figure 6.5). The same cooling rate (5 K/min) is applied for five experiments, therefore the same final phase distribution is expected only if the heating has no influence on the crystallization. The phase distribution {glass-anorthite-corundum} does not indicate a significant difference between the heating rates. Furthermore the sintering kinetics curves are very similar (see Figure 6.1), suggesting the conservation of the sintering mechanisms and also no obvious presence of crystallization. Consequently, it is concluded that the crystallization started during the dwell time at 890 °C whatever heating rate was used and after the complete densification: the glass-ceramic tape densifies by viscous flow.

6.3. Viscosity measurement of the glass-ceramic tape

The loading dilatometry is performed for the viscosity determination of the glass-ceramic. However this approach is found inappropriate due to incompatible technical requirements: the viscosity of the material is such low, that sample barrelling appears[1] even with the lowest load achievable with the loading setup (20 kPa). One solution to prevent barrelling is the increase of the sample diameter. However a much larger diameter generates thermal gradients and a worse sintering homogeneity. No satisfying experimental compromise can be found; therefore another method must be used for the determination of the viscosities: the bending of tapes under gravity.

The deflection of a GC stripe is measured with the optical dilatometer (see setup in Section 3.2.4.3). Using Eq. 3.7, the viscosity of a sintering glass-ceramic tape is calculated and is given in Figure 6.6 as function of temperature for heating ramps between 2 K/min and 20 K/min. Before 650 °C, there is no measurable bending of the stripes since the material viscosity is still very high. Bending is recorded above 650 °C corresponding to the temperature of glass transition of this material. Large deflections are monitored just beyond the T_g, and reveal a reduction of the glass viscosity. In the range 750 °C till 850 °C, there is an increase of the apparent viscosity of the GC material. Comparing the plots in Figures 6.1 and 6.6 the temperatures of the local maximum in viscosity match these of the local minimum of free shrinkage rate. A contribution to the increase of viscosity by the dissolution of the Al_2O_3 particles in the glass (see Figure 6.4) cannot be excluded. However, beyond this local maximum of viscosity, the viscosity drops again and cannot be justified by the dissolution of the alumina. Except the measurement with 2 K/min which remains in its position, all samples fall off from the setup due to combined asymmetric shrinkage (probably due to fric-

---

[1] the barrelling is a heterogeneous deformation of the sample diameter, larger in the middle part than at both ends.

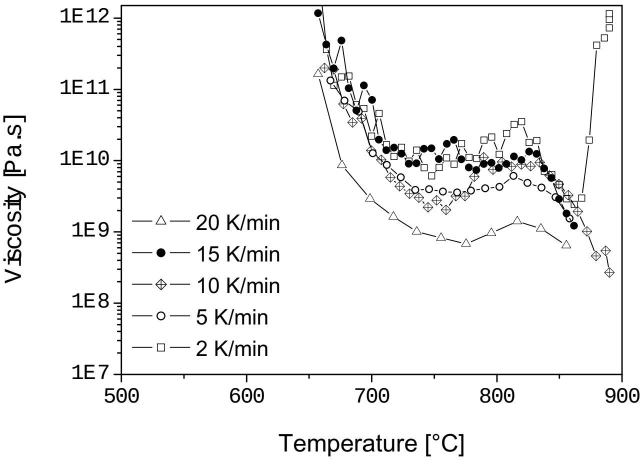

Figure 6.6.: Viscosity of the glass-ceramic versus temperature for several heating rates: 2 K/min, 5 K/min, 10 K/min, 15 K/min, 20 K/min

tion on one or the other supporting rod) and large bending of the stripes. The viscosity curves with heating rates between 2 K/min and 20 K/min differ by about one order of magnitude over the measurement (significantly less if the measurement with 20 K/min is excluded): at 800 °C, the viscosity is in the range 1 GPa.s to 11 GPa.s for the heating rates between 2 K/min and 20 K/min. However there is no apparent ordering of the curves with the heating rate suggesting thereby that, the observed difference between the measurements stems from the large scattering of the data.

6.4. Co-sintering of a bi-layer glass-ceramic/alumina

6.4.1. Sintering mismatch

The dimensional changes of the GC and Al_2O_3 tapes during thermal treatment up to 890 °C (20 K/min heating rate) are presented in Figure 6.7. In contrast to the glass-ceramic tape, the Al_2O_3 tape does not shrink in this temperature range and exhibits only thermal expansion (the experimental determination of the linear thermal expansion gives a value of 8.2 ppm/°C).

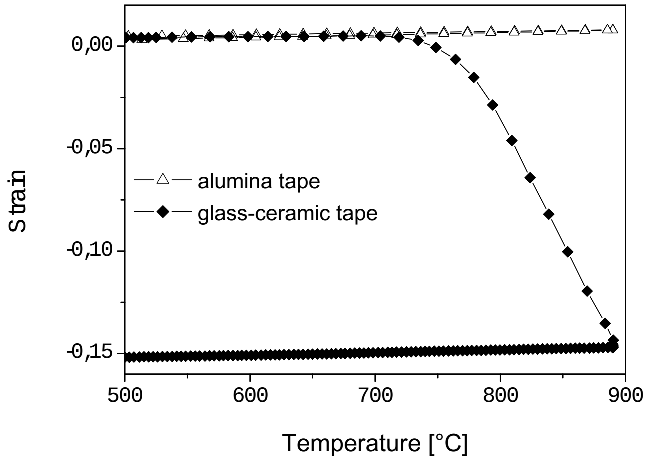

Figure 6.7.: Dimensional changes (strain) in temperature up to 890 °C of the glass-ceramic tape and the Al_2O_3 tape (20 K/min heating rate)

6.4.2. Qualitative description of co-sintering

As already seen in Chapter 5, the sintering rate mismatch leads to the generation of stresses and warpage of the bi-layer GC/Al_2O_3. The absolute curvature is presented during the heating phase in Figure 6.8.a (up to 890 °C with 20 K/min and hold for 10 min). The glass-ceramic tape being on top, the curvature remains negative over the whole measurement (with both ends pointing upwards). The markers A to F are placed on the curves in order to help a description and a discussion segment-per-segment. Additionally, the strain rate mismatch in Figure 6.8.b is illustrated by the strain rate difference $\{\dot{\varepsilon}_{(GC)} - \dot{\varepsilon}_{(Al_2O_3)}\}$ together with the warping rate (curvature rate).

Segment A-B:

The temperatures of this segment remain below the onset of sintering of the glass-ceramic tape (about 650 °C). The curvature increase is linear and can be attributed to the linear elastic thermal expansion difference between both tapes: the Al_2O_3 has a larger coefficient of thermal expansion (CTE).

Segment B-C:

Within this temperature segment, the glass-ceramic tape does not start shrinking, nevertheless a reduction of the curvature is observed. The elastic mismatch or the sintering onset of the glass-ceramic tape cannot justify the deformation of the bi-layer. However, the temperature has reached the domain of the glass transition T_g (≈ 650 °C) being characterized by a large reduction of the viscosity. The stresses in the composite are thus released by viscous deformation of the GC tape

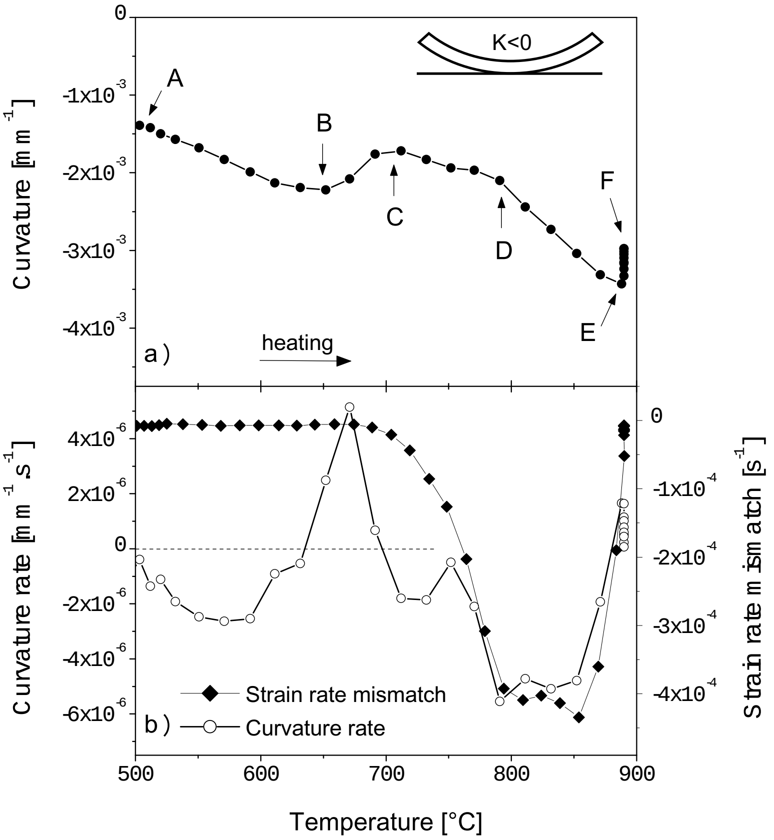

Figure 6.8.: a) Curvature of a bi-layer GC/alumina during heating (the stripe is oriented with the glass-ceramic tape on top) and b) comparison of the curvature rate of the same bi-layer with the sintering mismatch expressed as the strain rate difference $\{\dot{\varepsilon}_{(GC)} - \dot{\varepsilon}_{(Al_2O_3)}\}$ with 20 K/min

leading to the flattening of the stripe with help of the elastic behaviour of the alumina tape. An additional contribution of the gravity to the reduction of curvature cannot be excluded.

Segment C-D-E:

Larger curvature is built up in this temperature range. It can be attributed to the sintering shrinkage of the GC tape as shows the good match between the strain rate difference and the curvature rate in Figure 6.8.b. As shrinkage slowed down, the curvature reaches a maximum (-3.5×10^{-3} mm^{-1}).

Segment E-F:

During the holding time at 890 °C, a reduction of the curvature between -3.5×10^{-3} mm^{-1} and -3.0×10^{-3} mm^{-1} is observed. During the holding time, no more shrinkage of the glass-ceramic is expected (see Section 6.2).

The warpage behaviour is similar to that described in the segment B-C with combined effect of the elastic behaviour of the Al_2O_3 tape and the low viscosity of the GC tape. A contribution of the gravity cannot be excluded. During the early stage of crystallization, the anorthite crystals are likely to be isolated within the glass (like inclusions) and having thus no significant contribution to the viscosity of the glass-ceramic.

Influence of the heating rate on the warpage:

The influence of the heating rate on the warpage is investigated by comparing the experimental curvature rates (see Figure 6.9). Other heating ramps (2 K/min and 10 K/min) lead to qualitatively similar warpage rate curves; only the intensity of the peaks is smaller with smaller heating rates.

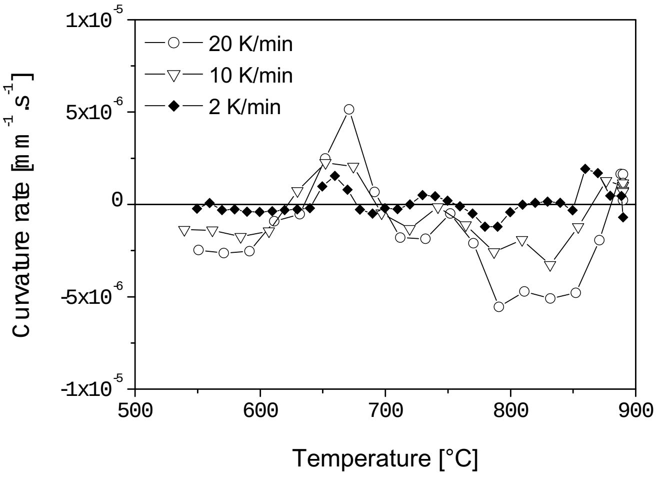

Figure 6.9.: Influence of the heating rate on the curvature rate of a bi-layer GC/alumina

Warpage during cooling:

The experimental curvature is monitored during cooling (see Figure 6.10). Three segments can be distinguished: 2 segments with decreasing curvature (F-G and H-I) separated by one segment with increasing curvature (G-H) bewteen -2.5×10^{-3} mm^{-1} and -3.8×10^{-3} mm^{-1} for temperatures between 750 °C and 650 °C.

Furthermore the relative dimensional change (related to 1 at 890 °C) for both tapes during cooling is plotted in Figure 6.11. The dimensional behaviour of the glass-ceramic tape shows also three distinct regimes so that, if α is the apparent coefficient of thermal expansion:

$\alpha_{\mathrm{GC}} < \alpha_{\mathrm{Al_2O_3}}$ between 890°C and 750°C,

$\alpha_{\mathrm{GC}} > \alpha_{\mathrm{Al_2O_3}}$ between 750°C and 650°C,

$\alpha_{\mathrm{GC}} < \alpha_{\mathrm{Al_2O_3}}$ below 650°C.

It demonstrates the non linear apparent CTE of the glass-ceramic during cooling. The temperatures of transition between the three regimes match these of the curvature changes: it shows the direct link between the CTE and the curvature.

However, most materials are known for having one monotonous CTE. This unusual behaviour can only be explained by the interplay of another mechanism to the thermal expansion. During crystallization the simultaneous consumption of the glass (ρ= 2.6 g/cm^3) and anorthite crystallization (ρ= 2.8 g/cm^3) lead to a volume reduction. Above 750 °C the thermal contraction added with the volume reduction due to crystallization generate a larger apparent volume contraction. This effect stops by 750 °C, very likely with the end of the crystallization. The transition at 650 °C corresponds to the T$_g$ of the rest glass associated to the classical change of thermal expansion behaviour.

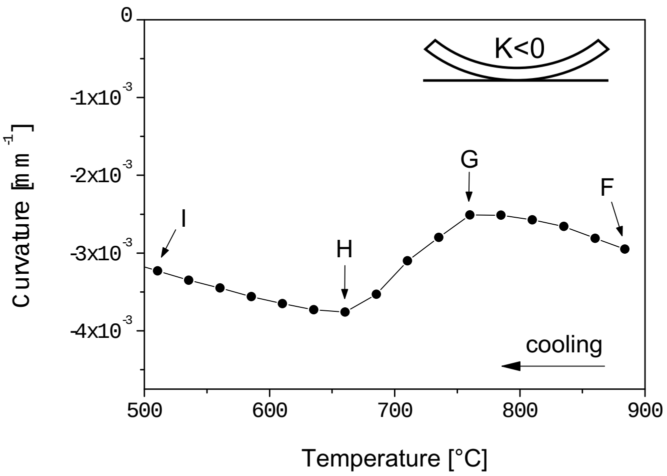

Figure 6.10.: Curvature of a bi-layer GC/alumina during cooling

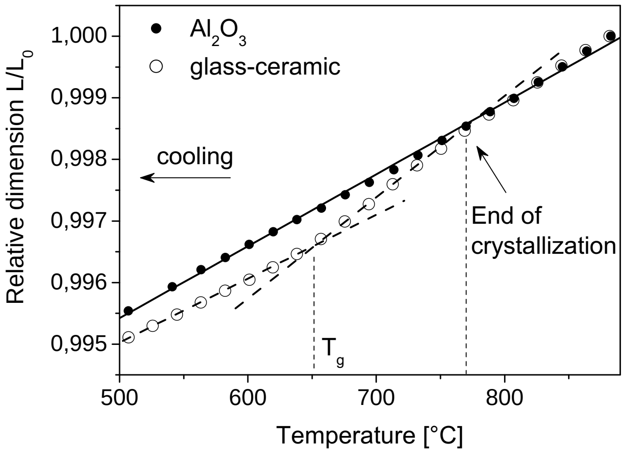

Figure 6.11.: Relative dimensions of the glass-ceramic and Al_2O_3 tapes during cooling

6.5. Conclusions on the co-sintering case of a glass-ceramic and alumina bi-layer

With the study of the glass-ceramic and alumina bi-layer, the following conclusions can be made:

- This glass-ceramic material densifies by viscous sintering. The crystallization of the anorthite during sintering occurs after the densification of the glass-ceramic. The free sintering kinetics is plotted in a kinetic-field for eventual predictions of the sintering kinetics with other thermal treatments.
- The loading dilatometry is not an appropriate method for this material. No satisfying technical solution is found to overcome the barrelling of the test-samples.
- An alternative method for the viscosity measurement is utilized for the glass-ceramic. The measured uniaxial viscosities show a scattering by one order of magnitude (in GPa.s). This method does not give access to the sintering kinetics under external load.
- The warpage of the glass-ceramic and alumina bi-layer is studied. A large part of the curvature built during the thermal treatment is caused by the elastic linear thermal expansion mismatch. The low viscosity of the glass ensures the minimization of the stresses and the reduction of the curvature initially built up by the thermal expansion mismatch (maximum shrinkage -3.5×10^{-3} mm^{-1} at 890 °C).
- During cooling after densification, the maximum curvature is reached (-3.8×10^{-3} mm^{-1}). As the crystallization goes on during cooling, the viscosity of the glass-ceramic tape increases. Consequently the stresses built by the mismatch are not efficiently released.

7. Discussion

7.1. Free sintering kinetics and apparent activation energy

The apparent activation energy for sintering can be read from the MSD (see Chapter 4). For a ZrO_2 compact, values in the range 600 kJ/mol to 650 kJ/mol are found above 5% of strain.

The activation energy values found in the literature are presented in Table 7.1 for surface, grain-boundary and lattice diffusions. A relatively large range of value is to be noted between activation energies of one same mechanism and is certainly due to different experimental procedures and materials (impurity nature and content) used in either study. Larger E_a values for 3Y-TZP (not given in Table 7.1) were reported between 930 kJ/mol and 310 kJ/mol (between 73% and 91% of relative density) [54]. It was justified by the control of sintering kinetics by the point defect formation related to the open or closed porosity. However the irregular free sintering curves point out heterogeneous sintering of the green-bodies (study with 80 µm agglomerated powder of 100 nm grains) [11, 55]. This example illustrates the importance of having homogeneous green-bodies to be able to make meaningful conclusions.

In oxide ceramics diffusion is controlled by the slowest species (Zr^{4+}) on its fastest path: for zirconia (3Y-TZP) sintering is controlled by grain-boundary diffusion [60]. The activation energy found in the present work is in reasonable agreement with the reported activation energies. Below

Table 7.1.: Activation energy E_a found in literature for 3Y-TZP materials

Diffusion mechanism	E_a **[kJ/mol]**	**Ref.**
Surface diffusion	260	[56]
GB-diffusion	465	[56]
	470	[57]
	570	[58]
	680	[59]
Lattice diffusion	370	[59]
	515	[57]

5% shrinkage strain, the values are higher (about 750 kJ/mol). It is explained by the participation of the surface diffusion to shrinkage; although the E_a values for surface diffusion are the smallest. Having the smallest activation energy compared to grain-boundary diffusion and lattice diffusion, the surface diffusion is the mechanism active at first as temperature increases. Surface diffusion participates mostly to the coarsening and the reduction of local curvatures; thus does not directly play a role in the narrowing of the particle centres taking place during shrinkage. With smaller heating rates, the relative contribution of surface diffusion is larger than with larger heating rates, suggesting more significant coarsening, larger consumption of the sintering potential and finally the deceleration of the sintering kinetics [61] (still comparing slow and high heating rates). The iso-strain points of small heating rates are thus shifted to higher temperatures relatively to the larger heating rates (see Figure 7.1). Subsequently, the slopes of iso-strain lines are artificially increased and the apparent activation energy too. As the temperature increases, the contribution of other diffusion mechanisms (grain-boundary and lattice diffusions) becomes more important and fades out the previous effect. Above 5% shrinkage strain, the iso-strain lines apparently rotate (slight anticlockwise rotation) so that E_a apparently decreases. Two hypotheses can be formulated:

1- the change in E_a reveals a real change in sintering mechanism as temperature and/or relative density increases. Sintering is indeed a complex process in which surface diffusion, grain-boundary diffusion and lattice diffusion participate. Interplay of both mechanisms grain-boundary and lattice diffusions can lead in theory to the variation of E_a.

2- the construction of the iso-strain lines assumes the independence of C on temperature (same strain and same grain size). This assumption is further investigated in the following.

The construction of the MSD is based on Eq. 2.4 which states a linear function if C is independent

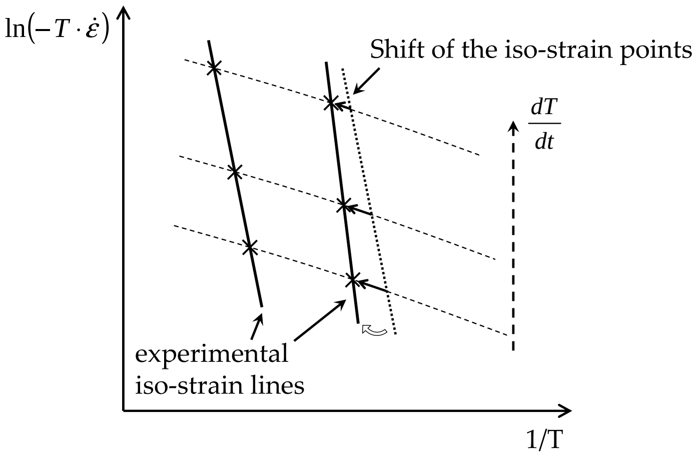
$\ln(-T\cdot\dot{\varepsilon})$
Shift of the iso-strain points
$\frac{dT}{dt}$
experimental
iso-strain lines
1/T

Figure 7.1.: Representation of the shift of the iso-strain points in the MSD due to the contribution of the surface diffusion

on temperature T. The temperature dependence of C (hypothesis 2) is modelled through the construction of new iso-strain points at defined temperatures and with a fixed activation energy (E_a= 600 kJ/mol) by setting $y = ax + b(x)$ where $y = ln(-T \cdot \dot{\varepsilon})$ (the MSD output), x is the inverse of temperature, a is the ratio -E_a/R and $b = ln(C(\rho, G, T)) = ln(p \cdot f(T))$. The parameter p is kept constant and set equal to the experimental value. Several dependences on temperature $f(T)$ (polynomial and exponential) are chosen to calculate the coordinates of new iso-strain points. In the small temperature range, each series of new iso-strain points can be linearly fitted (although the model for the new iso-strain points is not linear anymore) and the corresponding apparent E_a is extracted. The results are plotted in Figure 7.2.

In the demonstration, the slopes of the new iso-strain lines vary by ±4% around the unique activation energy (600 kJ/mol) when C is dependent on temperature. One hypothesis for the temperature dependence of C is the interplay of grain growth and densification. Grain growth is a thermally activated process and is defined with [37]:

$$G^m = G_0^m + \Psi(T)t \tag{7.1}$$

with

$$\Psi(T) = \Psi_0(\rho) \cdot exp\left(\frac{-Q_{gg}}{RT}\right) \tag{7.2}$$

where G_0 is the initial grain size, m grain growth exponent between 2 and 4 depending on mechanism, Ψ parameter depending on temperature and microstructure, Ψ_0 pre-exponential factor depending on the microstructure and Q_{gg} the activation energy for grain growth.

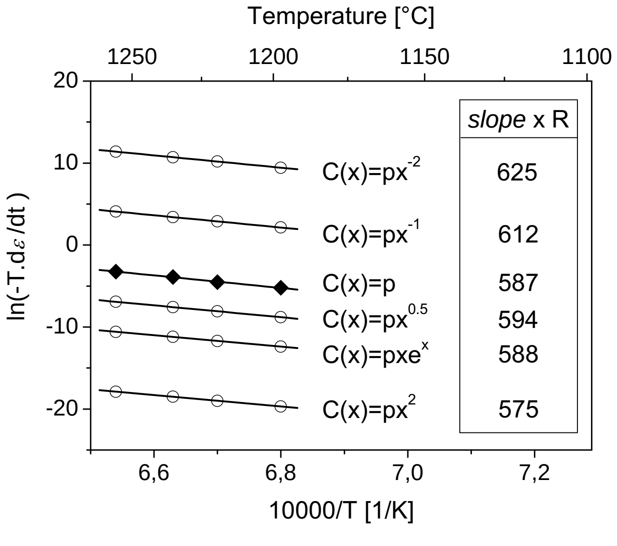

Figure 7.2.: Calculation of new iso-strain points considering the temperature dependence of C in Eq. 2.4 and the corresponding linear fits of the iso-strain points (the slopes are multiplied by the constant R). The new iso-strain points are modelled with one unique activation energy E_a=600 kJ/mol. The full diamonds are the original experimental data. (dt is in seconds, T in K and E_a in kJ/mol)

The interplay of grain growth and densification is already addressed for sintering alumina [29]. A similar phenomenon cannot be excluded for zirconia. Nevertheless the grain growth in ZrO_2 is complex to model due to (i) the coexistence of T- and F-crystalline phases at high temperature (see Table 4.3) and their differential grain growth [62] and (ii) the lack of experimental data on the grain growth of either T- and F-phase separately. The rotation of the slopes is shown in this work to be small suggesting either (A) only small grain growth or (B) control of densification and grain growth by the same diffusion mechanism. On the one hand, the hypothesis (A) is experimentally shown in this work (see Section 4.4.2). On the other hand, Wang et al. [60] concluded that the same mechanisms do control grain growth and densification in 3Y-TZP. Furthermore, the experimental activation energy reported in literature, 524 kJ/mol for grain growth in 3Y-TZP [63], corresponds also to the grain-boundary diffusion. These two latter points give more weight to the hypothesis (B). In conclusion, the hypothesis A and B remain plausible, but due to the small grain growth of the material studied in this work, it is not difficult to state further on the hypothesis (A) and (B).

It is fair to further address the question of the validity of the MSD without consideration of grain growth (or T-dependence of C). It is here argued that the MSD is a kinetic map in which interpolation and prediction of other sintering kinetics is strictly based on experimental data. The interpretation of the slope of the iso-strain lines does not interfere with the predictions of the sintering kinetics. Therefore even though some elements may not have been properly considered in the construction of the MSD from the sintering mechanism point of view, the practical use of the MSD is not hindered in any way.

7.2. Constrained sintering in zirconia

The discussion about the activation energy in Section 7.1 led to the conclusion that, the sintering of ZrO_2 is controlled by grain-boundary diffusion. Furthermore, the parallel shift of the iso-strain lines in the MSD suggests the same controlling mechanism for densification and creep. This leads to the same conclusion as Wang did, namely that creep like densification is controlled by grain-boundary diffusion [60].

For loaded experiments, the rate was shown to increase linearly with the stress (see Figure 4.3): with a larger stress, larger creep rate is expected. In contrast, the density is only slightly increased by 5% (see Figure 4.4) already at the onset of shrinkage, i.e. at low temperatures where the contribution of grain-boundary (or lattice) diffusion is small. The rearrangement of particles in the initial stage under effect of load or local plastic deformation at the neck contacts by the stress intensification effect [38] are plausible hypotheses. However these experiments reveal that creep (whatever load better 50 N and 200 N is applied) does not enhance the densification during the intermediate and the final stages. It can be argued that the sintering stress of this material (estimated in Section 3.2.5.2) is in same the range than the external stresses (1 to 5 MPa) letting a balanced competition between the contributions of densification and creep. But it does not constitute a sufficient explanation to justify clearly these experimental conclusions. No other satisfying hypothesis was found.

The loading memory of the sintering materials is illustrated by the formation of pore anisotropy during hot-forging experiments (see Figure 4.23) and by the changes of sintering kinetics (see Figures 4.6 and 4.7). In a random arrangement of spherical particles, the uniaxial external stresses are transmitted to all grains, and more especially to every grain-boundary non parallel to the load. The external stresses can be thus decomposed into one normal component to the grain boundary and one shear component along the grain-boundary. The grain boundaries exactly normal to the load undergo only compressive loads (see the grain-boundaries between the grains 1 and 3 or between 2 and 4 in Figure 7.3). Stresses are concentrated at the particle contacts having the smallest area, delivering additional diffusion potential and preferential neck growth of the grain boundaries under compression. The form of the neighbouring pores becomes slowly anisotropic and oriented along the load direction. Zuo hold the same reasoning with only four particles (like the particles 1 to 4 in Figure 7.3) and experimentally showed oriented pores after long uniaxial loading experiments with alumina samples [20]. Similar experimental investigations were also carried out with zirconia samples [64]. The same reasoning applied to the randomly distributed particles {2-4-5-7 to 9} leads to the formation of an oriented pore which orientation is not exactly parallel to the load direction but in an intermediate orientation (relevant to the experimental observations in Figure 4.23).

The increase in strain rate difference {free sintering - unloaded sequence} with the load suggests, that the degree of microstructure anisotropy is increasing with increasing the load (see Figure 4.6).

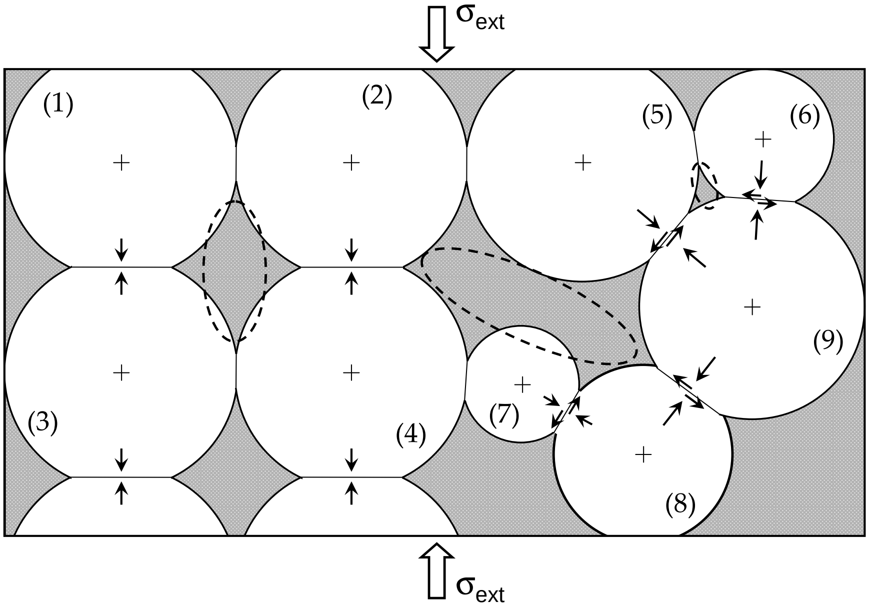

Figure 7.3.: Simplified random particle packing in a porous structure undergoing an external and uniaxial compressive load. Due to additional and stress-oriented matter displacement, there is orientation of the pore preferentially parallel to the load direction when the grains remain approximatively spherical.

Furthermore the anisotropy becomes more pronounced with time [2]. This explains probably why only a small degree of anisotropy is found in this work with 85% of relative density and almost none with 75%. Guillon et al. [65] studied the constrained sintering of Al_2O_3 coatings on a non-shrinking substrate (i.e. under tensile stresses) and observed the formation of anisotropic pores in the normal plane to the stress. All these experiments involved special conditions: only compression or only tension and during long application periods. In real co-sintering cases like with bi-layers, the stresses vary with the sintering rate mismatch, and can be successively positive and negative. Furthermore, the pore anisotropy is reduced by matter displacement over the surface, as curvature and surface energy equilibrium (dihedral angle) constantly serve the redistribution of the matter around the pore and between regions of different curvatures. In conclusion, the loading memory of the material is an implicit phenomenon of loading sintering, but its consequences on the sintering kinetics during real co-sintering measurements cannot be properly addressed in this work.

7.3. Experimental determination of the viscous moduli

7.3.1. Uniaxial viscosity

The uniaxial viscous modulus η_v quantifies the deformation of the material in the load direction. Its evolution during sintering is directly related to the temperature and the microstructure state of the porous structure (see Section 4.3.1).

The published works on experimentally determined viscous moduli are rare: the only reference found with ZrO_2 porous samples is the work done by Cai et al. [34] using the cyclic loading dilatometry. Zuo et al. [36] determined the uniaxial viscosity for Al_2O_3 samples during isotherms. The experimental results of this work are compared with the results reported in literature, the comparison of the experimental procedure is in Table 7.2 and the experimental results for the uniaxial viscosity are in Figure 7.4. The comparison of the experimental results points out the following points:

- Comparing the ZrO_2 compacts and stacks studied in this work, the uniaxial viscosities for the ZrO_2 stack are three times smaller than for the ZrO_2 compact above 70% of relative density. This difference in uniaxial viscosity is attibuted to the temperature interval between the measurements: 1150 °C for the ZrO_2 compact and 1270 °C for the ZrO_2 stack. The increase in uniaxial viscosity starts at about 60% of relative density for the stack and about 75% for the compact. The grain growth difference is a plausible explanation, as the final grain size is about 0.3 to 0.4 µm for the compact and 1.4 µm for the stack.
- The experimental results of Cai [34] reproduce the drop of uniaxial viscosity at the beginning of the measurement. However, the increase in uniaxial viscosity at high densities is

much smaller in his work and the viscosities by 90% of relative density differ by a factor 10. No explanation is found for this difference.

- The experimental results of Zuo [36] show discrepancies with the results of this work: for the lowest densities, the drop of uniaxial viscosity is not measured. The reason for that is the isotherm condition of the measurement, i.e. the suppression of the temperature contribution. The maximum values (at the maximum densities) are equal, although the densities are about different by 5% in relative. This can be explain by the overestimation of the density in the present work, due to exaggerated inverse barrelling[1].

All measurements compared in Figure 7.4 agree with the increase of uniaxial viscosity as the samples achieve full density. During an isotherm at 1350 °C, the uniaxial viscosity of fully dense ZrO_2 samples is increased by a factor of 4 during the first 5 hours, after 5 hours there is no significant increase (see Figure 4.18). Since the full density is already achieved, further increase in uniaxial viscosity can only be reached by grain growth as the number of grain-boundary interfaces is reduced. Creep is thereby reduced since less vacancy sources and sinks are available. Rearrangements of Eqs. 2.1 and 2.7 permit to make a correlation between the uniaxial viscosity and the grain growth, by writing:

$$\eta_v = \beta(\sigma, \rho^{-1}) \cdot TG^n \cdot \exp\left(\frac{Q_{gg}}{RT}\right) \tag{7.3}$$

---

[1] The inverse barrelling is a non uniform deformation of the sample due to the load with a smaller diameter in the middle than in the ends.

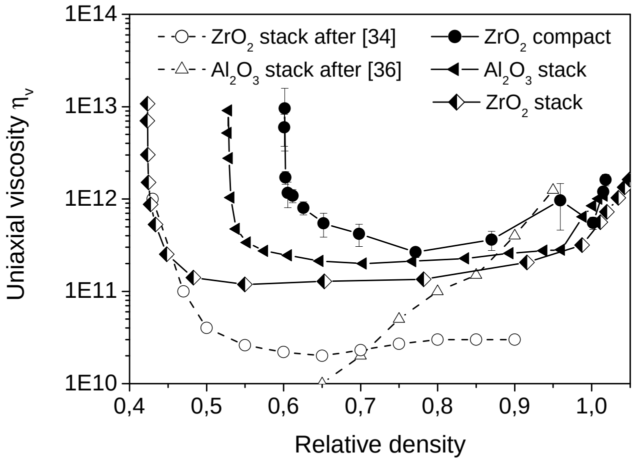

Figure 7.4.: Comparison of the uniaxial viscosity measured in this work for several samples (ZrO_2 compacts, ZrO_2 and Al_2O_3 stacks) and reported in literature for a ZrO_2 stack [34] and a Al_2O_3 [36] compact (approximate reproduction of the results from publications).

Table 7.2.: Simplified experimental procedures for the determination of uniaxial viscosity either from the present work or from the literature.

	ZrO_2 **compact**	ZrO_2 **stack**	Al_2O_3 **stack**	ZrO_2 **stack**	Al_2O_3 **compact**
Reference	**Chapter 4**	**Chapter 5**	**Chapter 5**	[34]	[36]
Material	3Y-ZrO_2	8Y-ZrO_2	99.90% Al_2O_3	TZ-12Ce	Al_2O_3
Processing	Cold isostatic pressing	Tape casting + lamination	Tape casting + lamination	Tape casting + lamination	Cold isostatic pressing
Initial relative density	0.59	0.42	0.52	0.46	0.58
Measurement method	Cyclic unloading dilatometry	Cyclic unloading dilatometry	Cyclic unloading dilatometry	Cyclic loading dilatometry	Discontinuous hot-forging
Temperature treatment	continuous heating 1 K/min 850 °C- 1350 °C	continuous heating 1 K/min 850 °C- 1480 °C	continuous heating 1 K/min 850 °C- 1480 °C	continuous heating 5 K/min RT - 1530 °C	isotherm 1250 °C
Initial grain size [µm]	0.2	0.6	0.3 - 0.4	0.2 - 0.3	0.2
Final grain size [µm]	0.3 - 0.4	5.3	1.4	1	-

where β is a parameter dependent on the applied stress and on the density, T is the temperature, G^n is the grain size and Q_{gg} the activation energy for grain growth. Taking ρ, σ, T and Q_{gg} constant during the isotherm cyclic unloading, the increase in uniaxial viscosity is directly proportional to the grain growth by:

$$\eta_v - \eta_{v,0} = k_0 \cdot \left(G^n - G_0^n\right) \tag{7.4}$$

where the subscript 0 indicates the beginning of the isotherm at the time t=0. The parameter k_0 is function of σ, ρ, Q_{gg} and T. The relation is plotted in Figure 7.5 for n between 2 to 4 (range of values usually found in literature for the grain size exponent) and using the experimental data displayed in Figures 4.18 and 4.21.

The experimental linearity between grain growth and uniaxial viscosity is not demonstrated in Figure 7.5. However large increase of grain growth and of viscosity are favourable for such analysis; this is not the case for this material (see Table 7.2, ZrO_2 compact). Consequently, no meaningful conclusion can be made on this part of the study.

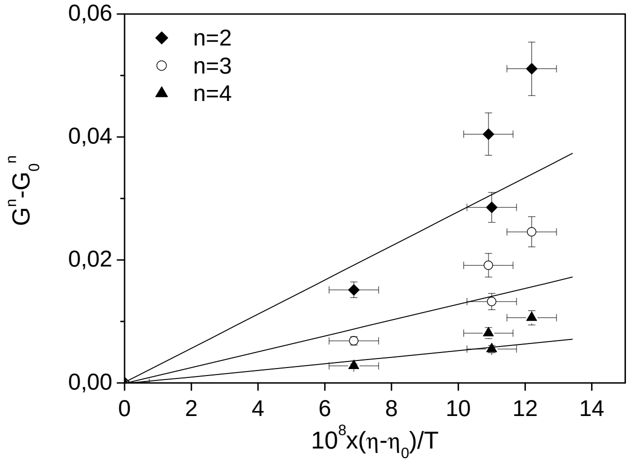

Figure 7.5.: Linear relation between grain growth and uniaxial viscosity during isotherms at T= 1350 °C for n between 2 and 4 (for several grain growth mechanisms)

7.3.2. Viscous Poisson ratio

For hot-forging experiments, the viscous Poisson ratio ν_v is expected between 0 and 0.5 (see Section 2.2).

The experimental results of this work on the viscous Poisson ratio ν_v are plotted in Figure 7.6 (the fits are given) together with the experimental results of Zuo's work [66] with Al_2O_3 samples. All results show a steady increase of ν_v in the range 0 to 0.5 as densification is occurring. Part of the discrepancies between the experimental results of this work and the literature results can be attributed to the experimental procedures: density, temperature, material, green-body homogeneity, etc... The onset of ν_v is found between 0 and 0.1 in this work and about 0.2 by Zuo et al. [66]. They significantly differ from one to the other experiment, but agree to state the onset value of ν_v different from 0.

In a porous cubic (CS) structure (see Figure 7.3 particles 1 to 4) under uniaxial forces, there is intensification of the stresses at the necks being not oriented along the force [66]. In this case, there is no macroscopic deformation in the radial direction, suggesting $\nu_v = 0$. However, particles are randomly distributed in real structures (see Figure 7.3 particles 5 to 9). Under uniaxial forces, a shearing at the necks may occur, leading to a radial deformation of the structure. The radial deformation remains small at low temperatures (i) as shearing is controlled by (non activated) diffusion mechanisms and (ii) as particles are closely packed. When the diffusion mechanisms are activated, neck growth occurs and a larger viscous response in the radial direction can be expected. The pre-sintering before the measurement starts in Zuo's experiments explains the onset of ν_v by 0.2 [67]. Finally, this reasoning leads also to state $\nu_v \neq 0$ at low temperatures. However, the experimental accuracy obtained in this work is not sufficient at low temperatures either to experimentally validate this hypothesis or to point out one finite value of ν_v.

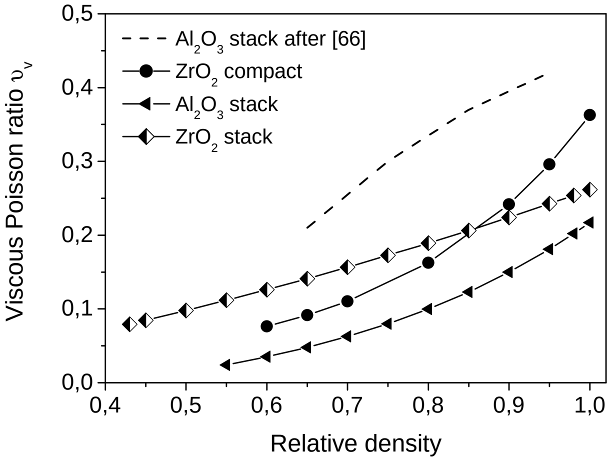

Figure 7.6.: Comparison of the viscous Poisson ratio measured in this work (the fits of the data points are given) for several samples (ZrO_2 compacts, ZrO_2 and Al_2O_3 stacks) and reported in literature for a Al_2O_3 compact [66] (approximate reproduction of the results from publications)

8. Conclusions and outlook

The present work aims at the establishment of an alternative to the complex material models for co-sintering and at the development of the associated experimental method.

A two part-material model is proposed in this work, it is built with:

1. the Master Sintering Diagram (MSD) for the prediction of sintering kinetics,
2. the cyclic unloading measurement method for the determination of the viscous moduli.

Figure 8.1 recalls the construction of the material model and the major results of the thesis.

8.1. Conclusions on the material model

From this work, the following conclusions can be drawn:

■ **The sintering kinetics of homogeneous porous bodies are successfully predicted with the Master Sintering Diagram (MSD).**

- The experimental procedure allows the collection of sintering data with a good quality: in the case of homogeneous green-bodies, the deviation between axial and radial strains is at most 2% (see Chapter 4).
- The changes in the temperature profile and in external stresses are correctly predicted so that, the sintering kinetics are predicted with a maximum deviation of 10% (see Chapter 5) compared to the experimental results.
- The MSD successfully takes into account the loading memory in the predictions of the sintering kinetics (see Chapter 4 for the evidence of the loading memory and Chapter 5 for the predictions of sintering kinetics with consideration of the loading history).

- **The interpretation of the MSD delivers information on sintering of the studied material**
    - The construction of the MSD permits the determination of the apparent activation energy for sintering and for creep. In the case of the ZrO_2 powder compacts, sintering and creep are controlled by the same diffusion mechanism (see Chapter 4).
    - Grain growth leads to the variation of the apparent activation energy. Since the grain growth of the ZrO_2 powder compacts is small, the effect remains small (see Chapter 4).
    - Heterogeneities in green-bodies affect the sintering kinetics curves and can lead to a misinterpretation of the MSD or can impede the interpretation of the MSD (see Chapter 4). It can be differently stated: an odd MSD and non explainable apparent activation energies can be the consequence of non homogeneous green-bodies.

- **The cyclic unloading method allows the determination of the viscous moduli**
    - The experimental results for the uniaxial viscosity and the viscous Poisson ratio are consistent with the expectations, at least at high temperatures (see Chapter 4 and Chapter 5): the viscous response of the material at temperatures below 1000 °C are not sufficiently significant to be able to state on the onset values of the viscous Poisson ratio (between 0 and 0.1).
    - Heterogeneities in samples bias the viscous moduli (see Chapter 5).
    - Grain growth leads to the increase of uniaxial viscosity (see Chapter 4).

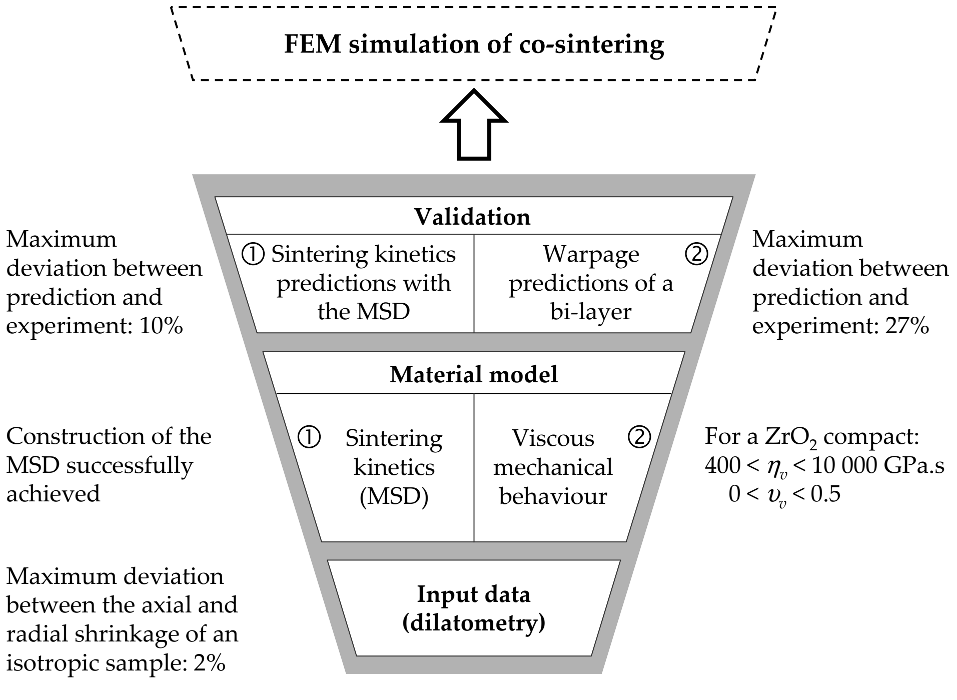
FEM simulation of co-sintering
Validation
① Sintering kinetics predictions with the MSD
Warpage predictions of a bi-layer ②
Maximum deviation between prediction and experiment: 10%
Maximum deviation between prediction and experiment: 27%
Material model
① Sintering kinetics (MSD)
Viscous mechanical behaviour ②
Construction of the MSD successfully achieved
For a ZrO_2 compact:
$400 < \eta_v < 10\,000$ GPa.s
$0 < \upsilon_v < 0.5$
Input data (dilatometry)
Maximum deviation between the axial and radial shrinkage of an isotropic sample: 2%

Figure 8.1.: Scheme describing the structure of the present work and the main results.

- The influence of the thermal treatment on the bulk and shear viscosities can be addressed with an Arrhenius plot like the MSD (see Chapter 4).

- The warpage of a bi-layer can be modelled using the free sintering mismatch between the materials and the viscous moduli: the prediction of the curvature rate is qualitatively in good agreement with the experimental result, however the maximum deviation between prediction and measurement is 27% (see Chapter 5).

8.2. Parameters affecting co-sintering

In the present work, the study of the bi-layer glass-ceramic and Al_2O_3 illustrates that this material model is not the only way to understand co-sintering cases (see Chapter 4). Several parameters for the reduction of the deformation during co-sintering are listed:

1. The *nature of the materials* plays a large role in the sintering kinetics. Additions of a second phase in one of the materials (like sintering aids or sintering retardants) leading to a crystal phase transformation, formation of a liquid phase, glass crystallization modify the sintering kinetics.

2. The *green-body homogeneity* and the *initial density* can be used to modify the sintering kinetics. Modifications of this parameters can be assessed for instance by the processing and by the powder size distribution.

3. the *temperature profile* is simultaneously applied to all materials of the composites. Pre-sintering and slow heating rates retard and reduce the sintering activity by extensive coarsening and neck growth (see Chapter 4). Thus they have impacts on grain growth and final density. In contrast, fast heating rate tends to reduce the viscosity (in comparison to slow heating rates).

4. The *geometrical solutions* by modification of the dimensions and geometries or the use of *sacrificial parts* can eventually reduce the macroscopic deformations.

8.3. Outlook

The present study constitutes a solid base towards the simulation of co-sintering with a simple material model. Further works and new axis of research are pointed out:

- Reduction of the number of experiments required for the construction of the MSD.
- Application of the material model to other materials like liquid-phase materials or metals.
- Improvement of the characterization method for the viscous behaviour at low temperatures. This is probably possible only with an improvement of the measurement resolution.
- Study of the influence of the microstructure anisotropy on the viscous moduli.
- Determination of the viscous behaviour of sintering materials under tension.
- Improvement of characterization methods for tapes using a measurement with a better reliability and a better resolution.
- Study of the pore orientation during a short loaded period either in tension or in compression and after successive tension and compression sequences.
- Correction of the thermal memory for more accurate predictions of the sintering kinetics.
- Implementation of the material model in the FEM and simulation of co-sintering.
- Development of an efficient tool for the determination of grain growth as function of the thermal treatment.

Appendix

A. True strain

A.1. Strains and strain rates

The software of the optical dilatometer TOMMI gives out the instant dimension relative to the initial dimension $L(t)/L_0$ with $L(t)$ is the instant length and L_0 is the size at the beginning of the experiment, i.e. at room temperature. This output is not exactly the strain from the mechanical point of view. Therefore a slight data treatment is required in order to deal with strain values.

Two expressions of strain exist: the true strain and engineering strain. These are often mixed-up, therefore a short explanation is required to distinguish both.

A.2. Linear true and engineering strains

The *engineering strain* ε_e is defined by:

$$\varepsilon_e = \frac{\Delta L}{L_0} = \frac{L(t)}{L_0} - 1 \tag{A.1}$$

When a volume of a length L_0 is successively extended of length δl_1 and δl_2, the total strain becomes:

$$\varepsilon_e = \varepsilon_1 + \varepsilon_2 = \frac{(L_0 + \delta l_1) - L_0}{L_0} + \frac{(L_0 + \delta l_2) - (L_0 + \delta l_1)}{(L_0 + \delta l_1)} \tag{A.2}$$

Only if the deformations are very small ($\delta l \ll L_0$) then it can be said that $\delta l + L_0 \approx L_0$ and the equation A.2 can be simplified with:

$$\varepsilon_e = \varepsilon_1 + \varepsilon_2 = \frac{\delta l_1 + \delta l_2}{L_0} \tag{A.3}$$

The *true strain* ε_t is defined by the infinite sum of each elemental change, so the total strain after successive extensions can be written:

$$\varepsilon_t = \frac{\delta L_1}{L_0} + \frac{\delta L_2}{L_1} + \cdots + \frac{\delta L_f}{L_{f-1}} \tag{A.4}$$

Since δl are very small next to L_0, the summation of all small strains δl can also be written

$$\begin{aligned}\varepsilon_t &= \int_{L_0}^{L_f} \frac{\delta l}{l} = ln\left(\frac{L_f}{L_0}\right)\\ &= ln\left(1 + \frac{\Delta L}{L_0}\right) = ln\left(1 + \varepsilon_e\right) \qquad \text{(A.5)}\end{aligned}$$

Plots of the expressions of the true and engineering strains can be seen in the figure A.1. The linear relation between engineering and true strains remains valid only for small strains <6%, which means that below this value one or the other expression give a comparable result. However for larger deformations the condition $\delta l \ll L_0$ is not valid anymore and the expression of the engineering strain become less precise. In science of sintering, measured strains during shrinkage is very likely over 6% thus true strains are recommended.

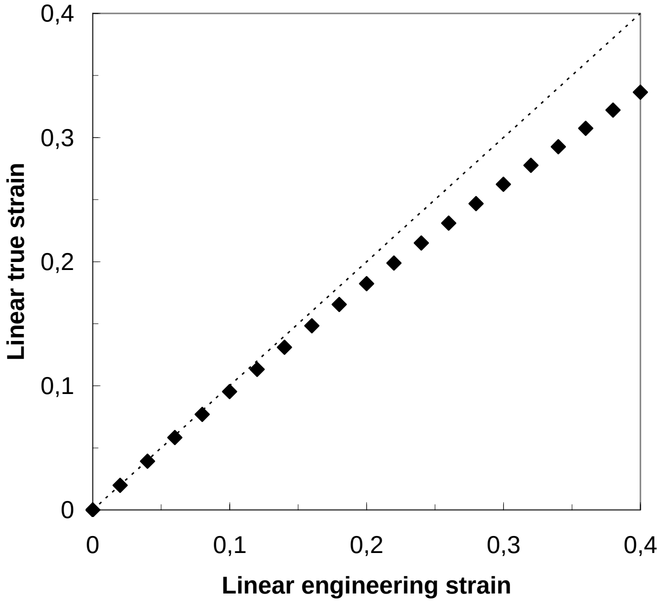

Figure A.1.: Evolution of the linear engineering and true strains from the equations A.1 and A.5 respectively

A.3. Volumetric strains and densities

The volumetric strain is mostly used to calculate the density from dilatometric data. Let us consider a volume V_0 which lengths are a_0, b_0 and c_0, so the initial volume is $\{V_0 = a_0 \times b_0 \times c_0\}$. The volume V_0 exhibits successive deformations δV and the volumetric strain is named ε^V. The *volumetric engineering strain* ε_e^V considers the length change in each direction, therefore it can be written:

$$\begin{aligned}
\varepsilon_e^V &= \frac{V(t)}{V_0} - 1 \\
&= \frac{(a_0 + \Delta a)(b_0 + \Delta b)(c_0 + \Delta c)}{a_0 b_0 c_0} - 1 \\
&= (1 + \varepsilon_a)(1 + \varepsilon_b)(1 + \varepsilon_c) - 1 \qquad \text{(A.6)}
\end{aligned}$$

if the volume change is isotropic, then the volumetric engineering strain is expressed with:

$$\varepsilon_e^V = (1 + \varepsilon_e)^3 - 1 = \left(\frac{L(t)}{L_0}\right)^3 - 1 \qquad \text{(A.7)}$$

By analogy to the linear true strain, the volumetric true strain is determined by summation of the infinitesimal changes of volume:

$$\varepsilon_T^V = \int_{V_0}^{V(t)} \frac{\delta V}{V_0} \qquad \text{(A.8)}$$

Furthermore the partial derivative of an infinitesimal change of volume is expressed by:

$$\begin{aligned}
\delta V &= \frac{\partial V}{\partial a} \cdot \delta a + \frac{\partial V}{\partial b} \cdot \delta b + \frac{\partial V}{\partial c} \cdot \delta c \\
&= bc \cdot \delta a + ac \cdot \delta b + ab \cdot \delta c \qquad \text{(A.9)}
\end{aligned}$$

this infinitesimal volume change related to the initial volume V_0 gives:

$$\frac{\delta V}{V_0} = \frac{\delta a}{a_0} + \frac{\delta b}{b_0} + \frac{\delta c}{c_0} = \sum_{i=a}^{c} \frac{\delta l_i}{l_{0,i}} \qquad \text{(A.10)}$$

By analogy with the expression of the linear true strain, the volumetric true strain is determined by the summation of infinitesimal changes of volume. Combining equations A.8 and A.10, we obtain:

$$\varepsilon_T^V = \int_{V_0}^{V(t)} \frac{\delta V}{V_0} = \sum_{i=a}^{c} \int_{l_0}^{l(t)} \frac{\delta l_i}{l_{0,i}} = \sum_{i=a}^{c} \varepsilon_{T,i} = \sum_{i=a}^{c} ln\left(\frac{L_i(t)}{L_{0,i}}\right) \qquad \text{(A.11)}$$

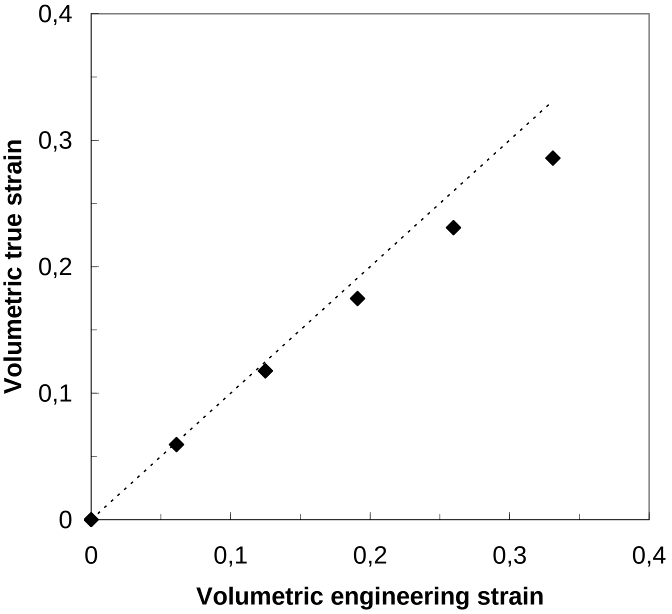

Figure A.2.: Evolution of the volumetric engineering and true strains from the equations A.6 and A.12 respectively

If the volume change is isotropic, then the volumetric true strain is expressed with:

$$\varepsilon_T^V = 3\varepsilon_T = ln\left(\frac{L(t)}{L_0}\right)^3 \tag{A.12}$$

Again two expressions for the volumetric strain are obtained: for isotropic deformations the volumetric engineering strain ε_e^V depends of the third power of the linear engineering strain and the volumetric true strain is obtained by the multiplication of the linear true strains in the three dimensions. Plotting both relations, the volumetric strains differ in their prediction (see figure A.2). For small linear strains <6% one or the other relation can be used without significant difference. For sintering application the volumetric true strains are advised to be used, since linear shrinkages over 6% can be expected.

The density of a sintering body is directly calculated from the relation of mass conservation:

$$\frac{\rho(t)}{\rho_0} = \frac{V_0}{V_t} \tag{A.13}$$

Considering the expression of the volumetric engineering strain (relations A.6 and A.7,

$$\frac{V_t}{V_0} = \varepsilon_e^V + 1 = \left(\frac{L(t)}{L_0}\right)^3 \tag{A.14}$$

On the other hand, the consideration of the volumetric true strain from the relations A.8 and A.12

gives:

$$\varepsilon_T^V = ln\frac{V(t)}{V_0} = ln\left(\frac{L(t)}{L_0}\right)^3 \tag{A.15}$$

equivalent to

$$\frac{V(t)}{V_0} = \left(\frac{L(t)}{L_0}\right)^3 \tag{A.16}$$

Keeping in mind the output of the dilatometer software ($L(t)/L_0$) the previous discussion on volumetric strains becomes quite relative. The instant densities during sintering are assessed directly from the output of the software without further consideration of the instant volumetric strain using the relation:

$$\frac{\rho(t)}{\rho_0} = \left(\frac{L(t)}{L_0}\right)^{-3} \tag{A.17}$$

B. Phase diagram ZrO_2 - Y_2O_3

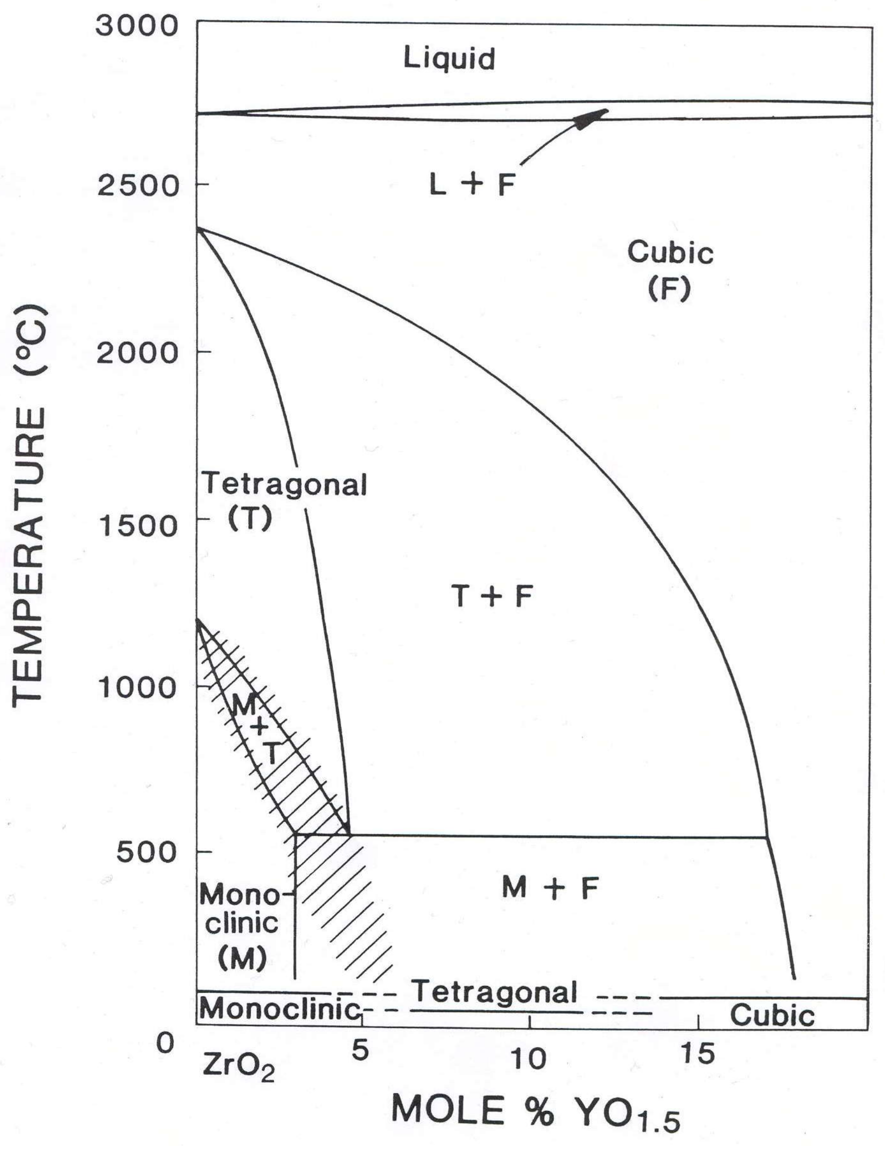

Figure B.1.: Zirconia-rich end of the ZrO_2-Y_2O_3 phase equilibrium diagram after [68]. Non equilibrium homogeneous phases are indicated at the lower margin. Hatched region indicates nonequilibrium monoclinic-tetragonal transition.

Bibliography

[1] C. H. Hsueh, A. G. Evans, R. M. Cannon, and R. J. Brook. Viscoelastic stresses and sintering damage in heterogeneous powder compacts. *Acta Metallurgica*, 34(5):927–936, 1986.

[2] D. J. Green, Olivier Guillon, and J. Rodel. Constrained sintering: A delicate balance of scales. *Journal of the European Ceramic Society*, 28(7):1451–1466, 2008.

[3] D. J. Green, P. Z. Cai, and Gary L. Messing. Residual stresses in alumina-zirconia laminates. *Journal of the European Ceramic Society*, 19:2511–2517, 1999.

[4] Johannes Kanters, Ulrich Eisele, and Jurgen Rodel. Cosintering simulation and experimentation: Case study of nanocrystalline zirconia. *Journal of the American Ceramic Society*, 84(12):2757–2763, 2001.

[5] N.J. Shaw. Densification and coarsening during solid state sintering of ceramics: a review of the models - i. densification. *Powder Metallurgy International*, 21(3):16–21, 1989.

[6] N.J. Shaw. Densification and coarsening during solid state sintering of ceramics: a review of the models - ii. grain growth. *Powder Metallurgy International*, 21(5):31–33, 1989.

[7] N.J. Shaw. Densification and coarsening during solid state sintering of ceramics: a review of the models - iii. coarsening. *Powder Metallurgy International*, 21(6):25–29, 1989.

[8] R. M. German. Sintering densification for powder mixtures of varying distribution widths. *Acta Metallurgica et Materialia*, 40(9):2085–2089, 1992.

[9] H.C. Yang and K.T. Kim. Creep densification behavior of micro and nano metal powder: Grain size-dependent model. *Acta Materialia*, 54(14):3779–3790, 2006.

[10] E. A. Barringer and H. Kent Bowen. Effect of particle packing on the sintered microstructure. *Journal of Applied Physics*, A45:271–275, 1988.

[11] Jingmin Zheng and James S. Reed. Effects of particle packing characteristics on solid-state sintering. *Journal of the American Ceramic Society*, 72(5):810–817, 1989.

[12] P. Markondeya Raj, A. Odulena, and W. R. Cannon. Anisotropic shrinkage during sintering of particle-oriented systems–numerical simulation and experimental studies. *Acta Materialia*, 50(10):2559–2570, 2002.

[13] I. O. Ozer, E. Suvaci, B. Karademir, J. M. Missiaen, C. P. Carry, and D. Bouvard. Anisotropic sintering shrinkage in alumina ceramics containing oriented platelets. *Journal of the American Ceramic Society*, 89(6):1972–1976, 2006.

[14] P. Markondeya Raj and W. Roger Cannon. Anisotropic shrinkage in tape-cast alumina: Role of processing parameters and particle shape. *Journal of the American Ceramic Society*, 82(10):2619–2625, 1999.

[15] M. F. Ashby and R. A. Verrall. Diffusion-accommodated flow and superplasticity. *Acta Metallurgica*, 21(2):149–163, 1973.

[16] C. Herring. Diffusional viscosity of a polycrystalline solid. *Journal of Applied Physics*, 21(5):437–445, 1950.

[17] R. L. Coble. A model for boundary diffusion controlled creep in polycrystalline materials. *Journal of Applied Physics*, 34(6):1979–1682, 1963.

[18] L. C. De Jonghe and M. N. Rahaman. Loading dilatometer. *Review of Scientific Instruments*, 55(12):2007–2010, 1984.

[19] George W. Scherer. Viscous sintering under a uniaxial load. *Journal of the American Ceramic Society*, 69(9):C–206–C–207, 1986.

[20] Ruzhong Zuo, Emil Aulbach, Rajendra K. Bordia, and Jurgen Rodel. Critical evaluation of hot forging experiments: Case study in alumina. *Journal of the American Ceramic Society*, 86(7):1099–1105, 2003.

[21] M. N. Rahaman, L. C. Jonghe, and C. H. Hsueh. Creep during sintering of porous compacts. *Journal of the American Ceramic Society*, 69(1):58–60, 1986.

[22] J. Svoboda, H. Riedel, and H. Zipse. Equilibrium pore surfaces, sintering stresses and constitutive equations for the intermediate and late stages of sintering–i. computation of equilibrium surfaces. *Acta Metallurgica et Materialia*, 42(2):435–443, 1994.

[23] H. Riedel, H. Zipse, and J. Svoboda. Equilibrium pore surfaces, sintering stresses and constitutive equations for the intermediate and late stages of sintering–ii. diffusional densification and creep. *Acta Metallurgica et Materialia*, 42(2):445–452, 1994.

[24] H. Riedel, V. Kozak, and J. Svoboda. Densification and creep in the final stage of sintering. *Acta Metallurgica et Materialia*, 42(9):3093–3103, 1994.

[25] J. Kanters, U. Eisele, and J. Rodel. Effect of initial grain size on sintering trajectories. *Acta Materialia*, 48(6):1239–1246, 2000.

[26] H. Palmour III and M.L. Huckabee. Studies in densification dynamics. In New York Plenum Press, editor, *Materials Science Research*, volume 6, pages 275–282. 1973.

[27] Hunghai Su and D. Lynn Johnson. Master sintering curve: A practical approach to sintering. *Journal of the American Ceramic Society*, 79(12):3211–3217, 1996.

[28] K. An and M.K. Han. Microstructural evolution based on the pressure-assisted master sintering surface. *Materials Science and Engineering A*, 391:66–70, 2005.

[29] F. Raether and P. Schulze-Horn. Investigation of sintering mechanisms of alumina using kinetic field and master sintering diagrams. *Journal of the European Ceramic Society*, 29(11):2225–2234, 2009.

[30] R. K. Bordia and G. W. Scherer. On constrained sintering–i. constitutive model for a sintering body. *Acta Metallurgica*, 36(9):2393–2397, 1988.

[31] R. K. Bordia, R. Zuo, Olivier Guillon, Samuel M. Salamone, and J. Rodel. Anisotropic constitutive laws for sintering bodies. *Acta Materialia (formerly called Acta Metallurgica et Materialia)*, 54(1):111–118, 2006.

[32] R. A. Gregg and F. N. Rhines. Surface tension and the sintering force in copper. *Metallurgical Transactions*, 4:1365–1374, 1973.

[33] V. M. Sglavo, P. Z. Cai, and D. J. Green. Damage in al2o3 sintering compacts under very low tensile stress. *Journal of Materials Science Letters*, 18(11):895–900, 1999.

[34] Peter Z. Cai, Gary L. Messing, and David J. Green. Determination of the mechanical response of sintering compacts by cyclic loading dilatometry. *Journal of the American Ceramic Society*, 80(2):445–452, 1997.

[35] O. Gillia, C. Josserond, and D. Bouvard. Viscosity of wc-co compacts during sintering. *Acta Materialia*, 49(8):1413–1420, 2001.

[36] Ruzhong Zuo, Emil Aulbach, and J. Rodel. Experimental determination of sintering stresses and sintering viscosities. *Acta Materialia (formerly called Acta Metallurgica et Materialia)*, 51(15):4563–4574, 2003.

[37] M. N. Rahaman. *Ceramic Processing and Sintering*. Marcel Dekker Inc., 1995.

[38] R. M. German. *Sintering Theory and Practice*. Wiley-interscience Publication, 1996.

[39] R. L. Coble. Intermediate-stage sintering: Modification and correction of a lattice-diffusion model. *Journal of Applied Physics*, 32:2327, 1965.

[40] D. Lynn Johnson and Ivan B. Cutler. Diffusion sintering: I, initial stage sintering models and their application to shrinkage of powder compacts. *Journal of the American Ceramic Society*, 46(11):541–545, 1963.

[41] W. D. Kingery and M. Berg. Study of the initial stages of sintering solids by viscous-flow, evaporation-condensation, and self-diffusion. *Journal of Applied Physics*, 26(10):1205–1212, 1955.

[42] W. Beere. The second stage sintering kinetics of powder compacts. *Acta Metallurgica*, 23(1):139–145, 1975.

[43] R. L. Coble. Sintering crystalline solids. i. intermediate and final state diffusion models. *Journal of Applied Physics*, 32(5):787–792, 1961.

[44] L. E. Malvern. *Introduction to the Mechanics of a continuous medium.* Prentice-Hall, Inc, 1969.

[45] R. K. Bordia and G. W. Scherer. On constrained sintering–ii. comparison of constitutive models. *Acta Metallurgica*, 36(9):2399–2409, 1988.

[46] Ruzhong Zuo and Jurgen Rodel. Temperature dependence of constitutive behaviour for solid-state sintering of alumina. *Acta Materialia*, 52(10):3059–3067, 2004.

[47] F. Raether. Currebt state of in situ measuring methods for the control of firing processes. *Journal of the American Ceramic Society*, 92(1):S146–S152, 2009.

[48] Rishi Raj. Analysis of the sintering pressure. *Journal of the American Ceramic Society*, 70(9):C–210–C–211, 1987.

[49] Peter Z. Cai, David J. Green, and Gary L. Messing. Constrained densification of alumina/zirconia hybrid laminates, ii: Viscoelastic stress computation. *Journal of the American Ceramic Society*, 80(8):1940–1948, 1997.

[50] Sang-Ho Lee, Gary L. Messing, and David J. Green. Bending creep test to measure the viscosity of porous materials during sintering. *Journal of the American Ceramic Society*, 86(6):877–882, 2003.

[51] Erwin E. Underwood. *Quantitative Stereology.* Addison-Wesley Publishing Company.

[52] Daniel Meyer. *Herstellung und Characterisierung von codotiertem und* $SrAl_{12}O_{19}$*-verstärktem Zirkonumdioxid.* Technischen Universität Darmstadt Germany, 2008.

[53] Ivan B. Cutler. Sintering of glass powders during constant rates of heating. *Journal of the American Ceramic Society*, 52(1):14–17, 1969.

[54] Guillaume Bernard-Granger and Christian Guizard. Apparent activation energy for the densification of a commercially available granulated zirconia powder. *Journal of the American Ceramic Society*, 90(4):1246–1250, 2007.

[55] Chun-Hway Hsueh, Anthony G. Evans, and Robert M. McMeeking. Influence of multiple heterogeneities on sintering rates. *Journal of the American Ceramic Society*, 69(4):C–64–C–66, 1986.

[56] J. Kanters, U. Eisele, H. Bder, and J. Rodel. Continuum mechanical description of sintering nanocrystalline zirconia. *Advanced Engineering Materials*, 3(3):158–162, 2001.

[57] Sathya Swaroop, Martin Kilo, Christos Argirusis, Gnter Borchardt, and A. H. Chokshi. Lattice and grain boundary diffusion of cations in 3ytz analyzed using sims. *Acta Materialia*, 53(19):4975–4985, 2005.

[58] Y. Okamoto, J. Leuji, Y. Yamada, K. Hayashi, and T. Nischikawa. Creep deformation of yttria-stabilized tetragonal zirconia (y-tzp). *Advances in Ceramics*, 24:565–571, 1988.

[59] Koji Matsui, Akira Matsumoto, Masato Uehara, Naoya Enomoto, and Junichi Hojo. Sintering kinetics at isothermal shrinkage: Effect of specific surface area on the initial sintering stage of fine zirconia powder. *Journal of the American Ceramic Society*, 90(1):44–49, 2007.

[60] Jenqdaw Wang and Rishi Raj. Activation energy for the sintering of two-phase alumina/zirconia ceramics. *Journal of the American Ceramic Society*, 74(8):1959–1963, 1991.

[61] May-Ying Chu, Mohamed N. Rahaman, Lutgard C. Jonghe, and Richard J. Brook. Effect of heating rate on sintering and coarsening. *Journal of the American Ceramic Society*, 74(6):1217–1225, 1991.

[62] Koji Matsui, Hideharu Horikoshi, Nobukatsu Ohmichi, Michiharu Ohgai, Hidehiro Yoshida, and Yuichi Ikuhara. Cubic-formation and grain-growth mechanisms in tetragonal zirconia polycrystal. *Journal of the American Ceramic Society*, 86(8):1401–1408, 2003.

[63] J. R. Seidensticker and Merrilea J. Mayo. Dynamic and static grain growth during the superplastic deformation of 3y-tzp. *Scripta Materialia*, 38(7):1091–1100, 1998.

[64] Dustin Frame and R. K. Bordia. Stress assisted sintering: evolution of anisotropic microstructures. In *Sintering '05*, volume 4e5, pages 272–275, Grenoble, France, 2005.

[65] Olivier Guillon, L. Weiler, E. Aulbach, and J. Rodel. Anistropic sintering of alumina thin films. In *Sintering '05*, volume 3b2, pages 204–207, Grenoble, France, 2005.

[66] Ruzhong Zuo, Emil Aulbach, and Jurgen Rodel. Viscous poisson's coefficient determined by discontinuous hot forging. *Journal of Materials Research*, 18(9):2170–2176, 2003.

[67] Olivier Guillon. personal communication. *Universität Darmstadt (Germany)*, 2009.

[68] D. J. Green, R. H. Hannink, and M. V. Swain. *Transformation toughening of ceramics*. CRC Press, Boca Raton, 1989.

List of Figures

1.1. Illustration showing the possible defects in a bi-layer due to the stresses during co-sintering 2
1.2. Scheme describing the structure and the red-line of the present work 6

2.1. Schematic construction of the MSD 11
2.2. Increment method of the MSD with one time increment *dt* 12
2.3. Graphical representation of prediction procedure with the MSD 12
2.4. Graphical representation of the cyclic unloading method 14

3.1. SEM image of the ZrO_2 green-body 16
3.2. Sketch of the optical dilatometer TOMMI 18
3.3. Exemplary images taken by TOMMI 19
3.4. Reproducibility of the strain measurements in temperature with TOMMI 19
3.5. Setup for the free sintering measurements of tapes in TOMMI 20
3.6. V-shape sample holders for the cyclic unloading method 21
3.7. Setup for the cyclic unloading in Tommi 22
3.8. Setup for the bending tape measurement in TOMMI 22
3.9. In-situ image of a warped bi-layer on a plate 25
3.10. Sketch of a warped bi-layer 27
3.11. In-situ image of a bent glass-ceramic tape on the bending setup 28
3.12. Sketch showing the determination of the orientation of an elliptic pore 30

4.1. Free sintering strains of ZrO_2 pressed samples 32
4.2. Sintering strain under uniaxial load of ZrO_2 pressed samples 34
4.3. Creep behaviour for ZrO_2 with the relation stress-strain rate 35
4.4. Influence of the load on densification of ZrO_2 compacts 35
4.5. Comparison of the sintering strain rates during loaded and unloaded sequences of a cyclic loading measurement 36
4.6. Comparison of the free sintering strain rates and the strain rates of unloaded sequences 37
4.7. Evidence of loading memory of the material with loaded measurements 37
4.8. Cross-section of the MSD for 1 N measurements 39
4.9. Apparent activation energy for free sintering of 3Y-ZrO_2 39

4.10. Cross-sections of the MSD at defined loads (50 N, 100 N, 150 N and 200 N) . . . 40
4.11. Shift of the iso-strain lines represented in a 2D-projection of the MSD 41
4.12. Horizontal cross-section of the MSD 42
4.13. Uniaxial viscosity and Poisson ratio for ZrO_2 pressed compacts 43
4.14. Influence of the heating rate on the shear and bulk viscosities of ZrO_2 pressed compacts 44
4.15. Influence of the heating rate on the uniaxial viscosity of ZrO_2 compacts 45
4.16. Influence of the heating rate on the viscous Poisson ratio of ZrO_2 compacts . . . 45
4.17. Influence of the thermal profile on the shear and bulk viscosities for ZrO_2 pressed compacts 47
4.18. Evolution of the viscous moduli η_v and ν_v during a dwell at 1350 °C 47
4.19. SEM images of dense freely sintered ZrO_2 samples 48
4.20. Influence of the sintering profile on the average cord-length 49
4.21. Influence of the holding time in dense samples on the microstructure regarding the grains 50
4.22. Binary-converted images of a porous ZrO_2 sample 50
4.23. Pore orientation in a porous structure sintered under uniaxial load 51

5.1. Predicted free sintering strain of a thermal treatment with constant heating rate . 54
5.2. Predicted free sintering strain of a thermal treatment with a temperature dwell . . 55
5.3. Prediction of the sintering strains under uniaxial compression (run 1) 56
5.4. Prediction of the sintering strains under uniaxial compression (run 2) 57
5.5. Free sintering strains of Al_2O_3 and ZrO_2 stacks 59
5.6. SEM image of the microstructure of a sintered Al_2O_3 stack 59
5.7. Uniaxial viscosity of Al_2O_3 stacks 60
5.8. Uniaxial viscosity of ZrO_2 stacks 60
5.9. Viscous Poisson ratio of Al_2O_3 stacks 61
5.10. Viscous Poisson ratio of ZrO_2 stacks 61
5.11. Shear and bulk viscosities of Al_2O_3 stacks 62
5.12. Shear and bulk viscosities of Al_2O_3 stacks 63
5.13. Experimentally measured warpage and prediction of a bi-layer Al_2O_3/ZrO_2 . . . 65

6.1. Shrinkage strain and strain rate of the glass-ceramic tape 68
6.2. Kinetic-field for sintering of the glass-ceramic tape 69
6.3. Diffractogram of the glass-ceramic tape 70
6.4. Evolution of the phase distribution during sintering 70
6.5. Influence of the heating rate on the phase distribution in the glass-ceramic 71
6.6. Viscosity of glass-ceramic 72
6.7. Sintering mismatch between glass-ceramic and alumina 73

6.8. Curvature of a bi-layer glass-ceramic/alumina and comparison with the sintering rate mismatch 74
6.9. Influence of the heating rate on the curvature rate of a bi-layer GC/alumina . . . 75
6.10. Curvature of a bi-layer GC/alumina during cooling 76
6.11. Relative dimensions of the glass-ceramic and Al_2O_3 tapes during cooling 77

7.1. Representation of the shift of the iso-strain points in the MSD due to the contribution of the surface diffusion 80
7.2. Variation of the apparent activation energy according to the dependence of C . . . 81
7.3. Simplified random particle packing in a porous structure undergoing an external and uniaxial compressive load 83
7.4. Comparison of the uniaxial viscosities measured in this work and reported in literature 85
7.5. Linear relation between grain growth and uniaxial viscosity during isotherms . . 87
7.6. Comparison of the viscous Poisson ratios measured in this work and reported in literature 88

8.1. Scheme describing the structure of the present work and the main results. 90

A.1. Linear engineering versus true strain 96
A.2. Volumetric engineering versus true strain 98

B.1. Phase diagram ZrO_2-Y_2O_3 101

List of Tables

2.1. Equations to describe the shrinkage by diffusion controlled solid-state sintering . 8
2.2. Diffusion creep models 9

3.1. Characteristics of the tapes used for the bi-layers 16
3.2. Sintering programs for loading dilatometry 24
3.3. Experimental programs for the model verification 25

4.1. Deviations between the radial and axial strains measured during the free sintering runs of ZrO_2 32
4.2. Quantitative description of free sintering shrinkage curves of ZrO_2 32
4.3. Crystalline phase distribution after thermal treatment 33

5.1. Deviations between prediction of the sintering kinetics and measurement with variable load 57
5.2. Fit parameters for the viscous Poisson ratio for the Al_2O_3 and ZrO_2 stacks 63
5.3. Deviations between prediction and measurement for the warpage of a bilayer alumina/zirconia 64

6.1. Quantitative description of sintering shrinkage curves of the glass-ceramic tape . 68

7.1. Activation energy E_a found in literature for 3Y-TZP materials 79
7.2. Simplified experimental procedures for the determination of uniaxial viscosity . . 86

List of symbols and abbreviations

Roman symbols

C, C_1, C_2:	material parameters
C_0:	unit factor in K/s, C_0 is implicit in the MSD plots despite the mathematical rigour
D:	diffusion coefficient
D_0:	pre-exponentiel diffusion coefficient
d_p:	shortest radius of an elliptic pore
D_p:	longest radius of an elliptic pore
E:	viscous moduli ratio of the materials of a bi-layer
E_a:	apparent activation energy (kJ/mol)
g:	gravity
G:	grain size
G_v:	shear viscosity
h:	thickness ratio of the layers in a bi-layer
K_v:	bulk viscosity
l:	cord-length of the linear intercept method
L:	macroscopic length of an object
m:	grain growth expenent function of the grain growth mechanism
n:	grain size exponent function of the sintering diffusion mechanism
Q_{gg}:	activation energy for grain growth
R:	gas constant
T	temperature
T_g:	temperature of glass transition

List of symbols and abbreviations

Greek symbols

α: coefficient of thermal expansion
ε: macroscopic strain or shrinkage strain (during sintering $\dot{\varepsilon} < 0$)
η_v: uniaxial viscosity
κ: curvature
ρ: density
σ: externally applied stress
ν_v: viscous Poisson ratio
χ: shape anisotropy factor of a grain

Derivated symbols

symbol + $(\dot{\ })$: time derivative or rate
symbol + $(\bar{\ })$: average value
symbol + $(_z)$: subscribe for z-direction (axial direction)
symbol + $(_r)$: subscribe for r-direction (radial direction)

Abbreviations

HR: heating rate
MSC: Master Sintering Curve
MSD: Master Sintering Diagram
KF: Kinetic-field
FEM: Finite Element Method
GC: glass-ceramic
SEM: Scanning electron microscope
SE: Secondary electron (refers to the SEM)
CTE: coefficient of thermal expansion

Curriculum Vitae

Name:	Marc Bruno Eric DELPORTE
Birth:	08.03.1980 in Saumur, France
Contact:	mbe.delporte@gmail.com

Studies

2006 - 2009:	Ph.D., Fraunhofer Institut for Silicat Research, Würzburg (DE) and Department of material research by Robert Bosch GmbH, Stuttgart (DE)
2002 - 2004:	Engineer Degree in Science of Ceramics, ENSCI, Limoges (FR)
2000 - 2002:	”Ingénieur-maître” diploma in Material Science, IUP, Poitiers (FR)
1998 - 2000:	Technician degree, IUT in Material Science, Blois (FR)

Professional experience, diploma work and traineeships

since 11/2009:	Engineer, Kläger Spritzguss GmbH & Co.KG, Dornstetten (DE)
10/2004 - 04/2006:	Engineer, EMPA, Dübendorf (CH)
03/2004 - 09/2004:	Diploma work, EMPA, Dübendorf (CH) Activation routes of alumina foams for producing MMCs by pressureless infiltration. *Ceramics International*, 33(7):1179-1185, 2007
2003 - 5 months:	Traineeship, Swedish Ceramic Institute, Gothenburg (SW)
2002 - 6 months:	Traineeship, French Atomic Energy Commission (CEA), Tours (FR)
2000 - 3 months:	Traineeship, Multitude Technologie, Laval (FR)